NASA/TP-20220002309

NASA Orbital Debris Engineering Model (ORDEM) 3.1
Model Verification and Validation

Orbital Debris Program Office

Timothy Kennedy
Mark Matney
Heather Cowardin
NASA Johnson Space Center
Houston, Texas

Alyssa Manis
HX5 – Jacobs JETS Contract

Andrew Vavrin
GeoControl Systems – Jacobs JETS Contract

John Seago
ERC – Jacobs JETS Contract

Drake Gates
Jacobs – Jacobs JETS Contract

Phillip Anz-Meador
Jacobs – Jacobs JETS Contract

Yu-lin Xu
University of Texas at El Paso – Jacobs JETS Contract

February 2022

NASA STI Program Report Series

The NASA STI Program collects, organizes, provides for archiving, and disseminates NASA's STI. The NASA STI program provides access to the NTRS Registered and its public interface, the NASA Technical Reports Server, thus providing one of the largest collections of aeronautical and space science STI in the world. Results are published in both non-NASA channels and by NASA in the NASA STI Report Series, which includes the following report types:

- TECHNICAL PUBLICATION. Reports of completed research or a major significant phase of research that present the results of NASA Programs and include extensive data or theoretical analysis. Includes compilations of significant scientific and technical data and information deemed to be of continuing reference value. NASA counterpart of peer-reviewed formal professional papers but has less stringent limitations on manuscript length and extent of graphic presentations.

- TECHNICAL MEMORANDUM. Scientific and technical findings that are preliminary or of specialized interest, e.g., quick release reports, working papers, and bibliographies that contain minimal annotation. Does not contain extensive analysis.

- CONTRACTOR REPORT. Scientific and technical findings by NASA-sponsored contractors and grantees.

- CONFERENCE PUBLICATION. Collected papers from scientific and technical conferences, symposia, seminars, or other meetings sponsored or co-sponsored by NASA.

- SPECIAL PUBLICATION. Scientific, technical, or historical information from NASA programs, projects, and missions, often concerned with subjects having substantial public interest.

- TECHNICAL TRANSLATION. English-language translations of foreign scientific and technical material pertinent to NASA's mission.

Specialized services also include organizing and publishing research results, distributing specialized research announcements and feeds, providing information desk and personal search support, and enabling data exchange services.

For more information about the NASA STI program, see the following:

- Access the NASA STI program home page at http://www.sti.nasa.gov

- Help desk contact information:

https://www.sti.nasa.gov/sti-contact-form/ and select the "General" help request type.

NASA/TP–20220002309

NASA Orbital Debris Engineering Model (ORDEM) 3.1
Model Verification and Validation

Orbital Debris Program Office

Timothy Kennedy
Mark Matney
Heather Cowardin
NASA Johnson Space Center
Houston, Texas

Alyssa Manis
HX5 – Jacobs JETS Contract

Andrew Vavrin
GeoControl Systems – Jacobs JETS Contract

John Seago
ERC – Jacobs JETS Contract

Drake Gates
Jacobs – Jacobs JETS Contract

Phillip Anz-Meador
Jacobs – Jacobs JETS Contract

Yu-lin Xu
University of Texas at El Paso – Jacobs JETS Contract

National Aeronautics and
Space Administration

Johnson Space Center
Houston, Texas 77058

February 2022

ACKNOWLEDGEMENTS

The authors would like to thank Debra Shoots for her technical editing of this document, and her expertise and guidance in the NASA STI release process. Additionally, the authors would like to thank the entire team in the NASA Orbital Debris Program Office that supported the radar, optical, and *in situ* data processing and analysis that were used in the model verification and validation process.

Available from:

NASA STI Program
Mail Stop 148
NASA Langley Research Center
Hampton, VA 23681-2199

National Technical Information Service
5285 Port Royal Road
Springfield, VA 22161

This report is also available in electronic form at http://www.sti.nasa.gov/ and http://ntrs.nasa.gov

REVISION AND HISTORY PAGE

REV.	DESCRIPTION	PUB. DATE
1.0	Initial Release	February 2022

This Page Intentionally Left Blank

TABLE OF CONTENTS

FIGURES

TABLES

This Page Intentionally Left Blank

1 INTRODUCTION

1.1 PURPOSE AND SCOPE

The NASA Orbital Debris Engineering Model (ORDEM) 3.1 Model Verification and Validation (V&V) document accompanies the delivery of the latest ORDEM 3.1 model (Vavrin & Manis, 2019) and provides a detailed description of the V&V activities used to verify that the model was built correctly and validate the model against independent, real world sources of data obtained from sampling the orbital debris environment. This ORDEM 3.1 Model V&V document, along with the related ORDEM 3.1 Model Process document – which covers details of the mathematical, statistical, and physical basis of the model – are intended to inform credibility assessments, risk analyses, uncertainty characterizations, and other applications derived from use of the model by the ORDEM 3.1 user community.

1.2 ORDEM 3.1 MODEL AND V&V DATA SOURCES

Data sources used for building and verifying the model were kept separate to the maximum extent possible from those used for model validation with this release of ORDEM 3.1. This follows recommendations from previous ORDEM release V&V activities, the NASA Engineering Safety Center (NESC), NASA-STD-7009A (Steele, 2016), as well as general best practices for statistical modeling. The latest release of ORDEM, version 3.1, incorporates recent radar data acquired from the Haystack Ultra-wideband Satellite Imaging Radar (HUSIR) and the Goldstone Solar System Radar for observations of debris populations in low Earth orbit (LEO), updated Michigan Orbital DEbris Survey Telescope (MODEST) data for observation of debris populations in the geosynchronous orbit (GEO) region, and the addition of recently available *in situ* data from exposed surfaces on the Hubble Space Telescope (HST) Wide Field Planetary Camera 2 (WFPC-2) radiator and multi-layer insulation (MLI). A diagram showing which sources were used for building and verifying the populations in ORDEM 3.1 and which were used for validation is shown in Figure 1-1 below. Table 1-1 shows the years of coverage and approximate size ranges for these sources. In addition to the previously mentioned sources, data from the Space Surveillance Network (SSN) and U.S. Space Transportation System (STS) were also used. Data for the sodium-potassium (NaK) population came from the HUSIR 2013 – 2015 radar measurements.

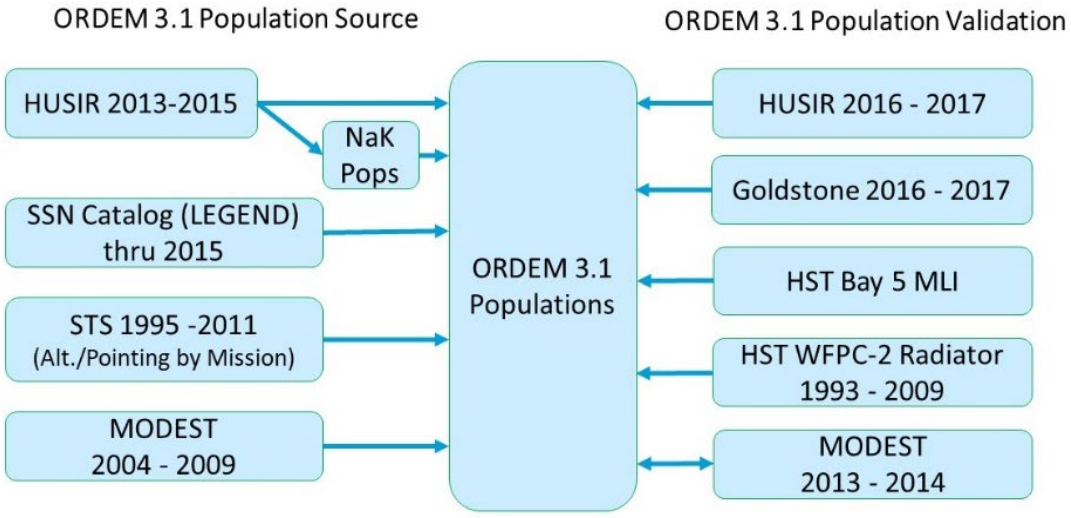

Figure 1-1. ORDEM 3.1 build and validation data sources.

Table 1-1. Data sources used for building and validating the ORDEM 3.1 populations, with applicable size limits and years of coverage.

Data Source	Size Limit (approximate)	Years Covered ORDEM 3.1
STS windows	10 – 300 μm	1995–2011
STS radiators	300 μm – 1 mm	1995–2011
HST Bay 5 MLI	10 – 300 μm	1990–2009
HST WFPC-2 Radiator	50 – 300 μm	1993–2009
Goldstone	3 – 8 mm	2016, 2017
HUSIR 75E	>5.5 mm	2007*, 2009*, 2013–2017
HUSIR 20S	>2 cm	2015
SSN Catalog	>10 cm (LEO) >1 m (GEO)	1957–2014 (LEO) 1957–2015 (GEO)
MODEST	>30 cm	2004–2006, 2007–2009, 2013–2014

* Datasets used for characterization of large breakups (Fengyun-1C, Iridium 33, and Cosmos 2251). Portions of dataset only around the time of the event were used.

1.3 FUTURE DATA SOURCES AND NESC RECOMMENDATIONS

The data in Figure 1-1 represents the best available concurrent with developing ORDEM 3.1. The recency of the data sources used in the building and validation of the model provide an updated state of the dynamic orbital debris environment. Future data sources that are anticipated to provide significant improvements in the building, verification, and validation of future releases of the model include: the Eugene Stansbery Meter Class Autonomous Telescope (ES-MCAT), future *in situ* debris sensors, and future upgrades to the SSN including the Space Fence and Space Surveillance Telescope (SST). Taken together, these future data sources, plus the integration of the new data sources from HST into ORDEM 3.1 validation, address recommendations from the NASA NESC directly applicable to the ORDEM model following the release of ORDEM 3.0.

2 VERIFICATION

2.1 MODEL VERIFICATION

Verification of the ORDEM 3.1 model is conducted by testing the as-built ORDEM model against data sources used to build the model to ensure that the implemented model matches the design to the extent possible given the constraints imposed by the different data sources used, and the concurrent applicability of the model to all orbital regimes sampled by the data sources. A detailed discussion of the model design and methods used to construct the ORDEM 3.1 model are covered in the ORDEM 3.1 Model Process Document, in progress, (Manis, *et al.*, 2022). Estimates of key parameters obtained from the different data sources used to build the model, and for verification purposes, will be discussed in this section – particularly those that relate to uncertainties associated with observed counts from radar, optical, or *in situ* data sources, as well as derivation of orbital debris size from the different data sources.

2.2 DEBRIS SIZE AND COUNT ESTIMATES

2.2.1 Size Estimates for Radar Data Sources

Size estimates from radar data sources are reported using the NASA Size Estimation Model (SEM), which relates the radar cross section (RCS) of debris objects from the measured Principal Polarization (PP) and Orthogonal Polarization (OP) channels, and a wavelength, to an empirically-derived characteristic length. The SEM originated from a study conducted by XonTech in the 1990's that utilized representative debris objects taken from two hypervelocity impact tests of simulated satellites at the Arnold Engineering Development Complex by the U.S. Department of Defense (Dalquist & Bohannon, 1991; Bohannon & Caampued, 1994). In addition to the representative debris objects from the hypervelocity impact tests, several debris-like objects were included in the sample to better represent the postulated debris environment at the time. The RCS values for the 39 debris objects were measured at an RCS radar range operated by the System Planning Corporation. RCS measurements of these objects were taken over 4 commonly used radar frequency bands (S band: 2.5647-3.9111 GHz; C band: 4.116-7.986 GHz; X band: 8.1544-12.7684 GHz; and Ku band: 12.924-17.538 GHz), with 8 frequency samples taken in the lowest frequency band, and 16 frequency samples taken in the remaining 3 frequency bands. These radar frequency bands correspond to the frequency bands in use by orbital debris radars. Measurements were taken from multiple different orientations of the debris objects to understand the distribution of possible RCS values that each piece of debris would present to a radar as the tumbling debris passes through the radar beam (Barton, 1998; Everett, Dalquist & Caampued, 1991).

The characteristic length, L_c, of an object is defined as the average of the three longest, orthogonal projected dimensions for an object measured along three orthogonal axes:

$$L_C = \frac{X + Y + Z}{3}. \qquad 2.2\text{-}1$$

The first axis coincides with the largest dimension, the second axis is the longest projection length in a plane orthogonal to the first axis, and the third axis is chosen to complete the orthogonal triad. This characteristic length is referred to in the remainder of this report as the size or diameter of the debris. Figure 2-1 shows an example of body dimensions of a complex-shaped object projected to a 2-dimensional surface. Note the projection measurement for Y is used for the calculation of L_c.

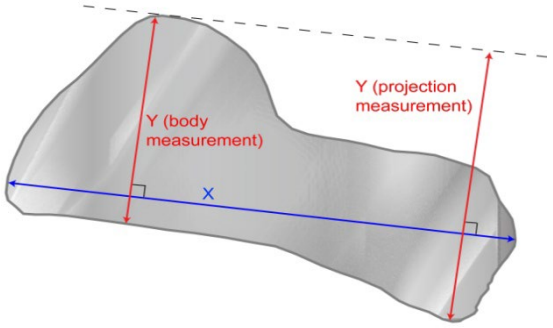

Figure 2-1: Illustration of body and projected measurement on complex shape (Hill, 2008).

Radar data from sensors operating with different wavelengths may be compared by scaling the size by the wavelength, λ, of the measurement frequency and scaling the RCS by the square of the wavelength. This results in a wavelength-normalized size, x = size/ λ, and a normalized RCS, z = RCS/ λ^2. Combining all of the measurements – different frequency and object orientations – onto a single plot results in the normalized RCS vs normalized size shown in Figure 2-2. Each of the 2072 data points on this plot uses a weighted average of the RCS taken for a single debris object, having a given wavelength-normalized size, over the hundreds of different orientations measured at a single frequency. The data were weighted to account for the non-uniform sampling of the object orientations as the data were collected (Dalquist & Bohannon, 1991; Bohannon & Caampued, 1994; Barton, 1998; Everett, Caampued & Chu, 1991; Everett, Dalquist & Caampued, 1991).

From the plot shown in Figure 2-2, a scaling curve – the solid black line – was developed from the data points. The solid blue line shows the theoretical normalized RCS for a sphere as a function of wavelength-normalized size. For debris sizes much smaller or larger than the radar wavelength, the scaling curve approaches the same result as the Rayleigh or optics regions, respectively, for the sphere. Between these two regimes is the Mie resonance region, where for the case of the sphere, there exists a one-to-many mapping between a given RCS value and the size of the sphere. In the case of the SEM, however, there is a one-to-one relationship between a given RCS and the size of the object, as shown in Figure 2-2 (solid black line).

For additional details on the piecewise function definition of the SEM or scaling curve from Figure 2-2, see (Xu & Stokely, 2005).

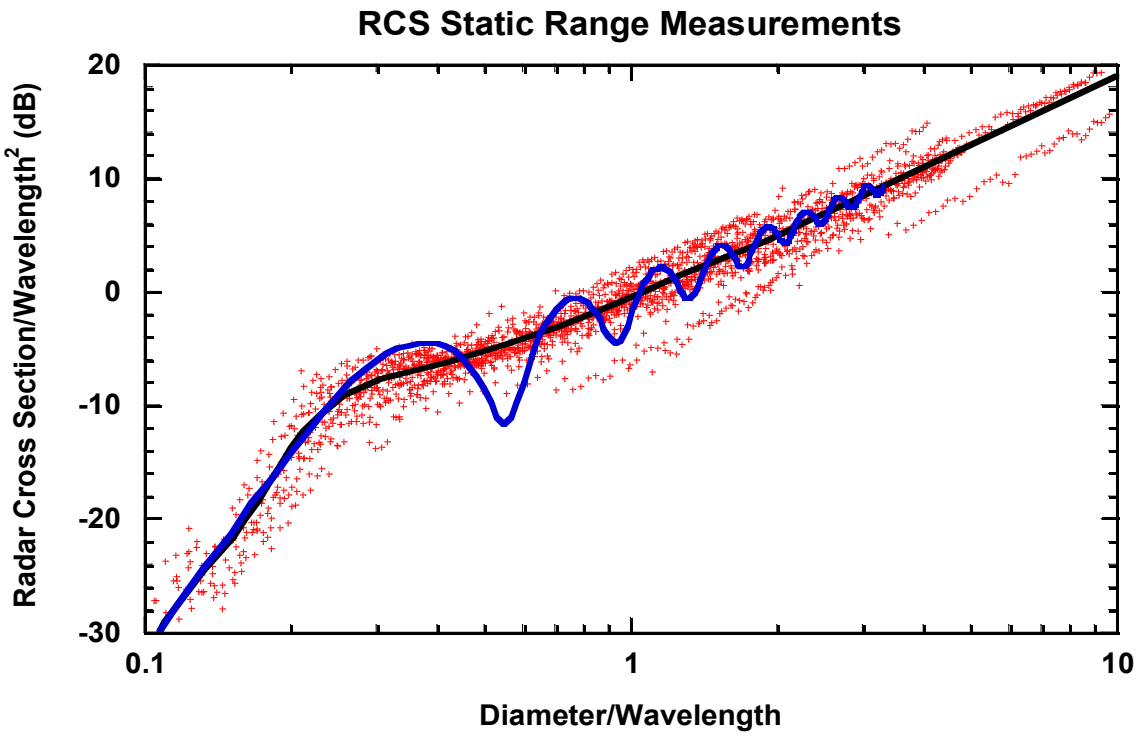

Figure 2-2. Results of RCS to physical size measurements for 39 representative debris objects over the frequency range 2.0–18 GHz (15–1.67 cm wavelength).

2.2.2 Size Estimates for In situ Data Sources

In situ data sets may be categorized as including dedicated *in situ* sensors, either active or passive, and impacts on surfaces returned from space and subsequently analyzed. Returned surface data were used in the development of ORDEM 3.0 and 3.1. In developing ORDEM 3.0, the STS fleet of orbiter vehicle's window and radiator impact data were used to build the small (less than approximately 3 mm) environment. Though impacts have been noted and characterized in STS reinforced carbon-carbon panels, the flexible reusable surface insulation blankets, and other structures, these were either too few or inadequately characterized to justify inclusion. The STS data set was reanalyzed for use in building ORDEM 3.1, and impact data sets derived from recent analyses of the HST WFPC-2 and MLI blankets, both returned by STS-125 in 2009, were incorporated into the ORDEM 3.1 validation efforts.

Size estimates from *in situ* data sources are reported using NASA-developed damage equations. Damage equations are interpretive, empirical equations which relate simple projectile characteristics (diameter d_p, mass density ρ) and impact circumstances (impact/relative velocity, *v*, and impact angle θ) to tangible impact characteristics (crater depth, crater, or penetration diameter, *etc.*). In general, these equations are of the form:

$$Y = c \cdot d_p^{\alpha} \cdot \rho^{\beta} \cdot v^{\gamma} \cdot (\cos\theta)^{\delta}\,, \qquad 2.2\text{-}2$$

where the ensemble (c, α, β, γ, δ) are fit coefficients for the specific dependent feature characteristic Y, which represents the crater depth, diameter, *etc.* These may be inverted easily to solve for an unknown independent characteristic, usually the projectile diameter d_p, if the impact velocity and angle are known or can be assumed. Other independent parameters are assumed, determined by analysis - such as Scanning Electron Microscopy-Electron Dispersive X-ray (SEM-EDX) analysis of craters to determine projectile residue material(s) and hence source (micrometeoroids or orbital debris) and mass density – or

estimated in simulation by sampling over distributions in impact parameters (*e.g.,* impact angle and velocity).

Extensive hypervelocity impact range testing has yielded sufficient data to formulate damage equations for the returned surfaces used in the ORDEM 3.1 development and validation efforts. Specifically, damage equations have been developed for STS windows (crater depth and diameter), STS radiators (facesheet craters and penetrations, thermal tape hole diameter), the WFPC-2 radiator (crater depth, crater average diameter, crater maximum length, paint spallation zone average diameter, and paint spallation zone maximum length), and HST MLI blankets (penetrations). These are discussed in detail in Section 2.4.1 for STS windows and radiators and in Section 3.3.1 for the HST WFPC-2 radiator and MLI.

2.2.3 Size Estimates for Optical Data Sources

The observable parameter for solar-illuminated targets from ground-based optical sensors is the apparent brightness or apparent magnitude of the target. To calculate the size of a target, defined for optical targets as the observed diameter of a sphere at a distance R, the apparent magnitude is first converted to absolute magnitude, $M_{abs}(filter)$, provided the bandpass/filter, distance, and phase angle. Phase angle, α, is defined as the angle subtended by sensor-target-sun. For the purposes of the calculation of size, the filter v is shown in Equation 2.2-3, but this is easily replaced with a bandpass provided the magnitude of the sun in the specific filter is known.

The size or diameter, d, of each target is inferred from its absolute magnitude assuming a given geometrical albedo of the object's surface, A_g, a phase function, $\Psi(\alpha)$, which defines how sunlight is scattered by the surface in a direction α to the observer, and range, R:

$$d = \frac{2 \cdot R}{\left[\pi \cdot A_g \cdot \Psi(\alpha)\right]^{0.5}} \cdot 10^{\left[\frac{M_{abs}(v) + M_{sun}(v)}{-5.0}\right]} \qquad \text{2.2-3}$$

where $M_{sun}(v)$ is the apparent magnitude of the sun in the visible filter.

The two phase functions that apply to spacecraft and debris – both of which are most likely present in a given optical dataset – are the specular equation, which is independent of phase angle:

$$\Psi(\alpha) = \frac{1}{4\pi} = 0.079579 \qquad \text{2.2-4}$$

and the diffuse Lambertian equation:

$$\Psi(\alpha) = \frac{2}{3 \cdot \pi^2}[sin(\alpha) - (\pi - \alpha) \cdot cos(\alpha)] \qquad \text{2.2-5}$$

where $\Psi(0)$ = 0.212207.

The ratio of the specular to diffuse Lambertian phase functions is approximately 0.375 at a phase angle of 0°, and the ratio of corresponding sizes is 0.612. Thus, if a brightness or magnitude is converted to a size under a diffuse Lambertian assumption, it is 0.612 times smaller than the size determined under a specular assumption. For example, an object with a 60 cm specular size becomes a 36.7 cm object under a diffuse Lambertian assumption. A comparison between the specular and Lambertian phase functions is shown in Figure 2-3.

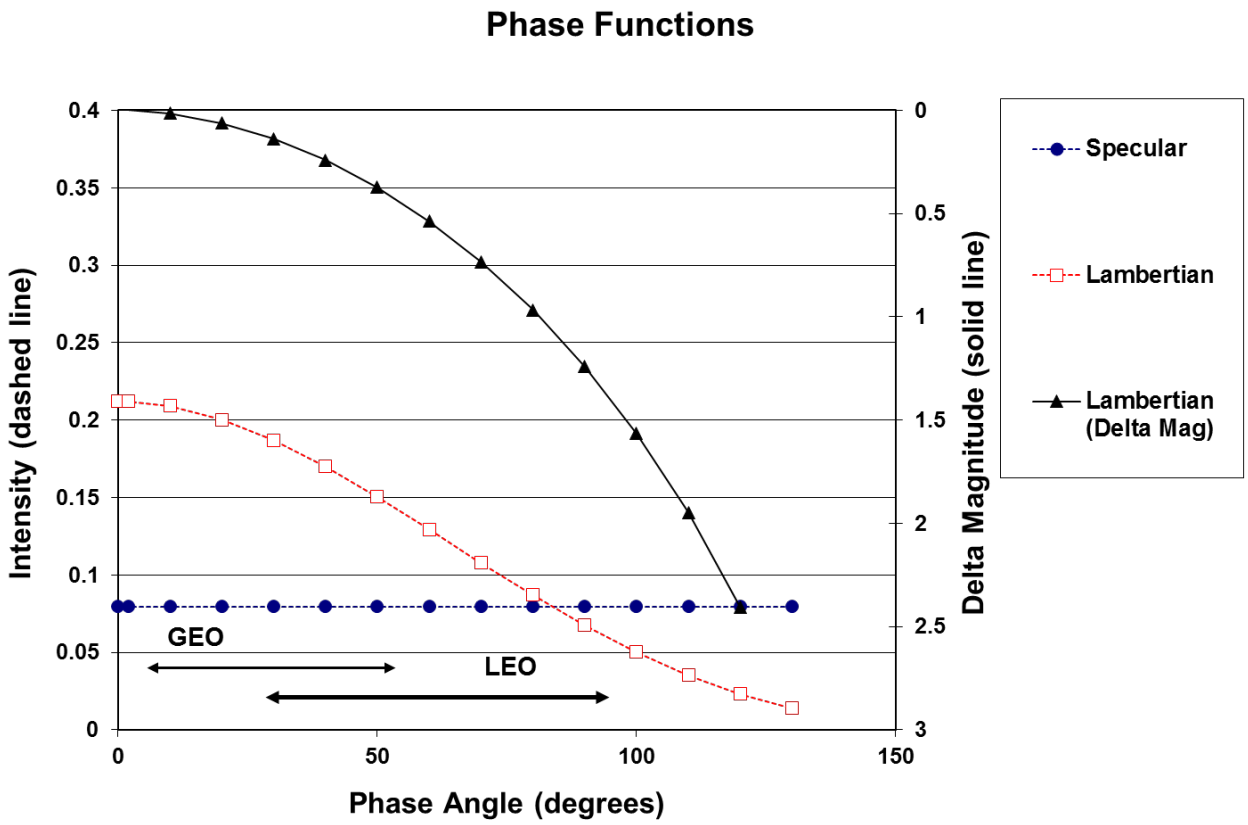

Figure 2-3: Specular and diffuse Lambertian phase functions. The right axis gives the intensity change in the Lambertian phase function with respect to 0° phase angle in terms of magnitudes.

The policy of the Inter-Agency Space Debris Coordination Committee is to correct observed magnitudes using a uniform phase function (a diffuse Lambertian phase function at a phase angle of 0°). The diffuse Lambertian phase function is similar to the empirical phase function that represents the lunar soil in the phase angle range for LEO targets. The details of the lunar phase function are dependent on the physical structure of the top layers of the lunar soil and is not relevant to solid surfaces. Consequently, the diffuse Lambertian phase function is preferred for spacecraft and debris whose surfaces are solid and rough and is used for the optical data considered here.

2.2.4 Uncertainty in Reported Counts

Count data from orbital debris measurement sources are assumed to follow Poisson statistics, and Poisson-based empirical standard errors are reported for measurement data with respect to uncertainty in the count values. Implicit in the assumption of a Poisson model is a constant count rate, as well as counts that occur one-at-a-time. Alternate distributions for modeling overdispersed (negative binomial) and underdispersed (generalized Poisson) data are available (Xu & Stokely, 2005), but past work for orbital debris observations using radar have shown that the assumptions requisite for using a Poisson model are met (Stokely, Benbrook & Horstman, 2007), and that the data are well-modeled by a Poisson distribution.

The Poisson distribution is defined in Equation 2.2-6 below. Debris counts, k, where k is an integer, are drawn from a Poisson distribution with mean λ. Note that the Poisson model is a single parameter model, and the variance is equal to the mean, λ, as well. Figure 2-4 shows a family of Poisson distributions where the mean, λ, is varied. The Poisson distribution may be rewritten in terms of the count rate as

shown in Equation 2.2-7, where in this case *r* is the count rate and T is the observation time for counting orbital debris.

$$k \sim \text{Poisson}(\lambda) = e^{-\lambda}\frac{\lambda^k}{k!} \qquad \text{2.2-6}$$

$$\text{kT} \sim \text{Poisson}(\text{rT}) = e^{-\text{rT}}\frac{(\text{rT})^k}{k!} \qquad \text{2.2-7}$$

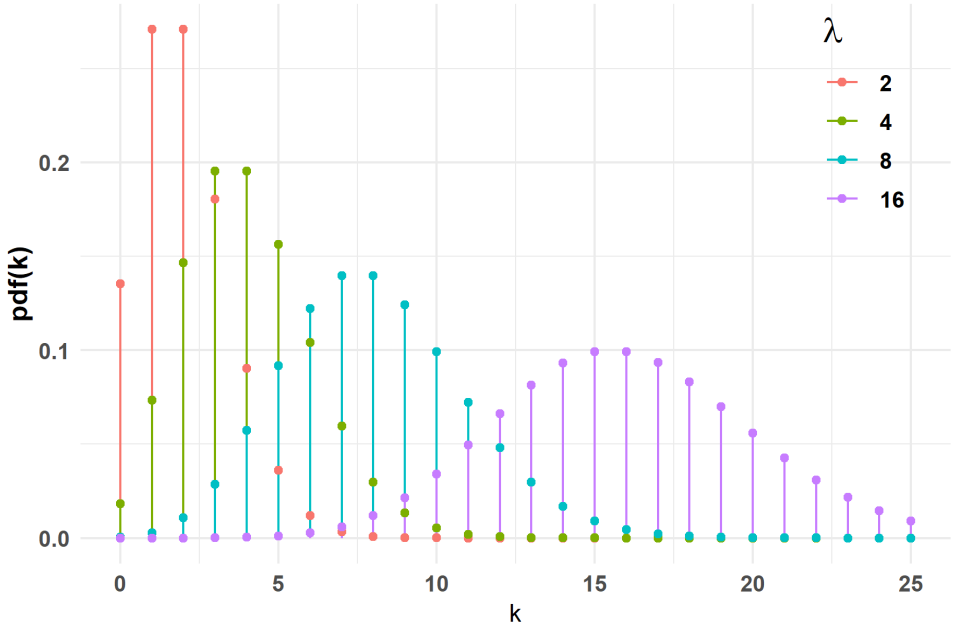

Figure 2-4. Poisson distributions with λ = 2, 4, 6, 8, and 16.

To determine a confidence interval for the reported debris count, *k*, standard errors are defined in a similar manner as that from a standard normal distribution. The upper and lower bounds are determined based on cumulative probabilities. In the case of the standard normal distribution, the upper (σ) and lower (-σ) bounds are such that the probability between ±σ is approximately 68.2% as depicted in Figure 2-5, where we note that since this is a standard normal distribution, σ = 1. The cumulative probabilities for the lower and upper bounds may be calculated from the quantiles of the cumulative distribution function for a standard normal to verify the interior probability is 68.2%.

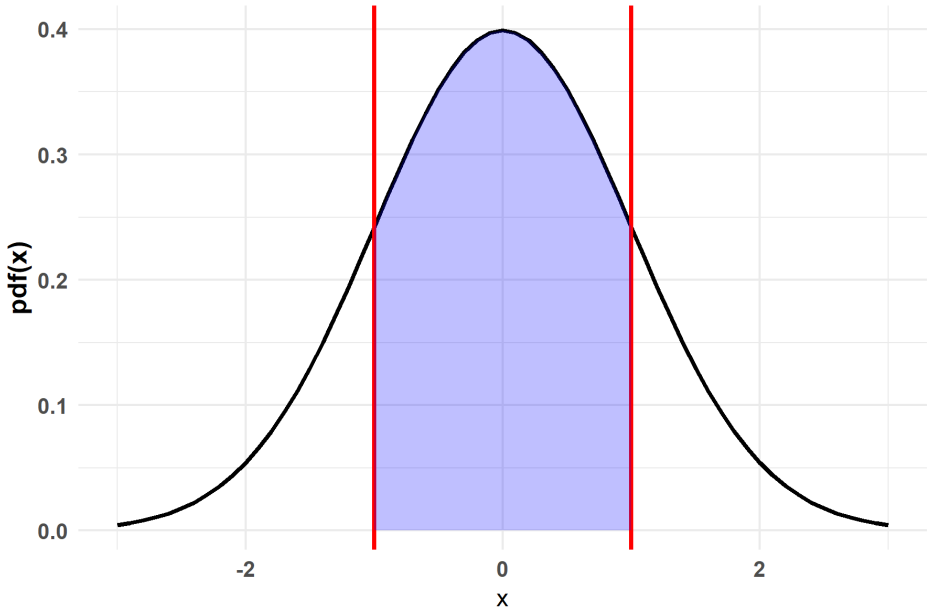

Figure 2-5. Standard normal distribution with the probability between ±σ highlighted.

The confidence interval for the parameter, λ, may similarly be found using quantiles calculated from a Gamma distribution – the cumulative distribution function for the Poisson and Gamma distribution are related – with shape parameters *k* and k+1 as shown in Equation 2.2-8, and α/2 and 1 – α/2 are set to obtain the quantile of interest. The scale parameter in this quantile function is set to unity.

$$F^{-1}(\alpha/2\,;k;1) \leq \lambda \leq F^{-1}(1-\alpha/2\,;k+1;1) \qquad 2.2\text{-}8$$

Alternatively, the use of the quantile function for a chi-squared distribution may be used, as shown in Equation 2.2-9, since the chi-squared distribution is a special case of the Gamma distribution. This and additional information on the generation of these relations may be found in (Johnson, Kemp & Kotz, 2005). The alternate form may be useful in cases where the Gamma distribution is not readily available or for use with tables where the cumulative density function for the chi-squared distribution is commonly tabulated.

$$\frac{1}{2}\chi^2(\alpha/2\,;2k) \leq \lambda \leq \frac{1}{2}\chi^2(1-\alpha/2\,;2k+2) \qquad 2.2\text{-}9$$

It should be noted that Poisson confidence intervals are always approximate due to the discrete nature of the underlying distribution, which is a well-known issue discussed in the previously cited reference. The approximation is less accurate for low counts with an exactly specified quantile. To demonstrate this, the probability between upper and lower standard errors – using Equation 2.2-9 – versus count number, *k*, is plotted in Figure 2-6. It is observed that as *k* increases the probability between the limits of the confidence interval asymptotically approaches that of the standard normal, 68.2%. A standard normal is often used to simplify the calculation of the standard errors when k is large.

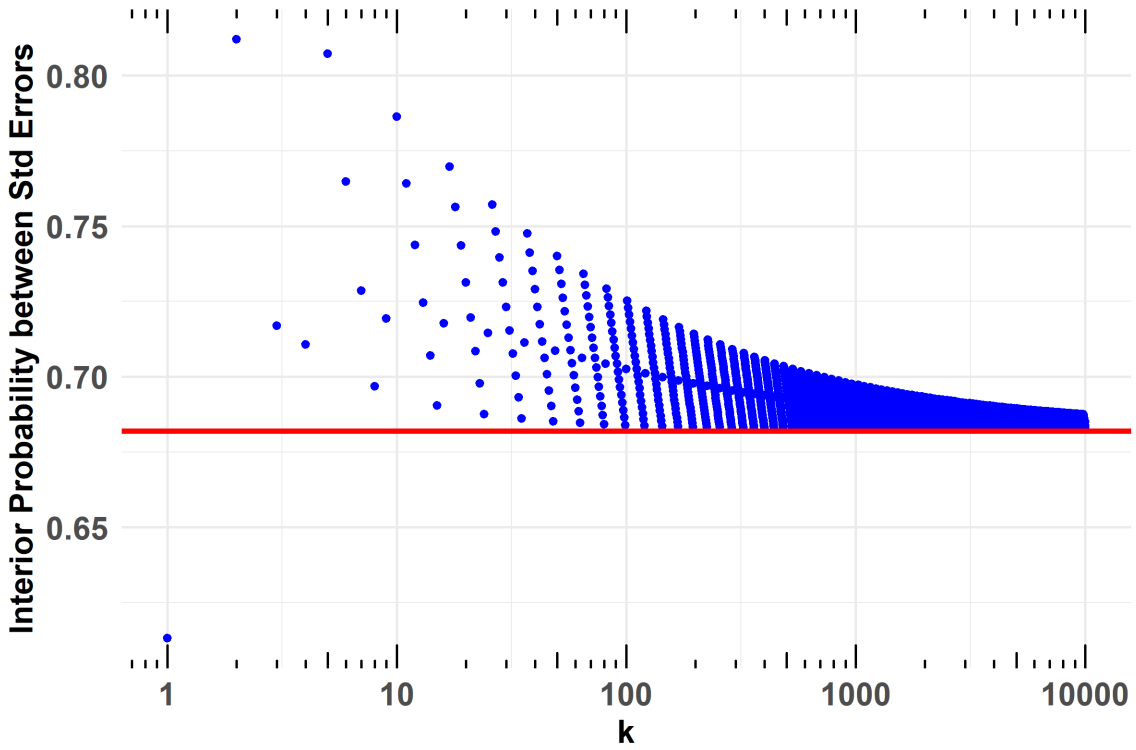

Figure 2-6. Probabilities between standard errors calculated with an upper limit using 2k + 2 degrees of freedom.

An improvement may be made to the approximate confidence interval specified in Equation 2.2-9, such that the probability between the upper and lower limits of the interval have a smaller mean square deviation from the 68.2% probability line. This modified confidence interval calculation is shown in Equation 2.2-10, where the lower limit calculation remains the same, but the degrees of freedom is reduced from 2k + 2 to 2k for the upper limit. The difference between the upper and lower cumulative probabilities versus the count number *k*, are plotted in Figure 2-7. This plot, which oscillates around the 68.2% line, has a smaller mean square deviation on average than the approximation detailed in Figure 2-6. As a result of this, uncertainty in the reported counts for all orbital debris count measurements shown in this report use this latter relation. A summary of the lower and upper standard errors for the first 10 counts are shown in Table 2-1. Also included in this table are the equivalent 95% confidence intervals, where α = 0.05. The two σ-confidence intervals are shown in Table 2-1 for reference only, and only the one σ values are used for reporting uncertainty in the orbital debris counts.

$$\frac{1}{2}\chi^2(\alpha/2\,;2k) \le \lambda \le \frac{1}{2}\chi^2(1-\alpha/2\,;2k) \qquad 2.2\text{-}10$$

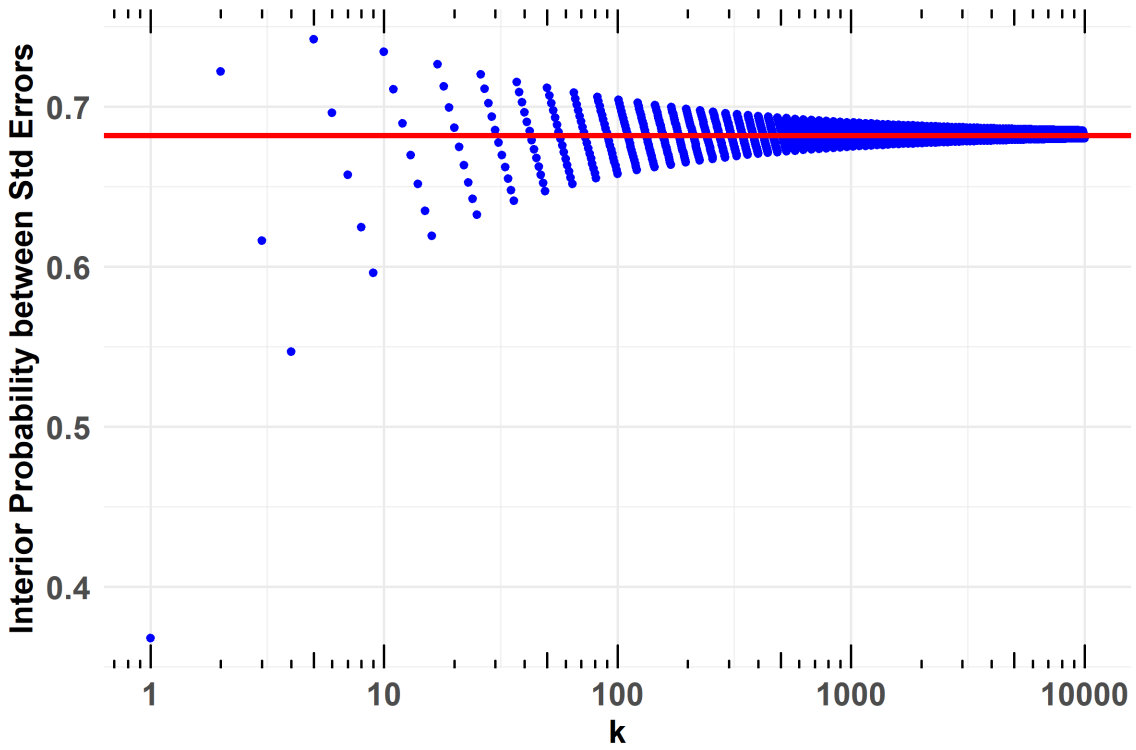

Figure 2-7. Probabilities between standard errors calculated with an upper limit using 2k degrees of freedom.

Table 2-1. Lower and upper limits for the confidence interval on observed counts, *k*, assuming a one σ definition for the quantiles α/2 and 1- α/2.
The 95% confidence interval, α=0.05, is included in the last two columns.

k	*lower*	*upper*	*α /2*	*1- α /2*
1	0.1727538	1.841022	0.02531781	3.688879
2	0.7081854	3.299527	0.24220928	5.571643
3	1.3672953	4.637860	0.61867212	7.224688
4	2.0856608	5.918186	1.08986537	8.767273
5	2.8403089	7.162753	1.62348639	10.241589
6	3.6200686	8.382473	2.20189425	11.668332
7	4.4185295	9.583642	2.81436305	13.059474
8	5.2316139	10.770281	3.45383218	14.422675
9	6.0565390	11.945142	4.11537310	15.763189
10	6.8913056	13.110204	4.79538870	17.084803

2.2.5 Radar Data and Model Size Comparisons

Comparisons between radar data and ORDEM are often made using the output of ORDEM's telescope mode, which outputs the yearly radar surface area flux in terms of debris size. This size represents an intrinsic object size, while sizes for radar data measurements are determined using the NASA SEM, as described in Section 2.2.1, which is a model fit to measured RCS data. The model fit provides a one-to-one mapping between a measured RCS and a SEM size. For a given RCS, however, there is uncertainty

regarding the actual physical size of the object measured. This uncertainty can be considered from the individual datapoints in Figure 2-2, where for a given RCS, variation in the actual object size that produced a given RCS can be observed – which for some RCS values represents a significant variation in size. An alternate characterization of the uncertainty is obtained by viewing the RCS-to-SEM size model as a conditional probability distribution. Conditioning on a given wavelength normalized size, *x*, the conditional density as a function of normalized RCS, is shown in Figure 2-8 – for several different wavelength-normalized sizes.

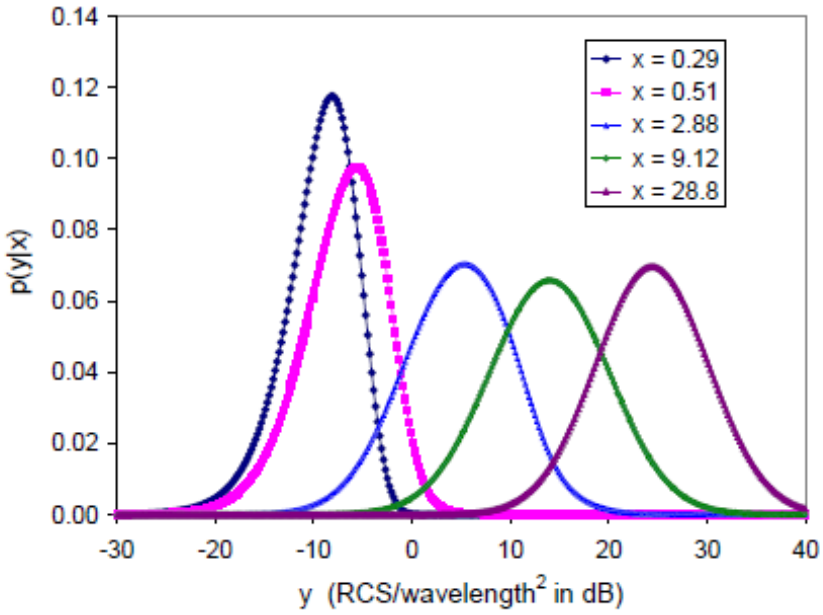

Figure 2-8. Normalized RCS distributions, inherent to the NASA SEM model, obtained by conditioning on several different wavelength-normalized sizes.

For a true comparison between the collected HUSIR and Goldstone data and the model predictions, it is necessary to reconstruct the uncertainties inherent in the RCS-to-SEM size conversion. To do this, a Monte Carlo sampling of the ORDEM telescope mode output, as an RCS distribution using the NASA SEM model to generate a corresponding probabilistic distribution of predicted sizes, is conducted. Comparisons between model and radar measurements are made on the basis of a cumulative size – up to a given size and larger. Based on the method of comparison, the Monte Carlo samples are weighted according to their likelihood of contributing to a given size, and these contributions are added together – up to the physical size being estimated. This process accounts for the effects that the distribution of RCS of orbital debris has on the SEM size predictions and provides a more consistent metric for comparison between the model and data. All charts comparing surface area and cumulative flux to radar measurements in this report were produced using this process.

2.3 RADAR-BASED POPULATIONS

2.3.1 HUSIR 2013–2015 Radar Data

Data from HUSIR, which is operated by the Massachusetts Institute of Technology (MIT) Lincoln Laboratory, for the calendar years 2013–2015 was used to build the populations for orbital debris having a size, as determined by the NASA SEM, of greater than approximately 5.5 mm in LEO. HUSIR data is collected on a U.S. Government fiscal year (FY) basis, and the data included for these population builds is from FY2014–2015 (corresponding to the last quarter of calendar year (CY)2013 through the third

quarter of CY15). This is the first time that data from HUSIR, previously Haystack, was available for inclusion with ORDEM. Haystack underwent upgrades starting in FY2010, which continued through the end of FY2013, when the radar was re-commissioned as HUSIR.

HUSIR orbital debris observations are conducted with the radar operated in a fixed beam mode rather than a typical tracking mode for the radar. Hence the radar, with its 0.058° 3-dB two-sided beamwidth at 10 GHz, is pointed at a fixed elevation and azimuth angle with respect to the local topocentric coordinate system, and objects pass through the radar beam. The two pointing geometries for data collection considered in this report are 75° elevation or 15° from zenith, due East – referred to as 75E – and 20° elevation or 80° from zenith, due South – referred to as 20S. The majority of observations are from the 75E pointing geometry because of the increased orbital altitudes that are observed with this pointing. Fewer observations are typically conducted for the 20S pointing because of the longer slant range to debris in a given orbital altitude and the fact that there is a $1/R^4$ dependence for the received power, where R is the slant range. Provided the dependence on altitude for radar performance, the HUSIR radar is complete down to approximately 5.5 mm at 1000 km, and 1 cm at 1600 km altitude for the 75E pointing geometry. For the 20S pointing geometry, HUSIR is considered complete to approximately 2 cm out to 1000 km altitude. Although observations from the 20S pointing are more limited, that dataset provides coverage of lower inclination bands that are not accessible with 75E pointing geometry.

A composite of the HUSIR 2013–2015 75E datasets was used to scale the initial populations modeled using NASA's LEO-to-GEO ENvironment Debris (LEGEND) model (see Appendix A for details) and is used here for verification purposes. This composite dataset represents a weighted average of the individual CY2013–2015 datasets, where the number of detections for a given size, range, *etc.* and for a given year was weighted by the number of observation hours for that year divided by the total observation hours across all three years.

2.3.2 Surface Area Flux vs Altitude

In LEO, to provide a verification method between the measurement data and ORDEM, the surface area flux is used for radar data. This surface area flux is defined in terms of the number of debris objects that pass through the radar beam, divided by the surface area of the radar beam – assuming the 3-dB beamwidth of the radar – per unit time, in this case on a yearly basis. See Section 2.2.5 for details on preparation of the model predictions for comparison with radar data measurements, specifically conversion of the ORDEM intrinsic debris sizes to an RCS distribution, and subsequent conversion to SEM size.

To further refine the comparison between radar data and the model, the surface area flux comparison is presented by altitude, to the extent of the coverage completeness. The observation-hour-weighted composite HUSIR data from 2013–2015 is shown in Figure 2-9 for sizes > 1 cm and in Figure 2-10 for sizes > 5.5 mm. The data uncertainties shown are the one σ-confidence intervals described in Section 0. A curve for the ORDEM 3.0 model prediction is included in the plots for comparison. All comparisons with ORDEM 3.0 are for reference only. Note that good agreement between ORDEM 3.1 and the measurements is obtained, and statistically the model is generally a good fit to the data – particularly at altitudes with higher detection rates. Comparison with the ORDEM 3.0 model prediction indicates a significantly improved match to the data using ORDEM 3.1. The ORDEM 3.1 curve should, however, match the data in this instance well – and it does – since the HUSIR data were used to build the model, whereas the ORDEM 3.0 result is a prediction of the environment at this point in time based on older measurements and SSN catalog data.

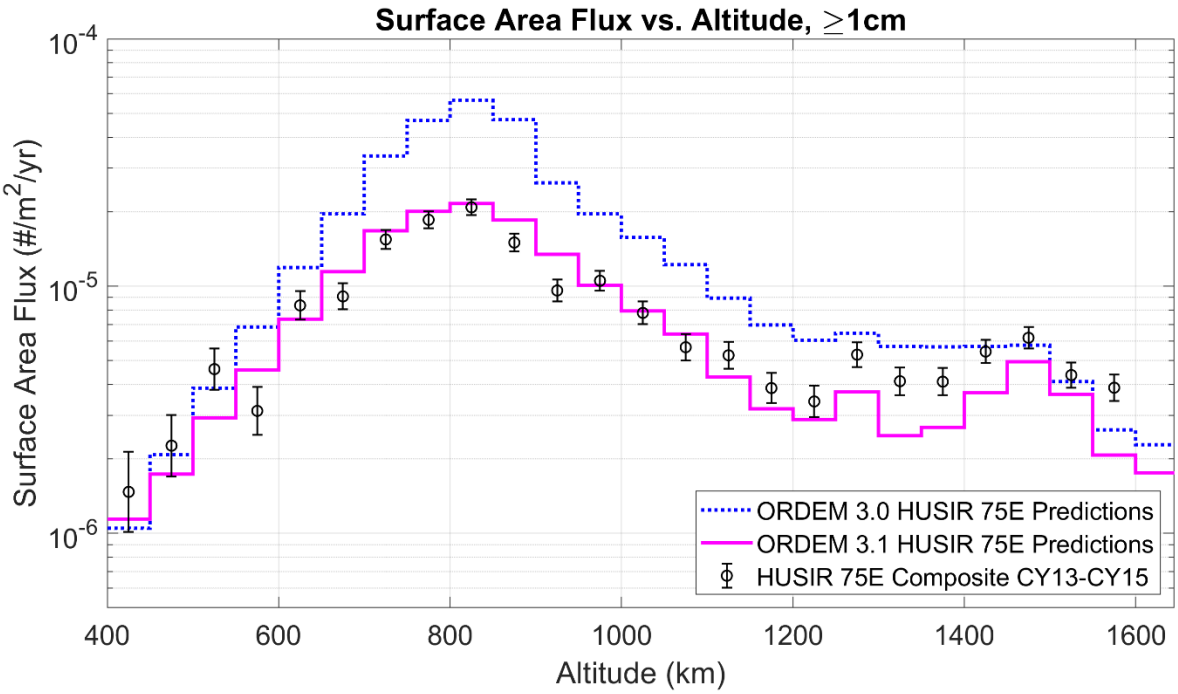

Figure 2-9. Comparison of the surface area flux vs altitude for a limiting size of 1 cm and larger between ORDEM 3.0, ORDEM 3.1, and measurements from HUSIR 75E.

Figure 2-10 shows the comparison of surface area flux as a function of altitude for sizes 5.5 mm and larger. Note that the model is again in good agreement with the data for most of the altitude bins, with one σ-confidence intervals shown.

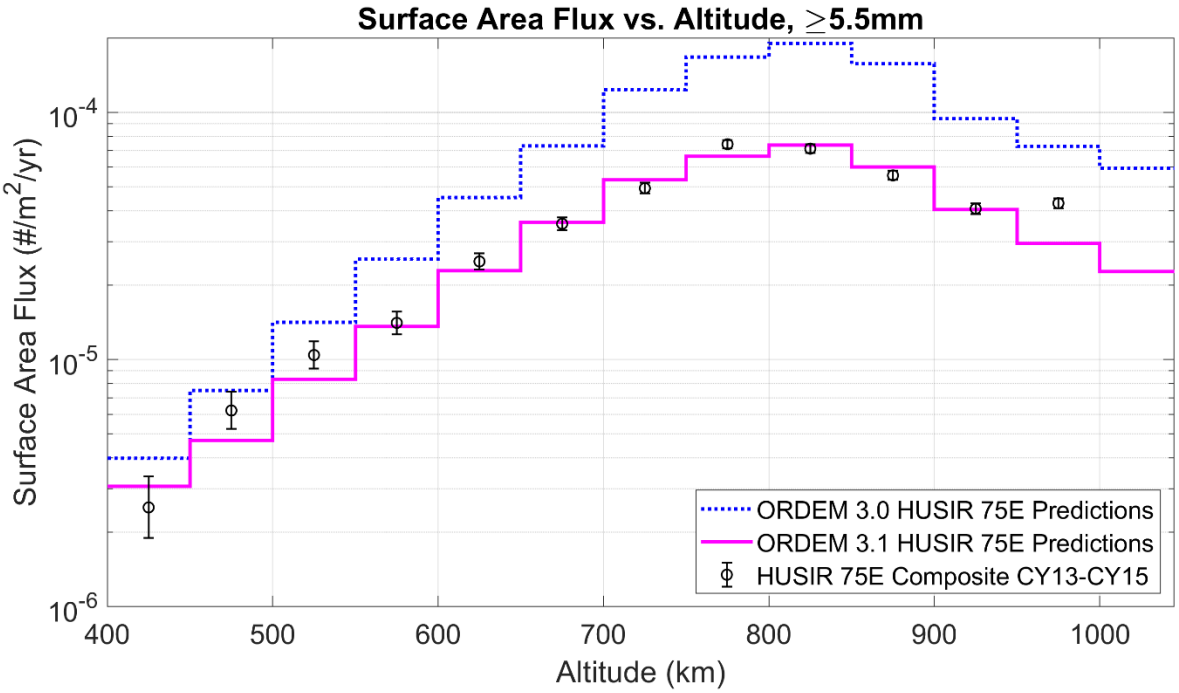

Figure 2-10. Comparison of the surface area flux vs altitude for a limiting size of 5.5 mm and larger between ORDEM 3.0, ORDEM 3.1, and measurements from HUSIR 75E.

2.3.3 Surface Area Flux vs Size

An alternate view of the surface area flux comparison between the model and data are available as a function of debris size. In this section, comparisons are shown for the composite data from altitudes up to 1000 km, as well as by breaking down the surface area flux as a function of size in key altitude bands of interest to NASA missions. Sizes reported are again based on the NASA SEM (Section 2.2.5).

In Figure 2-11, a comparison of the surface area flux versus debris size is shown between ORDEM 3.0 predictions, ORDEM 3.1, and HUSIR data. The dataset is limited to the 400–1000 km altitude band, and the upper limit on the size axes is set to 10 cm, which is the size at which the SSN catalog takes over from radar measurements for model comparison purposes. HUSIR is noise-limited for sizes smaller than about 5.5 mm at 1000 km, which is evident in the roll-off in the surface area flux near 5 mm. It is observed that ORDEM 3.1 is an excellent model fit to the data for altitudes between 400 and 1000 km and above the lower size limit of the HUSIR data.

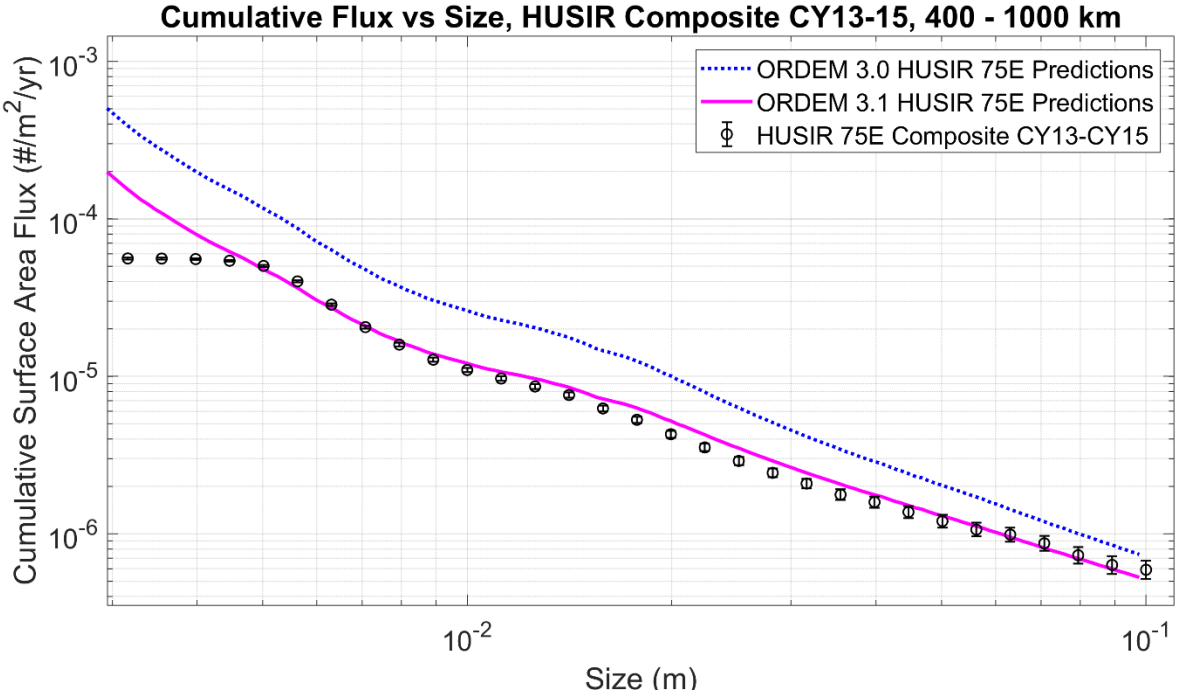

Figure 2-11. Comparison of the surface area flux vs SEM size between ORDEM 3.0, ORDEM 3.1, and measurements from HUSIR 75E. The altitude is restricted to 400–1000 km.

Further comparisons between the model and data on the basis of debris size for key NASA mission altitude regions (Table 2-2) are shown in Figure 2-12, Figure 2-13, Figure 2-14, and Figure 2-15, which correspond to nominal mission altitudes for the International Space Station (ISS), HST, the Afternoon or A-Train Constellation – a coordinated group of Sun-synchronous, Earth-observing satellites crossing the equator in an ascending (northbound) direction at approximately 1:30 pm local solar time (NASA, 2022), and NOAA 20, respectively. Identifiers and nominal operational altitudes for these missions are shown in Table 2-2. In the case of the first two missions, additional *in situ* data sources are available. These additional data sources are used as verification that the model is performing well for size regimes below the radar detection thresholds at these critical altitudes (see Section 2.4.3).

Table 2-2: Nominal operational altitudes for key NASA missions of ISS, HST, A-Train, and NOAA 20.

Name	International Designator	SSN #	Nominal Altitude Range (km)
International Space Station (ISS)	1998-067A	25544	400–450
Hubble Space Telescope (HST)	1990-037B	20580	550–600
A-Train Constellation	Multiple	Multiple	700–750
NOAA 20	2017-073A	43013	800–850

Surface area flux comparisons in Figure 2-12 through Figure 2-15 show good agreement between the ORDEM 3.1 model and data. For the ISS and HST altitudes (Figure 2-12 and Figure 2-13), the population density is less than at A-Train and NOAA 20 altitudes (Figure 2-14 and Figure 2-15), and fewer debris counts results in wider confidence intervals – particularly for debris several centimeters and larger. In all cases, however, ORDEM 3.1 provides a better fit to the data than the ORDEM 3.0 predictions.

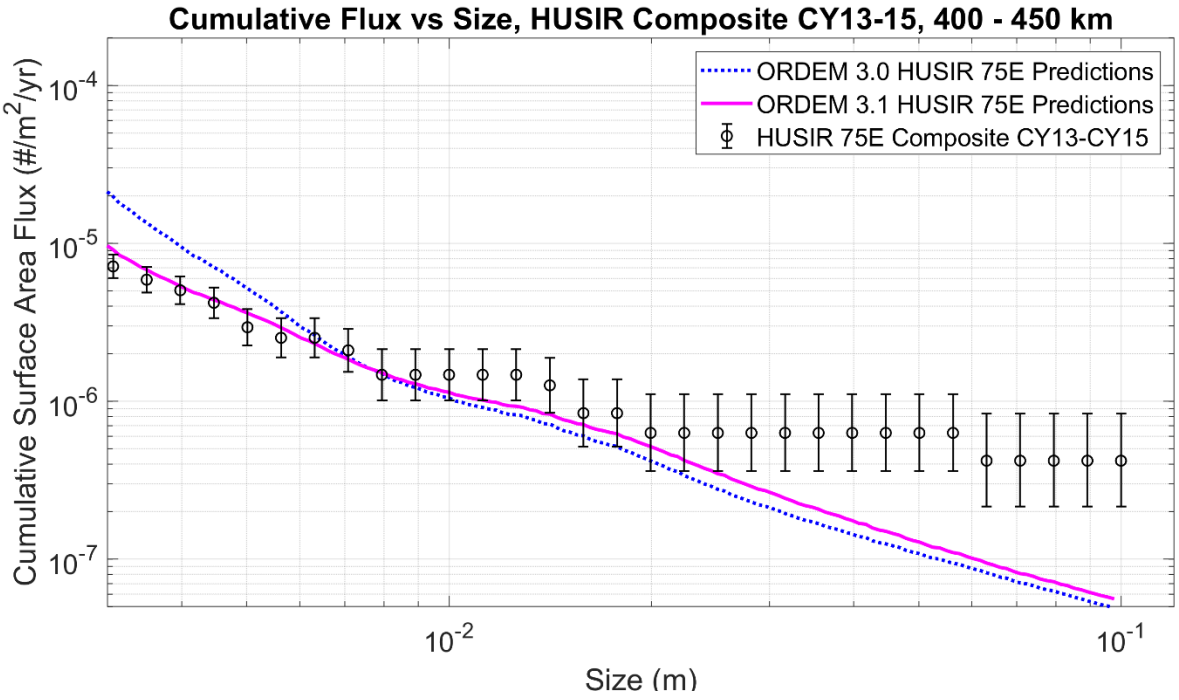

Figure 2-12. Comparison of the surface area flux vs SEM size between ORDEM 3.0, ORDEM 3.1, and measurements from HUSIR 75E. The altitude is restricted between 400 km and 450 km. The relatively large deviation observed for the larger object sizes in this plot is due to the low counts observed for these sizes in this altitude band, which is evident from the large uncertainties associated with these sizes. For sizes 2 cm and smaller, however, the model is an excellent fit relative to the data.

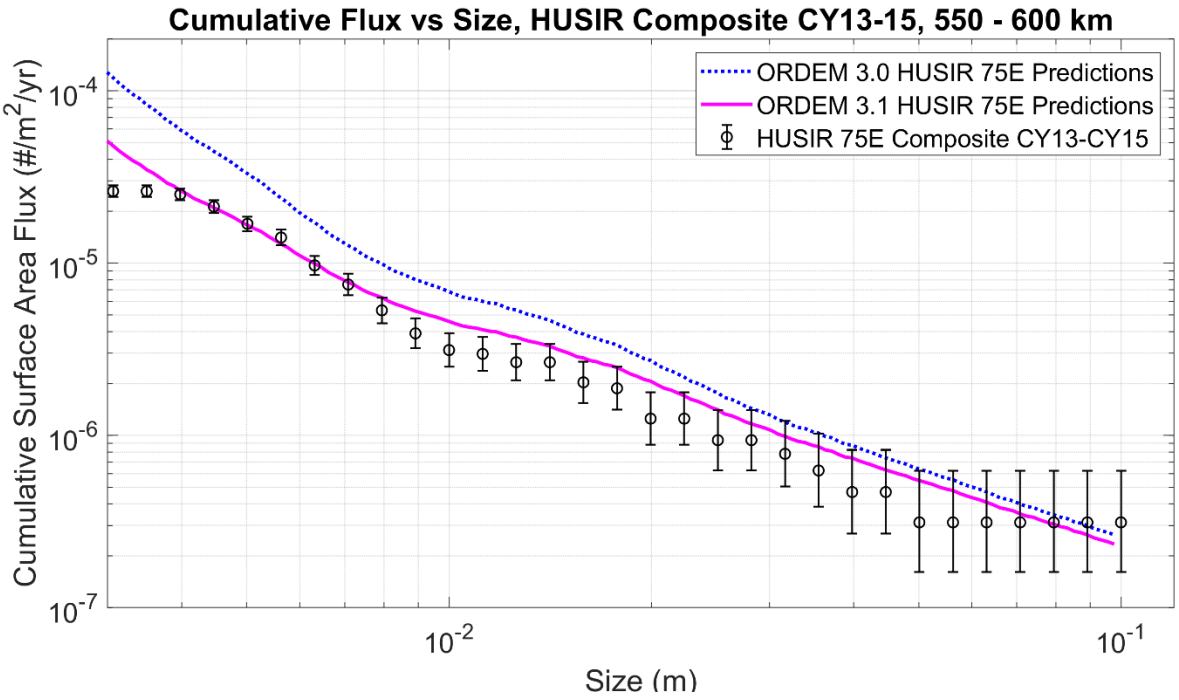

Figure 2-13. Comparison of the surface area flux vs SEM size between ORDEM 3.0, ORDEM 3.1, and measurements from HUSIR 75E. The altitude is restricted to 550–600 km.

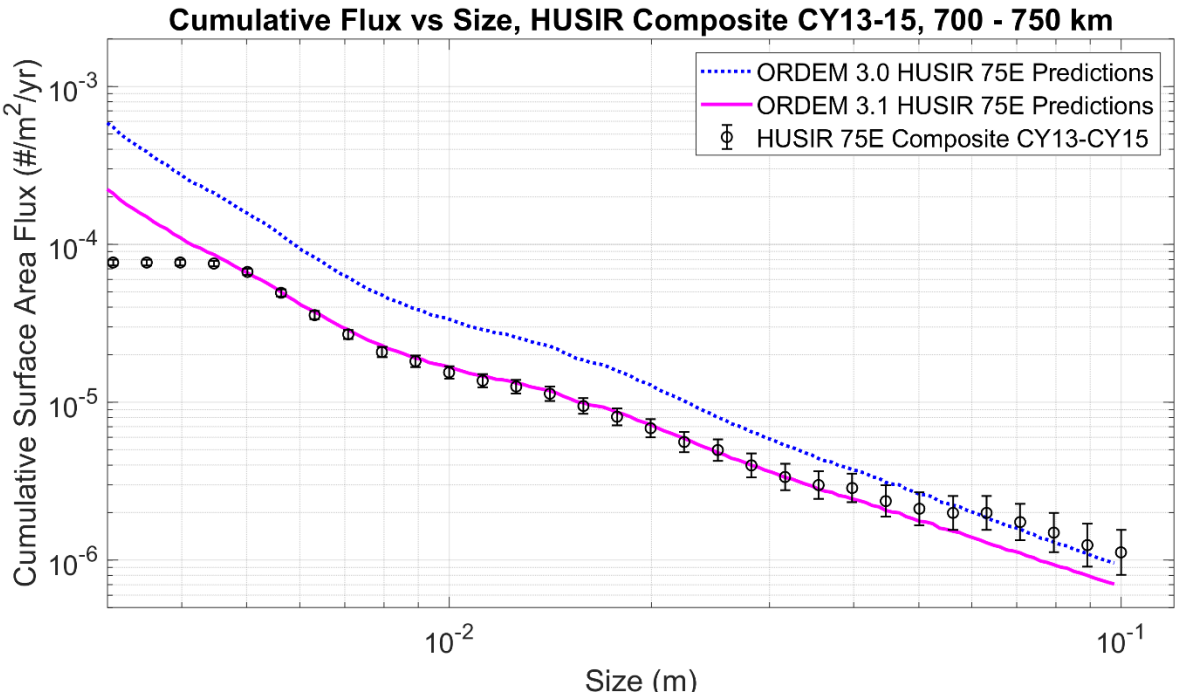

Figure 2-14. Comparison of the surface area flux vs SEM size between ORDEM 3.0, ORDEM 3.1, and measurements from HUSIR 75E. The altitude is restricted to 700–750 km.

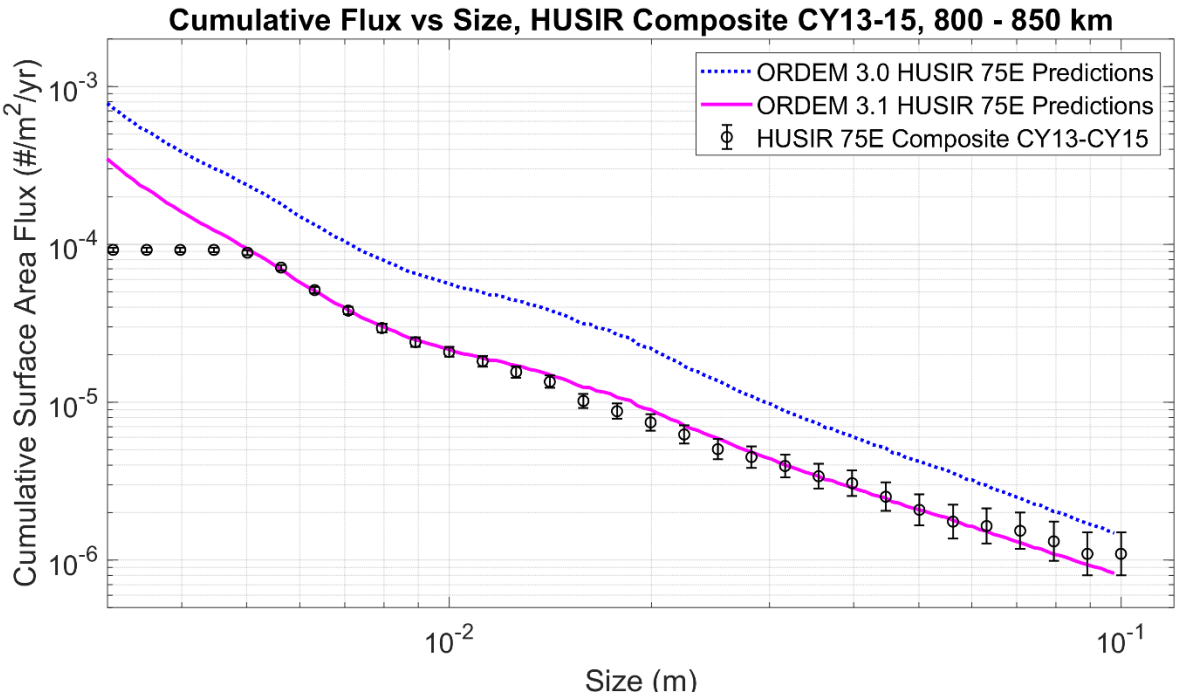

Figure 2-15. Comparison of the surface area flux vs SEM size between ORDEM 3.0, ORDEM 3.1, and measurements from HUSIR 75E. The altitude is restricted to 800–850 km.

2.4 IN SITU-BASED POPULATIONS

2.4.1 In situ Impact Data

The STS impact record, as defined by the NASA Hypervelocity Impact Technology (HVIT) group's Shuttle Impact Database (21 February 2012 edition), was used to scale the initial modeled degradation populations based on a reference particle production rate to establish the final, scaled, small debris population for ORDEM 3.1 (discussed in the ORDEM 3.1 Process Document Section 3.2). STS window impact craters and radiator perforations were used in building both ORDEM 3.0 and 3.1, but the data was reanalyzed for ORDEM 3.1. Radiator perforations were used to verify that the resulting degradation populations are consistent with the datasets.

STS radiators exposed an aluminum (Al) 2024-T8 facesheet covered with silver-Teflon thermal tape, with a total surface area of approximately 119 m^2 distributed among eight panels, that remained protected during liftoff and descent. Three types of damage to the radiators were typically recorded, including thermal tape holes, facesheet craters, and facesheet perforations. The thermal tape had a hole size with its own damage equation, but there were concerns about the accuracy of that data. There were also two types of craters, one that did not perforate the facesheet (in which case the depth of the crater was recorded), and one where the particle perforated the facesheet (in which case the diameter of the perforation was preserved). Because of the small size of the non-perforating craters, the completeness of that data set is in question. However, the inspection teams were generally more concerned with complete perforations and possible risk to the orbiter, so that dataset is expected to be more complete. Thus, only the dataset for facesheet perforations was used for building and verifying the ORDEM 3.1 populations.

A total of 67 STS missions were examined for impacts post-flight in radiator surveys. A total of 640 impact features were observed for a flight average of 9.6 impacts. Of these, 81 were facesheet

perforations. Type categorization, based on SEM-EDX analysis of impact feature residues, was 70% (450) unknown; 13% (86) micrometeoroids (MM); and 16% (104) orbital debris (OD).

Facesheet perforations were examined in detail, and additional, detailed SEM-EDX analyses were sponsored by the NASA Orbital Debris Program Office (ODPO) in 2012 for ORDEM 3.0 development. For ORDEM 3.1 development and validation purposes, constituents were classified as low density (LD; $\rho < 2$ g/cm^3), medium density (MD; $2 \leq \rho \leq 4.5$ g/cm^3), or high density (HD; $\rho > 4.5$ g/cm^3). LD constituents were treated as medium-density objects in the development of ORDEM populations, due to the limited number of debris impactors in this density regime. Figures 2-16 and 2-17 illustrate the breakdowns in the perforation distribution and identified orbital debris sources, respectively.

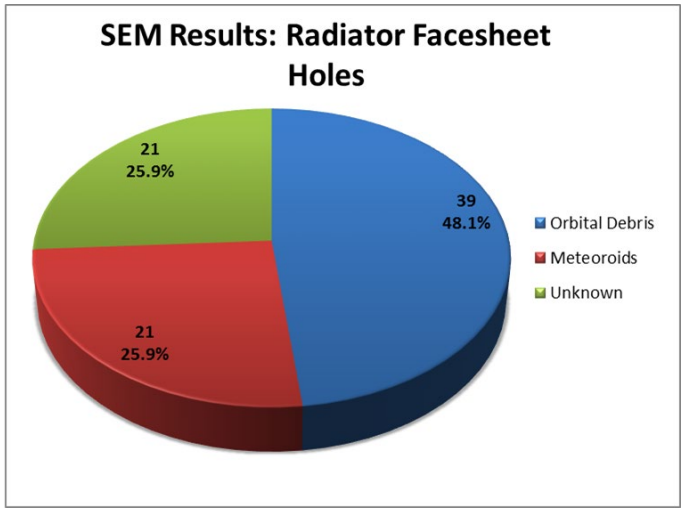

Figure 2-16. Breakdown by source for STS radiator perforations. Annotations indicate absolute number (out of 81) and percentage of that total.

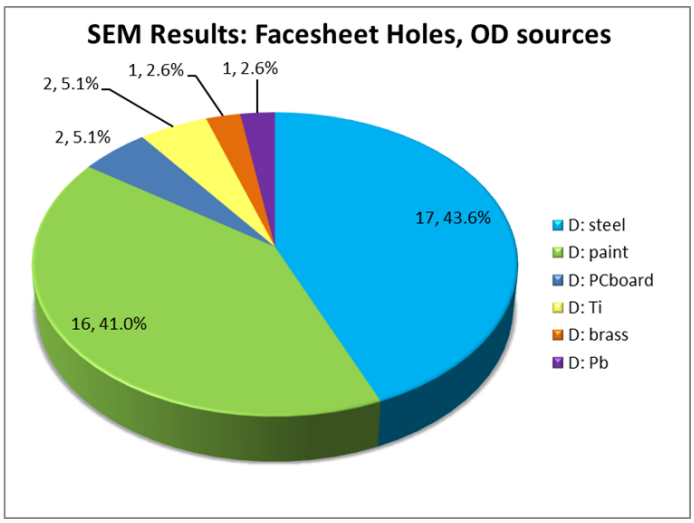

Figure 2-17. STS radiator orbital debris perforations by material type. The “D” prefix in the legend for each material type refers to the identification of the impactor as debris versus the other possible classifications of micrometeoroid or unknown. Note that Al is not present as Al traces cannot be distinguished from the radiator’s Al substrate. Annotations indicate absolute number (out of 39) and percentage of that total.

Since Al impactors could not be identified on the Al radiator surfaces, the unknown radiator perforation impactors were reclassified to approximately match OD/MM and HD/MD proportions seen in similar surveys of the STS windows, resulting in 100% of the Unknown perforation category being reclassified as MD (assumed entirely Al). Even with all of the Unknowns assigned as MD, however, MD was still underrepresented in the radiator perforations as compared to the windows. More details of the SEM-EDX analysis and classification of the window impacts can be found in Section 3.2.2 of the ORDEM 3.1 Process Document.

2.4.2 In situ Estimated Impactor Size

The facesheet perforation diameter damage equation was updated and revalidated for use during ORDEM 3.0 development and used in the ORDEM 3.1 build process. Impactor diameter d_p [mm] was inferred from the facesheet perforation diameter D_{fs} [mm] using the relationship (Hyde, 2015):

$$d_p = \max\begin{cases} 1.6726 \cdot \mathrm{D}_{fs}^{1.045} \cdot \rho^{-0.242} \cdot \mathrm{v}^{-2/3} \cdot (\cos\theta)^{0.151} \\ 1.05 \cdot \rho^{-1/3} \cdot (\mathrm{v} \cdot \cos(\theta))^{-2/3} \end{cases} \qquad 2.4\text{-}1$$

where all variables are as defined in Section 2.2.2.

Using the distribution of particle sizes, inferred from the distribution of measured feature sizes, the flux onto the impacted surface can be determined and compared to the flux predicted by the model. This process is diagrammed in Figure 2-18. There is inherent uncertainty in this method since, for a given feature size, the original size and velocity of the impacting particle is unknown. The same feature could be made by a small particle going fast or a large particle going slow. Thus, assumptions about proper velocities and directions must be made. For ORDEM 3.1 model verification, a probabilistic analysis of the environment and orbiter vehicle surface pointing directions was used to determine distributions in d_p as a function of distributions in relative velocity and impact angle, given a measured radiator perforation diameter. The average of the resulting distribution in d_p was then used to compare fluxes from the available data to those predicted by ORDEM.

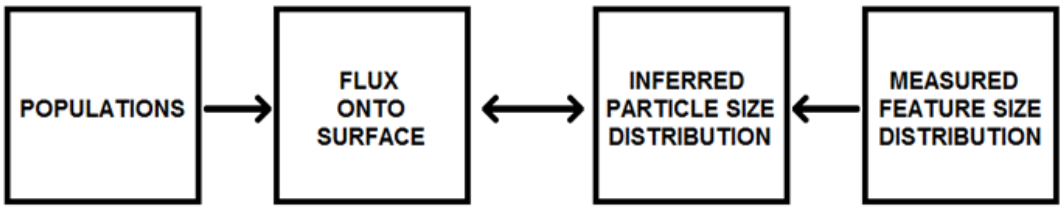

Figure 2-18. General process for comparing modeled fluxes on a surface with the distribution of particle sizes, inferred from the distribution of measured feature sizes, used to verify the degradation population in ORDEM 3.1. Double arrows indicate where comparisons between the model and data are made.

2.4.3 Cumulative Flux vs Size

Comparisons between the model and data on the basis of debris size for key NASA mission altitude regions are shown in Figures 2-19 and 2-20, which correspond to mission altitudes for the ISS and HST, respectively. To verify ORDEM 3.1 fluxes, and to compare with ORDEM 3.0, the counts of STS radiator perforations for missions corresponding to those orbital regimes were accumulated. Radiator perforations leave a physical hole in the facesheet and were considered to gauge the larger, most critical, size regimes of the orbital debris population most accurately. In Figures 2-19 and 2-20, the radiator facesheet perforations were converted to distributions in particle size using the process described in Section 2.4.2. Of the 67 missions for which radiator damage was recorded, impact data from 60 missions were used to

build and verify ORDEM 3.1, due to a lack of availability of detailed time-area product histories for the earliest missions, which is needed to relate feature size distributions to actual orbital populations and fluxes for building the ORDEM 3.1 degradation population. Horizontal uncertainties in Figures 2-19 and 2-20 represent the one σ uncertainties from the distribution obtained in d_p and imply a measure of confidence in the particle-size determination given the observed perforation diameter. Cumulative counts were converted into cumulative cross-sectional area flux by dividing the impact count by the aggregated presented-area-time product over the total duration of the applicable missions. Vertical uncertainties represent the one σ uncertainties in the cross-sectional area flux as computed from the Poisson probability model for uncertainty in reported counts described in Section 2.2.4.

Figure 2-19, representing the flux for the STS missions to the ISS, shows a generally good agreement between ORDEM 3.1 and the flux determined from the STS radiator facesheet perforations, particularly for the smaller sizes where more counts are available. The comparison at higher altitudes – the STS servicing missions to the HST – shown in Figure 2-20 are not quite as good, but there were also significantly fewer impacts seen in the post-mission surveys for the HST servicing missions than for the ISS missions. The model was scaled to best fit the overall radiator perforation data, most of which were at ISS altitudes, thus the model performs better for these lower altitudes.

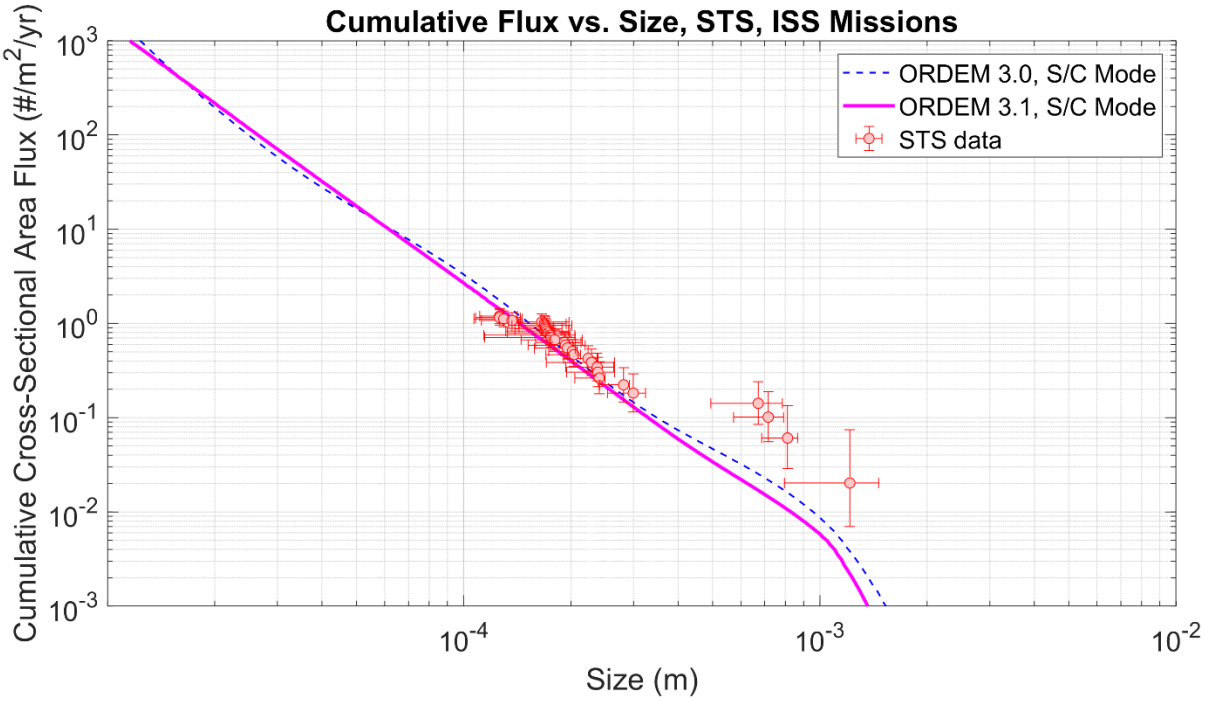

Figure 2-19. Comparison of the cumulative cross-sectional area flux vs. size for ORDEM 3.0, ORDEM 3.1, and the STS radiator perforation data from ISS missions.

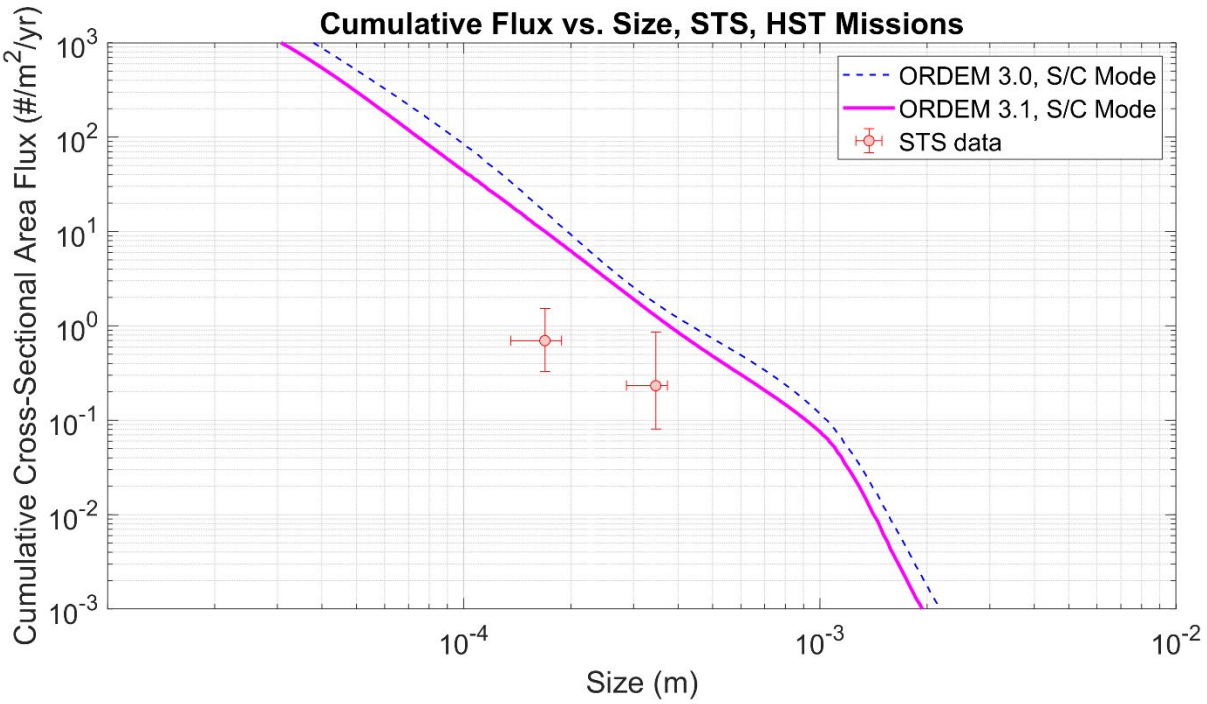

Figure 2-20. Comparison of the cumulative cross-sectional area flux vs. size for ORDEM 3.0, ORDEM 3.1, and the STS radiator perforation data from HST missions.

2.5 OPTICAL-BASED POPULATIONS

2.5.1 Optical Measurements in GEO

For the GEO region, the SSN catalog provides coverage down to a limit of approximately 1 m. To create a more statistically complete GEO population for ORDEM down to 10 cm in size, observations of GEO objects from MODEST were used to build and validate ORDEM 3.1. Data from two observation periods covering 2004–2006 (Abercromby, Seitzer, *et al.*, 2010) and 2007–2009 (Abercromby, Seitzer, *et al.*, 2011) were used for development of the ORDEM 3.1 GEO populations. These are compared to the ORDEM populations in Section 2.5.2 for verification of the model. An additional dataset from 2013–2014, used for model validation, is discussed in Section 3.4.1.

Objects detected by MODEST that are found to be in the publicly-available SSN catalog, with available Two Line Elements (TLEs), are termed correlated targets (CTs). Detected objects not correlated to objects in the catalog, based on the missed distance (absolute value of the squared difference between the observed and the predicted right ascension [RA] and declination [DEC] positions), are termed uncorrelated targets (UCTs). The MODEST datasets provide the following information for each target (*i.e.,* each detection) in the dataset:

- Detection date
- Detection time referenced to Universal Time (UT)
- ID (SSN catalog number for CTs, “99999” or “UCT” for UCTs)
- Observed mean motion assuming circular orbit)
- Observed inclination (INC, degrees, assuming circular orbit)
- Observed Right Ascension of the Ascending Node (RAAN, degrees, assuming circular orbit)
- Absolute magnitude

- Predicted eccentricity (ecc, UCTs will be reported as 0 ecc, otherwise ecc is provided from TLEs for CTs)
- Expectation value (EV)
- Number of detections
- Size (d, m)

Magnitudes for each target are converted to size according to Equation 2.2-3, assuming an albedo of 0.175 (Mulrooney, Matney, & Barker, 2008), a diffuse Lambertian phase function, a range of 36,000 km for GEO observations, and with the Sun's apparent magnitude of $M_{sun}(R)$ = −27.103 when using the MODEST broad R filter. The MODEST system is capable of detecting 19th magnitude objects, which corresponds to approximately 10 cm in size under these assumptions for magnitude-to-size conversion; however, the dataset is considered complete to approximately 17th magnitude (approximately 30 cm in size). Each MODEST target has an associated EV which is defined as the likelihood of detection in a given orbit and is calculated based on the location of the telescope at a given date and time. Each MODEST 3-year dataset provides "complete" coverage over the entire 3-year timespan, so that the given expectation value is the likelihood of seeing a target over the entire 3-year interval. This expectation value is used to assign each target a weight, w, representing how many times that target should be counted for a statistical sampling of the population. The weight, or number of objects represented by each target in the MODEST dataset, is equal to the inverse of the EV, that is, w = 1/EV.

An object in the GEO belt that is expected (on average) to be detected multiple times over a set of observation runs would have an expectation value greater than one, and thus, a weight less than one. This statistically accounts for multiple detections of the same object. Likewise, an object with an orbit that has a low expectation value of being detected due to the observation times and pointing directions would have a weight greater than one, indicating that object is a sample from a larger population that is, on average, undetected or under-sampled. This weighting procedure applies to both UCTs and CTs. The expectation values, and thus the object weights, given in each MODEST dataset are determined based on the observation coverage of each observation campaign, so the weights applied to the targets in each dataset are independent.

The MODEST 2004–2006 and 2007–2009 datasets were combined into a composite dataset and propagated to a common epoch of 0h UT 1 January 2007, corresponding roughly to the midpoint of the two datasets. UCTs were filtered to include only those objects most likely to be GEO fragmentation debris, based on their magnitude (size) and a debris ring filter applied in the Cartesian coordinates of (INC · cos(RAAN), INC · sin(RAAN)). CTs identified as fragmentation debris were also included in the composite dataset. See Sections 3.3.2 and 3.3.3 of the ORDEM 3.1 Process Document for details of the process to combine and filter the datasets.

2.5.2 GEO Population Verification

2.5.2.1 Mean Motion Distribution

The orbital arc observed by MODEST is short, and an assumed circular orbit (ACO) is thus necessary to obtain the orbital elements for UCTs. Non-circular orbits were assigned to the UCTs using the behavior of the modeled GEO breakup clouds, as discussed in Section 3.3.4 of the ORDEM 3.1 Process Document. To verify that the model behaves correctly, within the limitations of the MODEST observations, a comparison of the modeled mean motions to the mean motions observed in the MODEST 2004–2009 composite dataset was performed.

Since the mean motion of the UCTs in the MODEST datasets are calculated using an ACO, to compare to the non-circular orbits assigned to build the ORDEM 3.1 populations, the orbits from the statistical ORDEM 3.1 GEO population (the GEO population based on the MODEST detections, without the LEGEND component) were converted to a circular mean motion distribution. That is, using an object's

modeled mean motion and eccentricity, 100 samples of an ACO mean motion were calculated assuming a true equatorial orbit and the circular velocity at that altitude. The estimated orbit for each object in the population was weighted by $w/100$, and the resulting circular mean motion distribution is shown in Figure 2-21, compared to the MODEST composite observed mean motion distribution. The number of objects in each bin is the sum of the weights of the objects in that bin, since each object does not necessarily have a weight equal to one. Uncertainties shown for the MODEST data points are the one σ-confidence intervals from the standard Poisson counting error:

$$\sigma = \sqrt{\sum_{i=1}^{M} w_i^2} \qquad 2.5\text{-}1$$

where M is the number of MODEST targets in the bin of interest, and w_i is the weight of an individual target. In general, the circular mean motion distribution of the ORDEM 3.1 population provides a match to the MODEST data within the one σ, and certainly two σ, uncertainty bounds. For mean motions below approximately 0.9 rev/day, where the model and the data diverge more prominently, it is possible that geosynchronous transfer orbit (GTO) objects are classified as GEO objects in the MODEST datasets, given the circular orbit assumption and the rate box used (±2 arc-second/second in hour angle and ±5 arc-second/second in declination (Abercromby, Seitzer, *et al.*, 2010; Abercromby, Seitzer, *et al.*, 2011), even with the debris ring filter that was applied to select objects most likely to be GEO debris. This discrepancy is an area of ongoing investigation but given the large uncertainties on the MODEST data points, indicating low statistical sampling, the overall agreement between ORDEM 3.1 and the MODEST data is considered quite good.

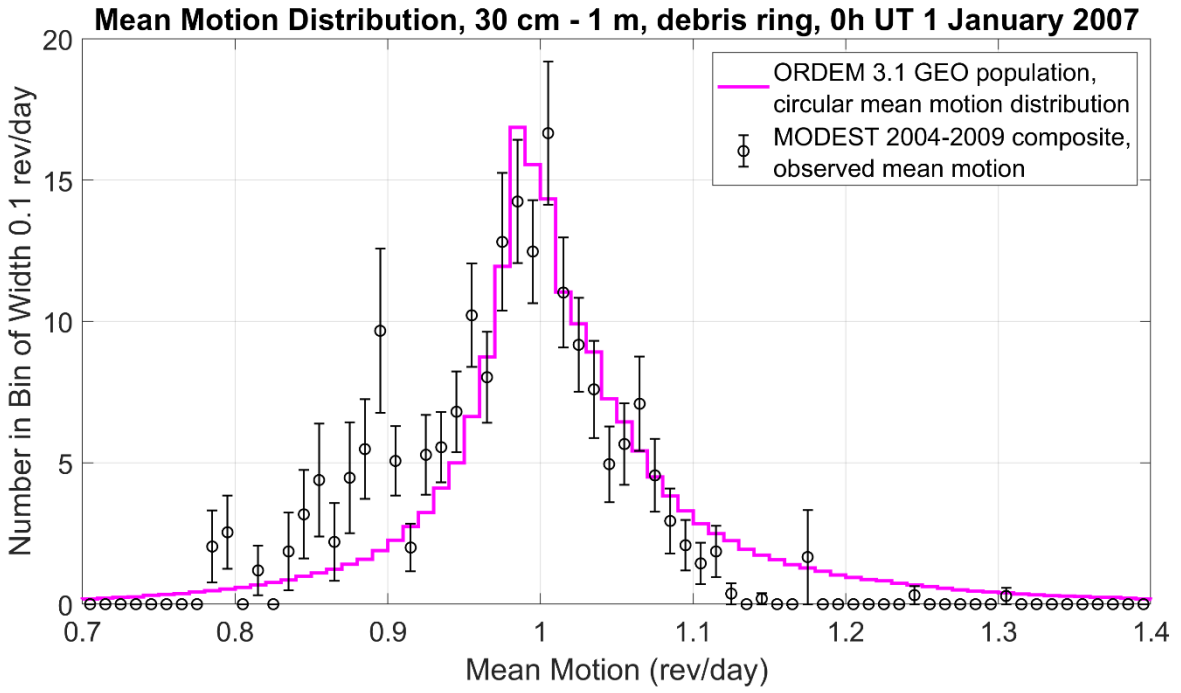

Figure 2-21. Comparison of the mean motion distribution from ORDEM 3.1, converted to a circular mean motion distribution, and the observed mean motion distribution from the MODEST 2004–2009 composite UCTs and CT debris.

2.5.2.2 *Cumulative Number vs Size*

The MODEST dataset is considered complete down to 30 cm, so the ORDEM 3.1 GEO population was extended down to 10 cm using the slope of the MODEST composite dataset, as discussed in Section 3.3.5 of the ORDEM 3.1 Process Document. Figure 2-22 shows the cumulative size distribution of the statistical ORDEM 3.1 GEO population as compared the MODEST 2004–2009 composite dataset. As expected, the model follows the data quite well since this part of the ORDEM 3.1 GEO population was built from the MODEST composite dataset. Additionally, though, this comparison verifies that the component of the model that was built by extrapolating down to 10 cm extends the trend of the MODEST data greater than 30 cm down to the lower sizes, as intended. This serves to qualitatively verify the size distribution of the model below the coverage limit of MODEST.

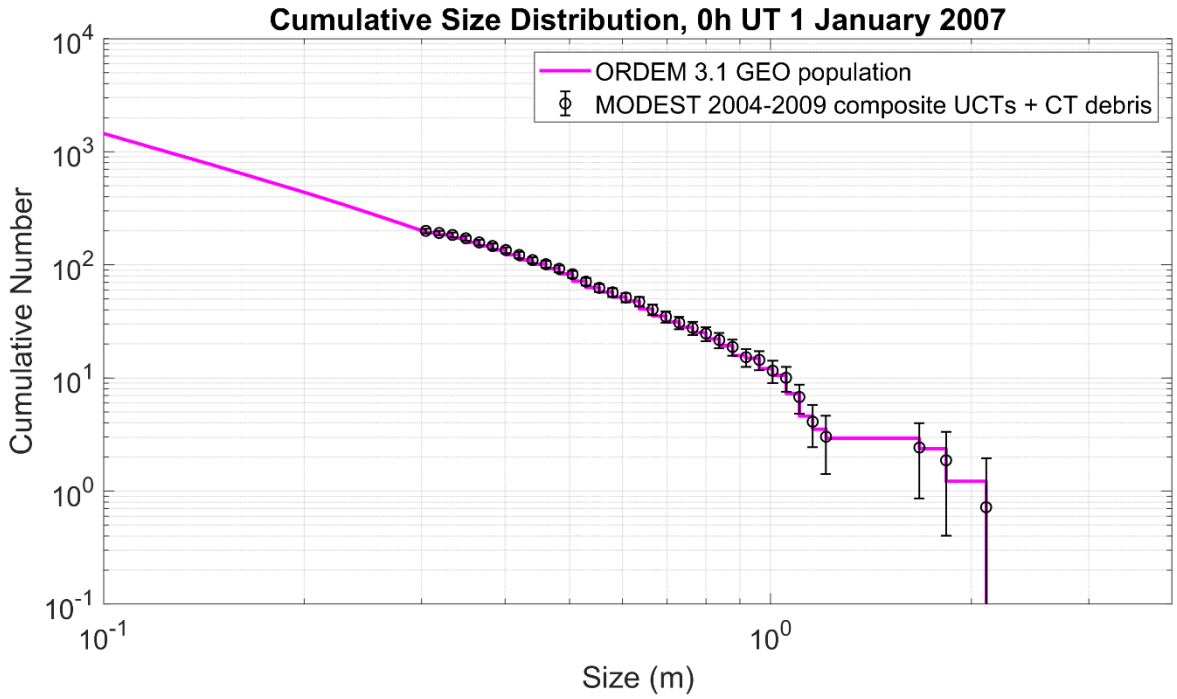

Figure 2-22. Comparison of cumulative number vs. size for the statistical ORDEM 3.1 GEO population and the MODEST 2004–2009 composite UCTs and CT debris.

3 VALIDATION

3.1 MODEL VALIDATION

Validation of the ORDEM 3.1 model is conducted using a similar methodology as that used for model verification – particularly with respect to the debris flux obtained from the model and that implied by each data source. An independent set of data sources, however, are used for the validation process to ensure that the ORDEM 3.1 model remains valid as additional observations from the orbital debris environment are made. These observations in some cases come from the same sensor, but typically for later years, to ensure that model predictions remain applicable in an evolving and dynamic orbital debris environment. In other cases, such as with additional data sources from HST and Goldstone, the data source provides a unique perspective on the environment that may extend the size of the orbital debris observation or contain additional information about a particular orbital regime than was available from the source(s) used for building the model.

3.2 RADAR-BASED POPULATIONS

3.2.1 HUSIR 2016 - 2017 Radar Data

HUSIR data from the 75E pointing geometry in 2016 and 2017 were used for ORDEM 3.1 validation. Many of the same considerations for the HUSIR 2013–2015 dataset used to build the ORDEM 3.1 populations are applicable to data from this sensor in 2016–2017. Variation in the performance of this sensor does arise, however, with one of the more important considerations being the sensitivity of the sensor changing over time due largely to changes in the transmitter power. HUSIR is a high power radar that uses traveling wave tube amplifiers (TWTAs) to obtain the transmitter power levels necessary to be sensitive to orbital debris at the altitude limits that this radar is intended to cover. TWTAs, however, are not as reliable as their solid-state equivalents, and the latter technology is not yet available for radars of this class. As a result, the year-over-year performance of the radar can vary significantly as TWTAs fail and are replaced. In Figure 3-1, the sensitivity of HUSIR over all of the years covered by the ORDEM 3.1 population build and validation datasets included in this report are shown. Note that in FY2017, the sensitivity of the radar falls off significantly, which implies that the limiting debris size that the radar is able to see for this fiscal year is not as small as in other years. FY2016, however, was a good year for the radar from the sensitivity point of view, and it is sensitive to orbital debris down to similar sizes as that observed in the 2013–2015 dataset.

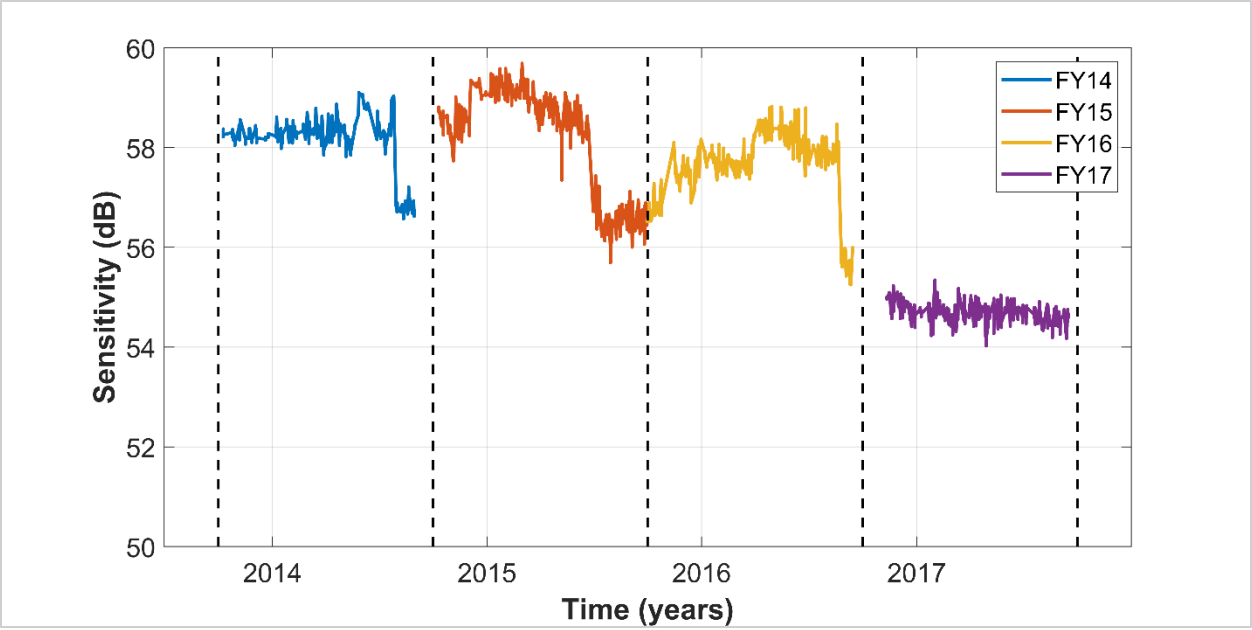

Figure 3-1. Sensitivity history for HUSIR from the beginning of FY2014 through the end of FY2017. The vertical dashed lines indicate fiscal year boundaries.

3.2.2 Goldstone 2016–2017 Radar Data

Additional radar datasets available for validation of ORDEM 3.1 are from the Goldstone Solar System Radar, a bi-static radar that uses a 70 m antenna with a nominal 440 kW to transmit and a 35 m receiver antenna to receive radar returns from orbital debris. Goldstone, like HUSIR, uses tube-based amplifiers – klystrons – for its transmitter and is subject to similar sensitivity variations for orbital debris data collection activities. Goldstone is unique in that it enables debris observations to even smaller sizes than HUSIR, down to approximately 3 mm at 1000 km altitude; however, its performance is limited for larger orbital debris sizes. For objects on the order of 1 cm and above, the larger radar returns tend to saturate the low noise amplifier, particularly for smaller slant ranges, which reduces the count rate for objects at these sizes. HUSIR has a more sophisticated auto gain control system, enabling it to avoid saturation on similarly sized debris objects.

The Goldstone radar data were upgraded in 2016–2017, where both a PP and OP channel were available to make use of the NASA SEM for estimating debris size from the RCS reported in radar data observations. Significantly fewer observation hours are available from Goldstone than HUSIR, and higher orbital debris density altitude regions provide better counting statistics for the limited number of hours received. Thus, comparisons to Goldstone data are made mostly at higher altitudes where the counting statistics are improved.

3.2.3 Surface Area Flux vs Altitude

The more recent 2016–2017 HUSIR and Goldstone datasets were used as validation, and comparison of these data are made to the ORDEM 3.1 model predictions. Since the model was not built from these datasets, this is a good indicator of how well the model is doing at providing predictions of the debris environment from more recently collected and processed data.

A similar methodology to that used for model verification was applied for the comparison between model and validation measurements. In this section, the surface area fluxes versus altitude are compared. In Figure 3-2, the surface area flux for HUSIR in 2016 is compared to the model to a limiting size of 1 cm and larger. The surface area flux is again the number of debris objects that pass through the surface area of the radar beam – restricted to the two-sided 3-dB beamwidth for each radar, per unit time – which is on a yearly basis. Uncertainties on the data points are the one σ Poisson uncertainties described in Section 2.2.4. As shown in Figure 3-2, ORDEM 3.1 continues to provide a good model fit for the environment in 2016 and is a better fit than ORDEM 3.0.

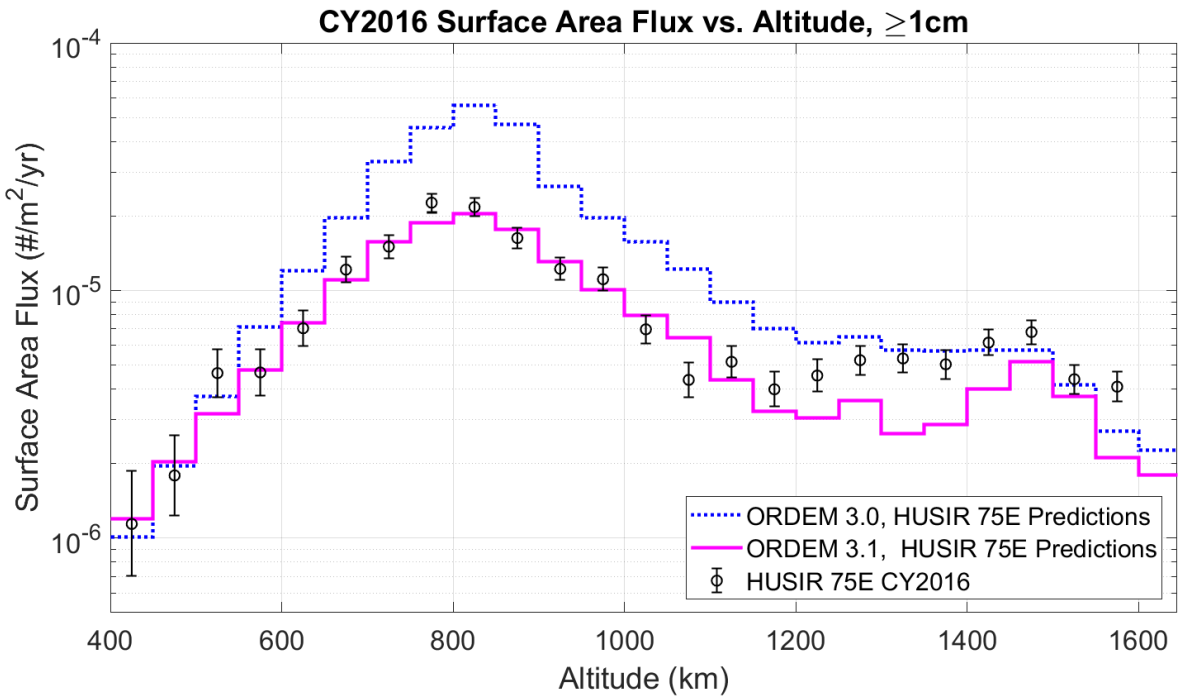

Figure 3-2. Comparison of the surface area flux vs altitude for a limiting size of 1 cm and larger between ORDEM 3.0, ORDEM 3.1, and measurements from HUSIR 75E in 2016.

As described in Section 3.2.1, HUSIR had comparable sensitivity in 2016 as it did in 2013–2015, where the radar is sensitive to orbital debris down to 5.5 mm at 1000 km. This limiting size and larger are used to develop the surface area flux versus altitude plot shown in Figure 3-3 (as in Figure 2-10, shown for the model reference size of 5.5 mm and larger). The ORDEM 3.1 model prediction is again observed to match the data well for most of the altitude bins shown and is a better match than ORDEM 3.0. The deviations observed at 700–850 km, where ORDEM 3.1 is under-predicting the environment in 2016 are hypothesized to be the result of several breakups that occurred near these altitudes in 2015. These breakups were not included in the ORDEM 3.1 population builds, and additional investigation is needed to determine whether these breakups in 2015 are the source of this deviation. As will be observed in Figure 3-5, however, deviations during 2017 are smaller at these altitudes; thus, if the discrepancy in 2016 is due to these breakups, as hypothesized, most of the additional debris created by these events washed out of the environment by 2017.

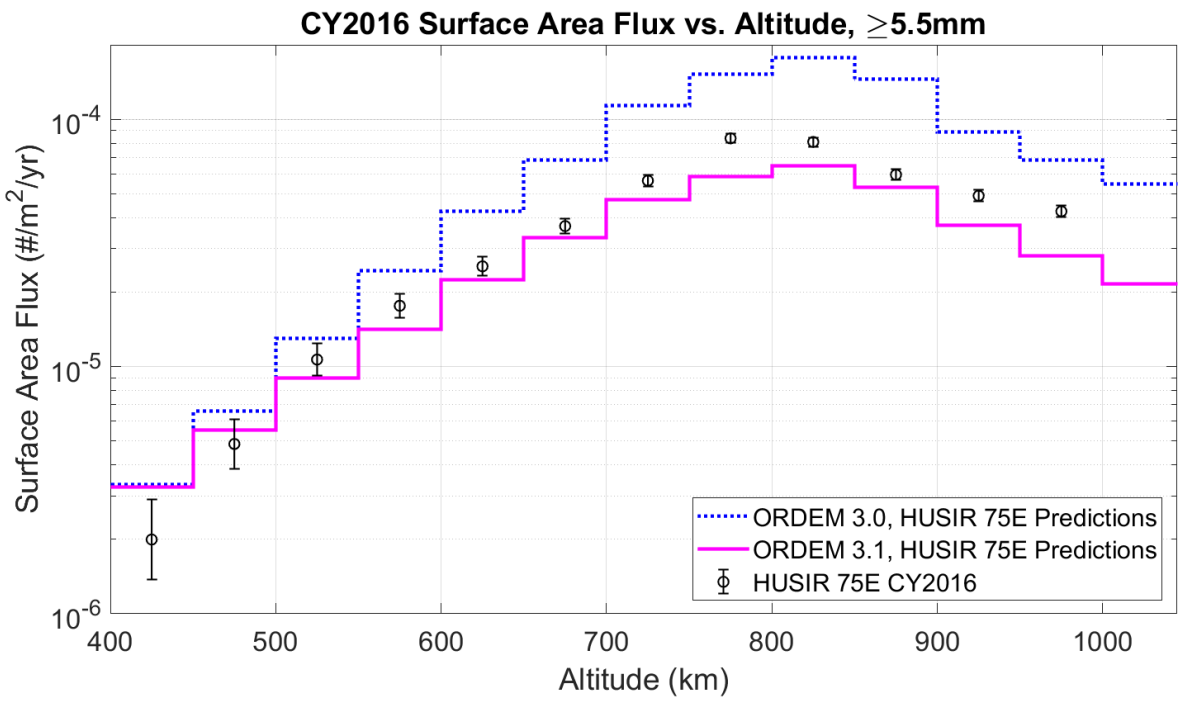

Figure 3-3. Comparison of the surface area flux vs altitude for a limiting size of 5.5 mm and larger between ORDEM 3.0, ORDEM 3.1, and measurements from HUSIR 75E in 2016.

Surface area flux versus altitude is compared between ORDEM 3.1 and HUSIR measurements for 2017 in Figure 3-4 and Figure 3-5 to a limiting size of 1 cm and 5.5 mm, respectively. Recall that in 2017, HUSIR was less sensitive than in other years considered in this report, and the altitude limit for a sensitivity to the 1 cm size drops from 1600 km to approximately 1500 km, while the limit for 5.5 mm drops from 1000 km to approximately 900 km. Data from this sensor in 2017, however, continues to show that for altitudes where the radar is sensitive, the data continue to match ORDEM 3.1 well, and ORDEM 3.1 provides a better match to the environment than ORDEM 3.0.

An additional point of interest in Figure 3-4 and Figure 3-5 is that the radar saw fewer objects in 2017 at the 400–450 km altitude bin than predicted, whereas in 2016 the radar data and model predictions were statistically equivalent for objects 1 cm and larger. Additionally, ORDEM 3.1 is better matched to the data in the 700–850 km altitude region, where a more significant under-prediction was seen during 2016 for the 5.5 mm and larger orbital debris (Figure 3-3).

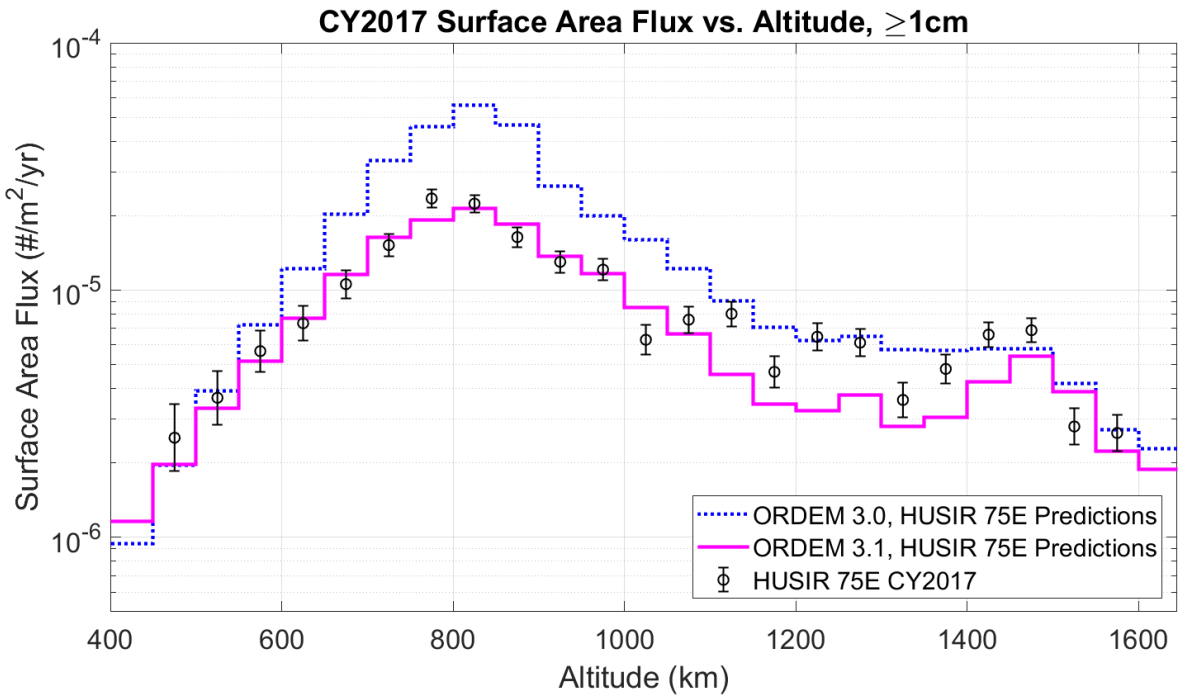

Figure 3-4. Comparison of the surface area flux vs altitude for a limiting size of 1 cm and larger between ORDEM 3.0, ORDEM 3.1, and measurements from HUSIR 75E in 2017.

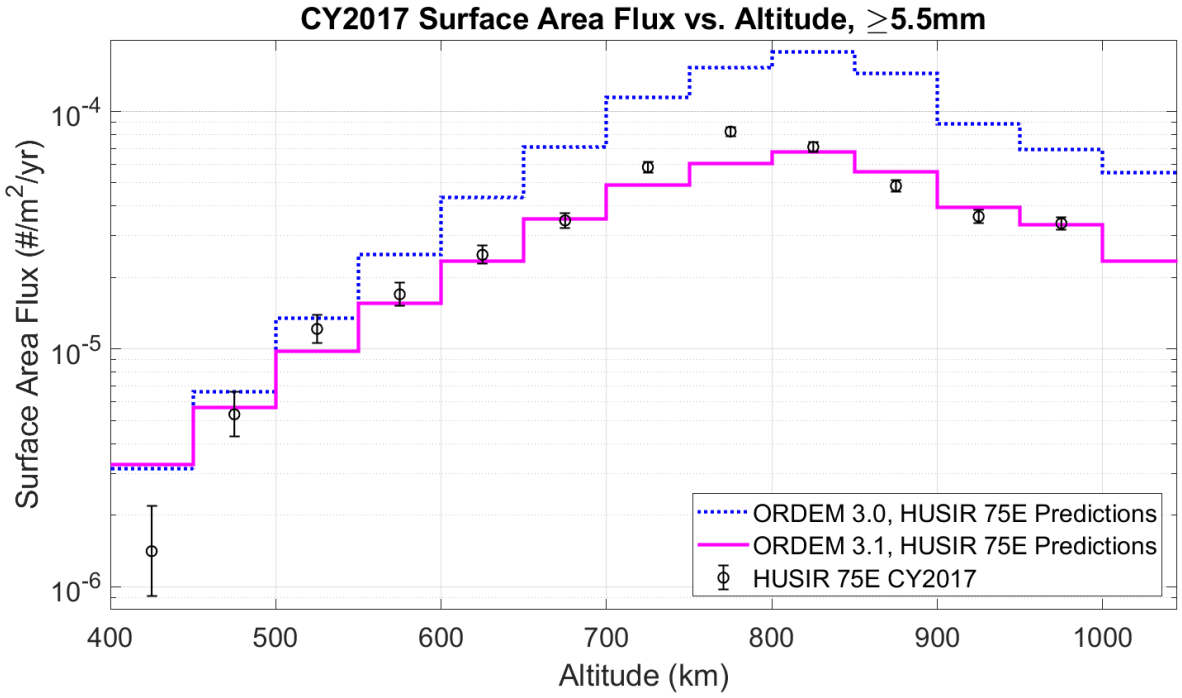

Figure 3-5. Comparison of the surface area flux vs altitude for a limiting size of 5.5 mm and larger between ORDEM 3.0, ORDEM 3.1, and measurements from HUSIR 75E in 2017.

3.2.4 Surface Area Flux vs Size

As an additional check of the model, the surface area flux as a function of SEM size are compared in this section. In Figure 3-6, the HUSIR surface area flux versus size in 2016 from 400 to 1000 km is compared to the model. As observed for the similar plot in Section 2.3.3 (Figure 2-11), the roll-off in the data indicates where the loss of radar sensitivity occurs – around 5.5 mm. The ORDEM 3.1 model matches the data well and is a better match than ORDEM 3.0.

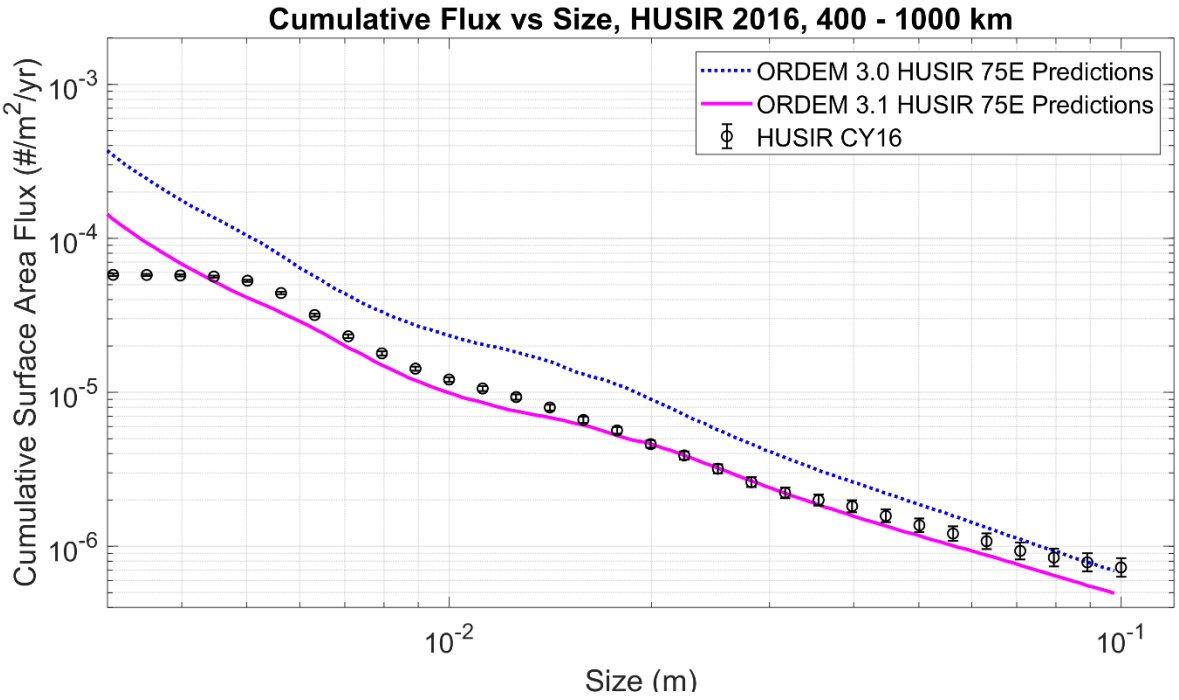

Figure 3-6. Comparison of the surface area flux vs SEM size between ORDEM 3.0, ORDEM 3.1, and measurements from HUSIR 75E in 2016. The altitude is restricted to 400–1000 km.

A similar comparison was made to the Goldstone data, as shown in Figure 3-7. Goldstone is more sensitive to the smaller debris particles than HUSIR, and the data is well matched to the model prediction out to approximately 4 mm. The match between data and ORDEM 3.1 predictions is significantly better than that for ORDEM 3.0. The horizontal axis is shown going out to only 1 cm because of the well-known saturation issue that this radar has for larger objects – in fact, the roll-off starts for sizes slightly smaller than 1 cm in Figure 3-7.

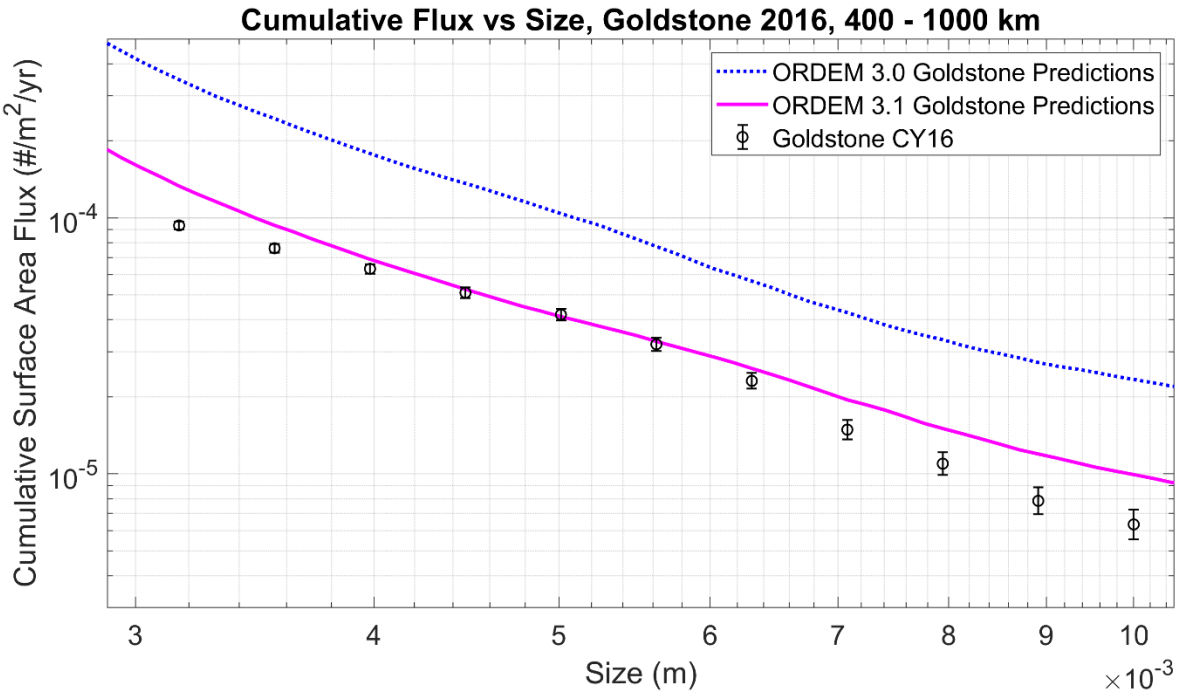

Figure 3-7. Comparison of the surface area flux vs SEM size between ORDEM 3.0, ORDEM 3.1, and measurements from Goldstone in 2016. The altitude is restricted to 400–1000 km.

Additional validation is conducted for several key altitude bands in the remaining figures in this section. In Figure 3-8, HUSIR 75E 2016 data is compared against ORDEM 3.1 and 3.0 model predications in the 400–450 km altitude regime (nominal ISS orbit altitude). Note that both model predictions are relatively close to each other, but the ORDEM 3.1 model follows the step up in cumulative surface area flux slightly better than ORDEM 3.0 for sizes around 8 mm and larger, and follows the data better at sizes below approximately 5 mm.

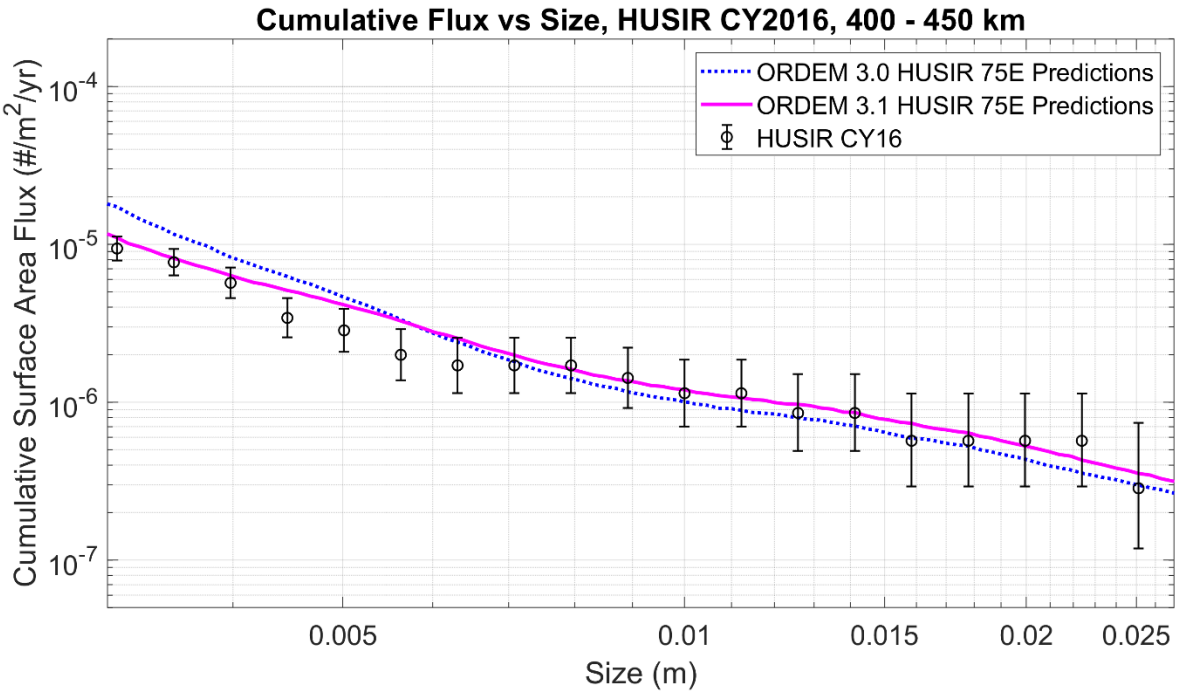

Figure 3-8. Comparison of the surface area flux vs SEM size between ORDEM 3.0, ORDEM 3.1, and measurements from HUSIR 75E in 2016. The altitude is restricted to 400–450 km.

Predictions for the 700–750 km altitude band, of interest to the A-Train Constellation, are compared to HUSIR data from 2016 in Figure 3-9. The data from HUSIR indicates a good match to ORDEM 3.1, which is better matched to the data than ORDEM 3.0. Model predictions are compared to Goldstone data from 2016 in Figure 3-10. This comparison also shows a good match, where the left endpoint for the data used in Figure 3-10 is close to 3 mm. The upper size cut-off in this figure is near 1 cm due to the receiver amplifier saturation.

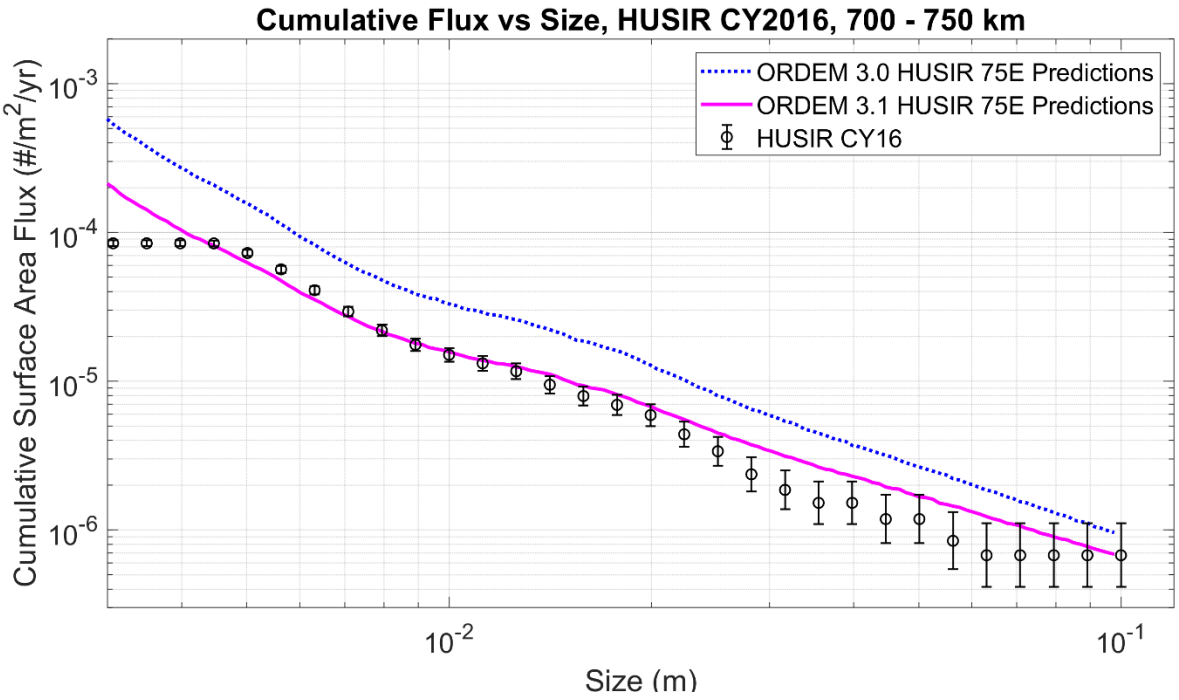

Figure 3-9.Comparison of the surface area flux vs SEM size between ORDEM 3.0, ORDEM 3.1, and measurements from HUSIR 75E in 2016. The altitude is restricted to 700–750 km.

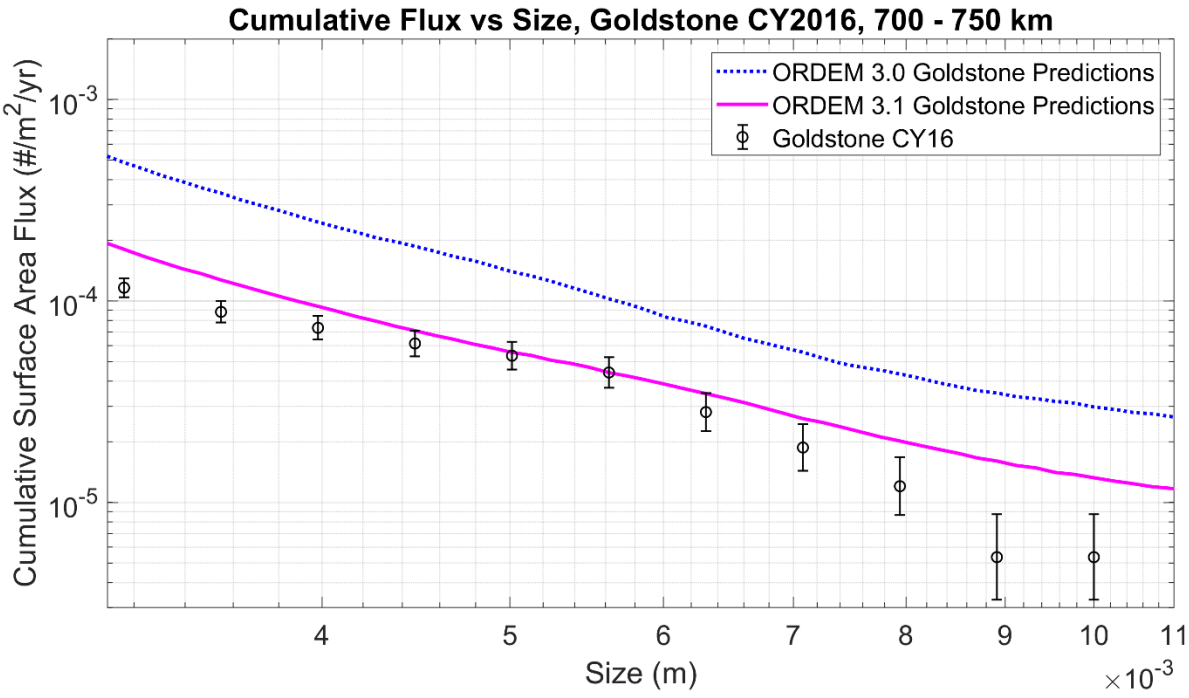

Figure 3-10. Comparison of the surface area flux vs SEM size between ORDEM 3.0, ORDEM 3.1, and measurements from Goldstone in 2016. The altitude is restricted to 700–750 km.

Moving up to 800–850 km (NOAA 20 operational altitude region), where the orbital debris density is significantly higher, model predictions for ORDEM 3.1 match the data much better than ORDEM 3.0 predictions, as shown in Figure 3-11. The completeness with respect to size for HUSIR is closer to 5 mm at this altitude, as observed in the roll-off in the data on the left-side of the figure. The one σ uncertainties are plotted along with the data, and the ORDEM 3.1 model is generally statistically equivalent to the data for many of the sizes shown. A similar plot from Goldstone in 2016 is available in Figure 3-12, where the ORDEM 3.1 model predictions again show good agreement with the data – with the left endpoint extending to nearly 3 mm.

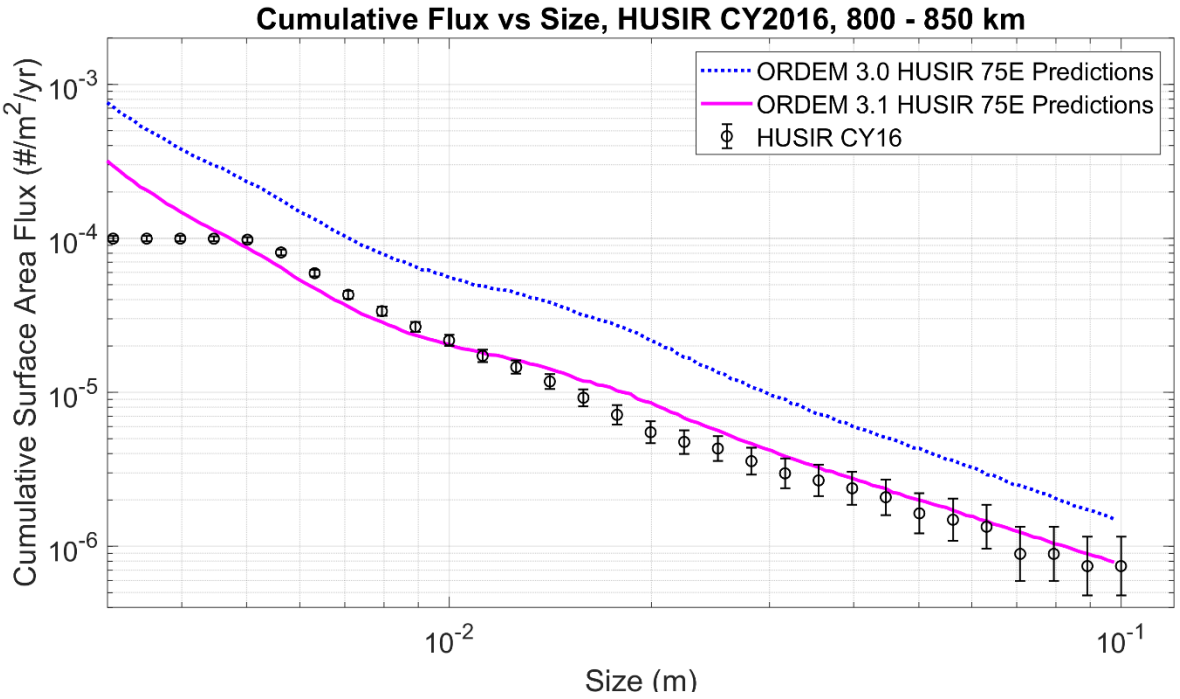

Figure 3-11. Comparison of the surface area flux vs SEM size between ORDEM 3.0, ORDEM 3.1, and measurements from HUSIR 75E in 2016. The altitude is restricted to 800–850 km.

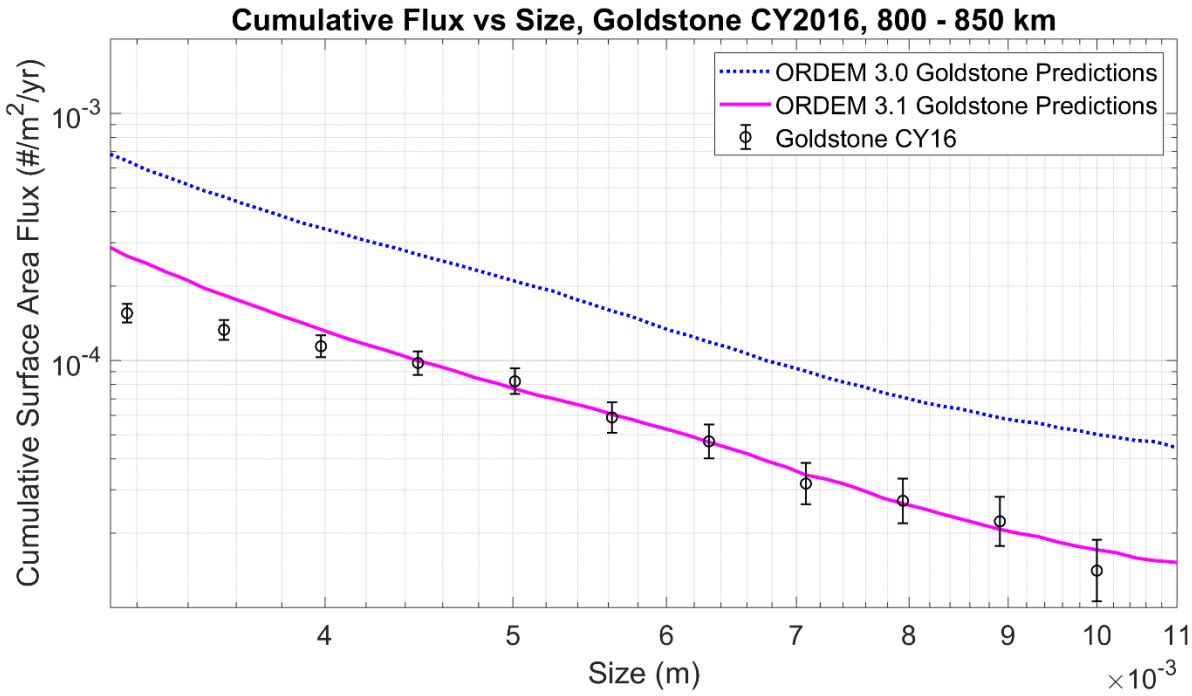

Figure 3-12. Comparison of the surface area flux vs SEM size between ORDEM 3.0, ORDEM 3.1, and measurements from Goldstone in 2016. The altitude is restricted to 800–850 km.

3.2.5 Log-likelihood Test

In addition to the graphical validation procedures discussed in the previous two sections, a modified log-likelihood test is described in this section to quantify the comparison of ORDEM 3.1 model predictions against radar data. The approach described in this section outlines a hierarchical model that enables model uncertainties to be directly included in the comparisons between the model and measured data. A Monte Carlo approach is used to generate a large number of samples from the hierarchical model, which are then compared against the data – resulting in p-values used to assess the likelihood that the measured data matches the model. The criteria used to indicate the quality of the model fit in this report are p-values tested at the 0.05 level of significance ($\alpha = 0.05$).

Monte Carlo samples, m_i, are drawn from a Poisson distribution as shown in Equation 3.2-4. The Poisson distribution is parameterized by λ_i, which is the expected value of orbital debris counts in a particular size or altitude bin. The context of λ_i depends upon the comparison being made, *e.g.*, the model results plotted in Figure 2-10 have the context of the expected number of objects in an altitude bin, whereas in Figure 2-11, it is the expected number of counts of a given SEM size or larger. While cumulative size charts are very useful, for the purposes of the statistical tests, the data was broken into differential size bins for comparison to the model.

Uncertainties are included by modeling each λ_i as being sampled from the log-normal distribution shown in Equation 3.2-3 – where in all cases in this section, "ln" refers to the natural logarithm. The population mean of the log-normal distribution to be sampled is assumed to be

$$\mu_i = ln\left[\frac{{y_i}^2}{\sqrt{{y_i}^2 + {\sigma_{yi}}^2}}\right] \qquad 3.2\text{-}1$$

where y_i is the ORDEM 3.1 expected count (flux * area * time) in a given size or altitude bin and σ_{yi} is the uncertainty in the predicted model value of y_i computed by ORDEM 3.1. Similarly, the standard deviation of the log-normal distribution to be sampled is

$$\sigma_i = \sqrt{ln\left[1 + \frac{{\sigma_{yi}}^2}{{y_i}^2}\right]} \quad \text{3.2-2}$$

The sampling is a two-step process. First, we sample $\ln(\lambda_i)$ from the log-normal distribution

$$\ln(\lambda_i) \mid \mu_i, \sigma_i \sim N(\mu_i, \sigma_i) \quad \text{3.2-3}$$

We then sample from the Poisson distribution using the sampled λ_i as the expectation value.

$$m_i \mid \lambda_i \sim Poisson(\lambda_i) \quad \text{3.2-4}$$

The likelihood, *L*, that an array of data values (either actual data or samples from the Monte Carlo sampling procedure described above) are from Poisson distributions of the original array of expected values, y_i, is described in Equation 3.2-5. The log-likelihood, $\mathcal{L}$, (Equation 3.2-6) is constructed by taking the logarithm of the likelihood in Equation 3.2-5. To compare the log-likelihoods between the model and the measurements, the inequality in Equation 3.2-7 is evaluated for a set of Monte Carlo samples, where the i^{th} sample in a set represents the expected counts in the i^{th} size or altitude bin. Samples from the Monte Carlo model are m_i and the measured data values are x_i in Equation 3.2-7. If the sampled values are more likely than the measured data the inequality is false, while if the measured data is more likely the inequality is true. This process is conducted over many trials, and the proportion of times the Monte Carlo sample is less likely than the measurements determines the p-values for evaluating the model fit. This is shown graphically in Figure 3-13, where the ratio of the shaded area to the total area under the curve represents the p-value. The p-value can be compared to a target α value. So, assuming a 95% confidence value (α = 0.05), a p-value < α implies the inequality of Equation 3.2-7 is true < 5% of the time – indicating a poor model fit. Note that the log-likelihood is, by its nature, a one-sided / one-tailed test, so there is no indication of whether the data is above or below the model, only a measure of the likelihood the data is a random selection from the model.

$$L(\vec{m}|\vec{y}) = \prod_{i=1}^{n} Poisson(\mathrm{m}_i, y_i) = \prod_{i=1}^{n} \frac{{y_i}^{m_i} e^{-y_i}}{m_i!} \quad \text{3.2-5}$$

$$\mathcal{L}(\vec{m}|\vec{y}) = \log\left(L(\vec{m}|\vec{y})\right) = \sum_{i=1}^{n} m_i \log(y_i) - y_i - \log(m_i!) \quad \text{3.2-6}$$

$$\mathcal{L}(\vec{m}|\vec{y}) < \mathcal{L}(\vec{x}|\vec{y}) \quad \text{3.2-7}$$

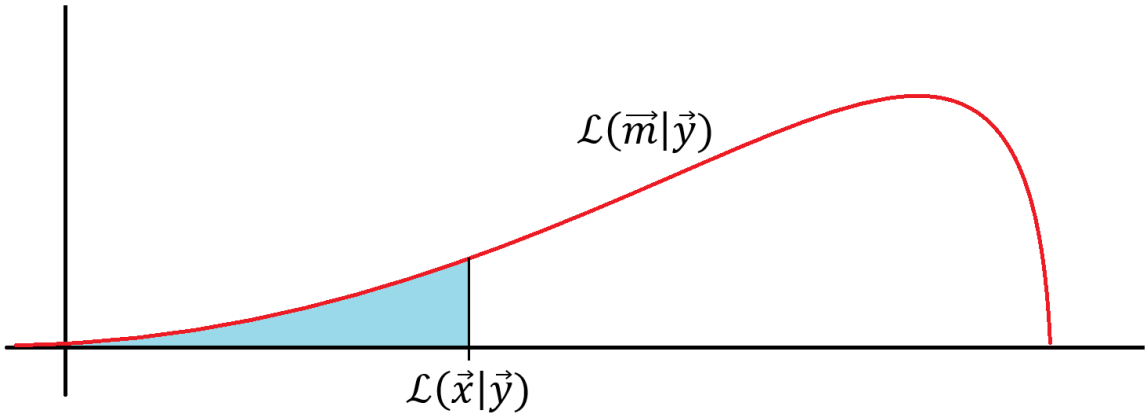

Figure 3-13. The curve represents the probability distribution of the Monte Carlo samples as described in the text. The shaded section represents Monte Carlo samples with log-likelihood lower than the original data. The ratio of the shaded area to the total area under the curve represents the p-value.

3.2.6 Log-likelihood Test for Radar Data

The log-likelihood test is applied to the radar data used to verify how well the ORDEM 3.1 model predictions match data not used in the construction of the model. The validation radar data are summarized graphically in Figure 3-2 to Figure 3-12, and in Figure B-3 (Appendix B). The results of the log-likelihood tests are shown in Table 3-1, where it is noted that all p-values obtained are greater than 0.05, indicating that the ORDEM 3.1 model predictions remain good compared against the validation datasets, using the criteria described in Section 3.2.5. Of the 12 cases tested, half were within a one σ confidence limit (α = 0.32) and half were within a 90% confidence limit (α = 0.1), which is very close to what would be expected by random chance.

Note that in the altitude bin cases, a minimum size had to be identified for which the detection rate was believed to be complete.

Table 3-1: Results from log-likelihood tests comparing ORDEM 3.1 model results against measured radar data used to validate the ORDEM 3.1 model.

Case	p-value	comments (within)
2016 HUSIR, 1 cm altitude breakdown, Figure 3-2	0.133	90%
2016 HUSIR, 5.5 mm altitude breakdown, Figure 3-3	0.119	90%
2017 HUSIR, 1 cm altitude breakdown, Figure 3-4	0.151	90%
2017 HUSIR, 5.5 mm altitude breakdown, Figure 3-5	0.390	1-sigma
2016 HUSIR, 400–1000 km (>1 cm), Figure 3-6	0.554	1-sigma
2016 HUSIR, 400–450 km (>3 mm), Figure 3-8	0.627	1-sigma
2016 HUSIR, 550–600 km (>5 mm), Figure B-3	0.237	90%
2016 HUSIR, 700–750 km (>5 mm), Figure 3-9	0.540	1-sigma
2016 HUSIR, 800–850 km (>1 cm), Figure 3-11	0.210	90%
2016 Goldstone, 400–1000 km (>4 mm), Figure 3-7	0.341	1-sigma
2016 Goldstone, 700–750 km (>3 mm), Figure 3-10	0.221	90%
2016 Goldstone, 800–850 km (>4 mm), Figure 3-12	0.361	1-sigma

3.3 IN SITU-BASED POPULATIONS

Since the release of ORDEM 3.0, significant work has been done in characterizing the impact record of the HST WFPC-2 and MLI blankets. These recent analyses, including the development of new analytical techniques, provides new validation data for ORDEM 3.1.

3.3.1 In situ Impact Data

3.3.1.1 HST MLI

The majority of the HST vehicle's external surfaces, including the bus and optical tube, are covered with thermal tape or MLI blankets. Servicing missions (SM) 1, 2, 3a, 3b, and 4 to the HST by the STS conducted extra vehicular human inspections, as well as photographic inspections of the HST exterior, from the vantage point of the orbiter vehicle's cabin, for the purposes of assessing space environment weathering and spacecraft health. In particular, damage to the MLI blankets was assessed and repairs and replacements conducted in the course of extra vehicular activities. Figure 3-14 depicts the HST exterior with prominent damage and replacements mapped following SM 3b.

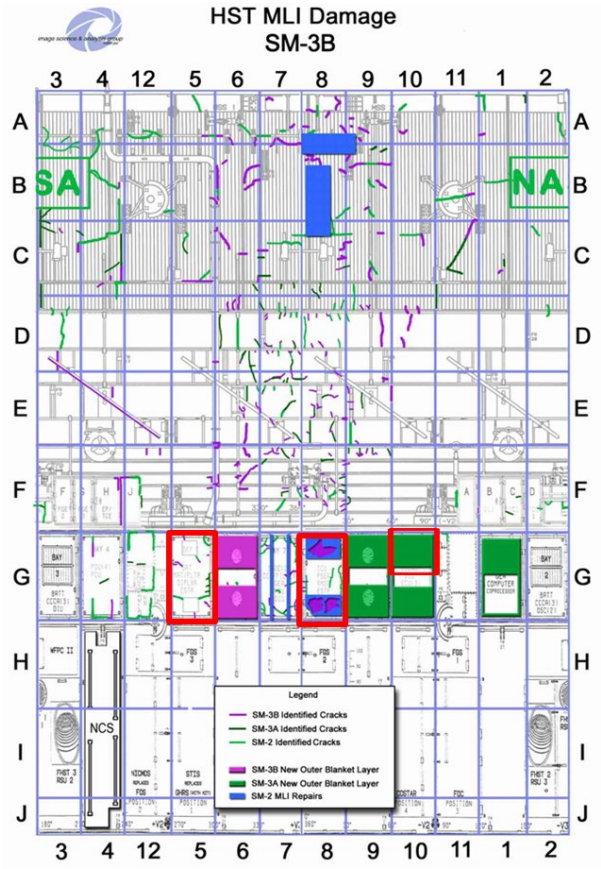

Figure 3-14. The HST surface "unrolled" to produce a flat map in spacecraft bay (horizontal) and longitudinal (vertical) coordinate space. Legend per original figure and uneditable to improve legibility. Red boxes indicate MLI panels briefly surveyed at NASA Goddard Space Flight Center (GSFC) in 2009 and delivered to, or intended for, NASA Johnson Space Center (JSC) for detailed survey; 5G is Bay 5, 8G is Bay 8, and 10G is Bay 10—note that only the upper half of Bay 10 was intended for ODPO analysis, the lower half being retained by the GSFC Public Affairs Office archive. The WFPC-2 radiator lies in the 2H-3H boundary in this figure.

MLI blankets for electronics bays 5, 8, and 10 (regions 5G, 8G, and 10G, respectively, in Figure 3-14) were retrieved by SM 4/STS-125 in 2009 and returned. Bays 5 and 8 had been exposed to the space environment for approximately 19.1 years, whereas Bay 10 had been exposed for 9.8 years. After examination by other project teams, the Bay 5 and 8 blankets were delivered to the ODPO for detailed inspection. Both blankets consisted of a complete 17-layer MLI stack consisting of two 5 mil- (127 μm)-thick vapor-deposited-Al (VDA)-Teflon™ fluoropolymer film (manufactured by Chemours) flexible optical solar reflector (FOSR) outer layers and 15 0.3 mil (7.62 μm) VDA-Kapton® polyimide film (manufactured by E.I. du Pont de Nemours and Co.) inner layers; the utility of Bay 8 was lessened by another project team's removal of the majority of the outer, exposed blanket layer. Thus, all recent analysis facilitating ORDEM 3.1 validation has concentrated on Bay 5. Four 20 x 20 cm samples were cut from Bay 5 and examined in detail. The nominal limiting feature size was 100 μm; however, the survey was extended to smaller sizes to encompass all features revealed by backlighting. Figure 3-15 depicts a typical penetration feature under both front-lit and backlight conditions.

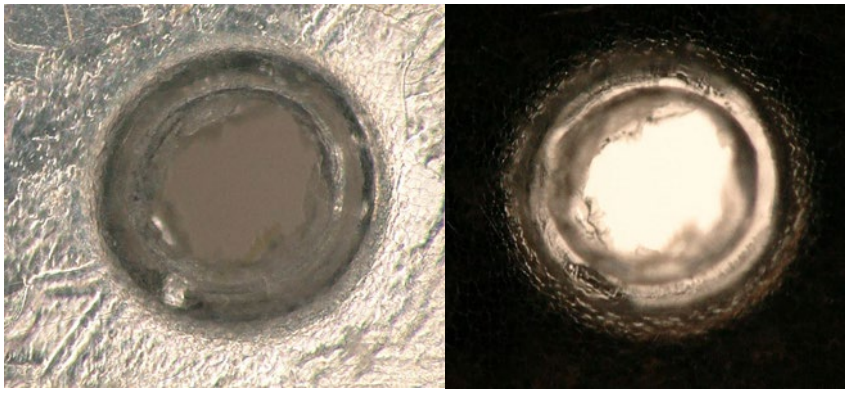

Figure 3-15. An HST MLI penetration (200x magnification). The same feature is illustrated in front-lit (left) and backlight (right) conditions.

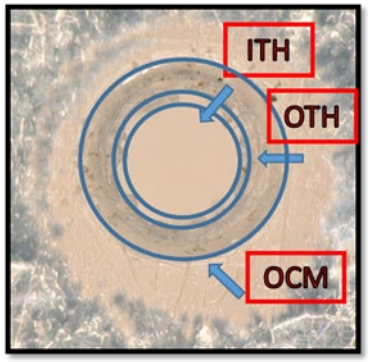

Figure 3-16. Morphological feature nomenclature developed during the analysis of MLI penetration features, shown at 200x magnification. These include inner through-hole (ITH), outer through-hole (OTH), and outer coating melt (OCM) measurements and diameters. For elliptical features, the minor axis was chosen to indicate diameter, attributing elongation of the major axis as being due to impact angle effects.

Blanket penetrations were characterized by their morphology (Figure 3-16) to include inner through-hole (ITH) and outer through-hole (OTH) diameter measurements (when elliptical, the penetration's minimum [or minor] diameter was used), an opaque zone diameter, a (backlight) transmission zone diameter, and an outer coating melt (OCM) damage zone diameter. A NASA White Sands Test Facility (WSTF) test

campaign was used to calibrate penetrations and develop a damage equation, as well as to explore the potential for MLI impacts to be below the hypervelocity impact (HVI) threshold and thus more likely due to contamination than on-orbit MM/OD impacts. Figure 3-17 compares the inner and outer through-hole diameters from the Bay 5 MLI with WSTF impacts.

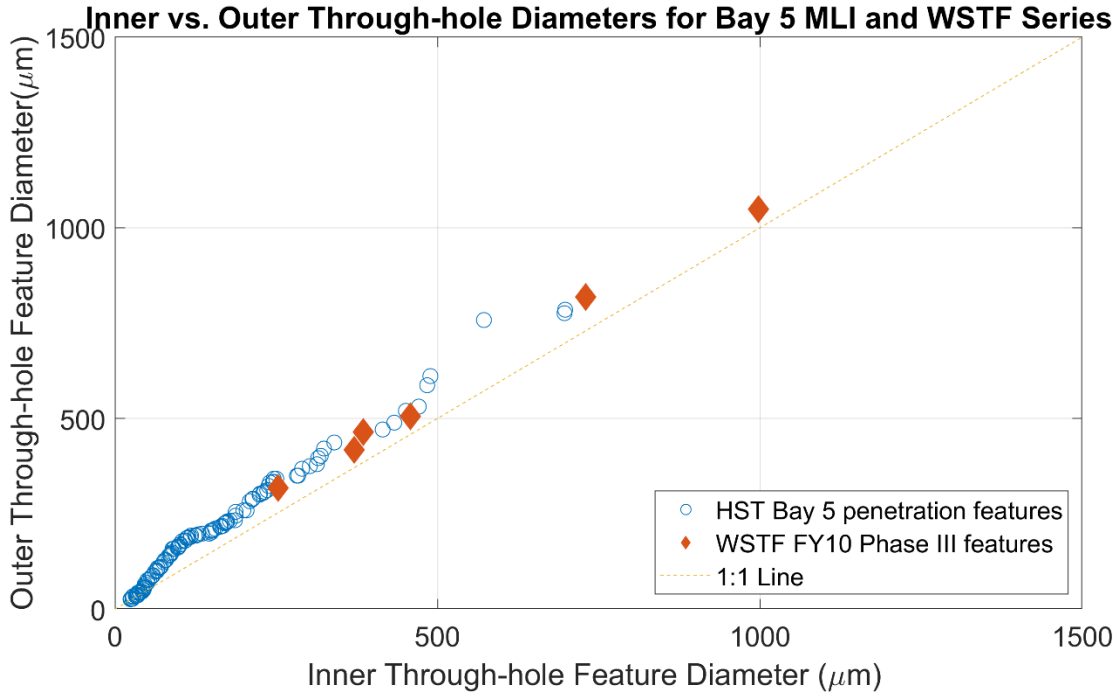

Figure 3-17. HST Bay 5 MLI penetration's inner and outer through-hole feature sizes compared with features observed in a NASA WSTF test campaign. Materials used in WSTF campaigns included soda lime glass, Nickel, and Al 2017-T4 alloy.

Bay 5 penetration measurements and ground-based WSTF testing are consistent. Additionally, this comparison confirmed that the nature of MLI impacts (featuring both inner and outer through-holes rather than a clean "cookie cutter" appearance) was consistent with HVI morphology. Penetration measurements were further compared with WSTF HVI test data to derive an appropriate, interpretive damage equation. The generic form relating d_c, the feature diameter [mm], and d_p, the projectile diameter [mm], was expressed as:

$$d_c = c \cdot d_p^{\alpha} \cdot \rho_p^{\beta} \cdot (v \cdot cos\theta)^{\gamma} \qquad 3.4\text{-}1$$

where all other variables are as defined in Section 2.2.2. The inner and outer through-holes and the outer melt zone diameters were compared, using linear least-squares analysis, to the WSTF HVI data, and the OTH measurements were determined to yield the minimum residuals with respect to these data. Therefore, the OTH measurements were adopted for the feature size determination and the ensemble (c, α, β, γ) of constants (0.99133, 0.866, 0.2928, 0.1958) used when the equation was inverted to solve for d_p. SEM-EDX analysis of the MLI blanket penetrations has not yet been conducted to characterize trace residues and provide information on impactor type (MM or OD) or material density. Thus, for the purposes of ORDEM 3.1 validation, the reader must note that (a) mean mass densities of 7.9 g/cm^3 (HD) and 2.8 g/cm^3 (MD) were adopted for interpreting d_p from d_c, and (b) MM and OD impacts cannot be differentiated, so validation is conducted against the total (MM and OD) model environments.

Figure 3-18 illustrates the cumulative number distribution, scaled per square meter, derived from measurements of the HST Bay 5 MLI blanket for all impact features as well as only impacts which penetrated the first layer.

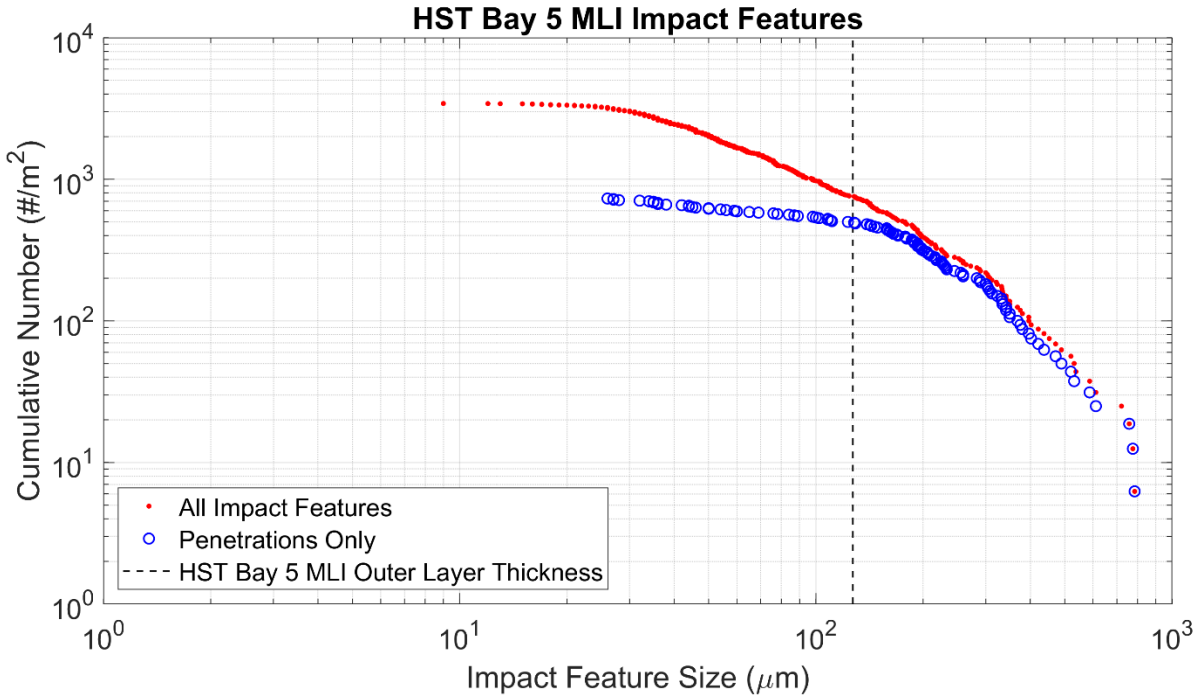

Figure 3-18. Feature sizes measured from four HST Bay 5 MLI 20 x 20 cm square samples. The outer (exposed) layer thickness is indicated relative to feature sizes to provide a measure for the transition from craters to penetrations which is typically difficult to interpret. Impact feature size is used as the independent variable because an MLI cratering damage equation does not exist at the time of writing.

The interpretive damage equation 3.4-1 was used to derive projectile diameters for MLI penetrations under the assumptions outlined above. The resulting ensemble is portrayed in Figure 3-23.

3.3.1.2 HST WFPC-2

The HST WFPC-2 camera was retrieved by SM 4/STS-125 in 2009 and returned after approximately 15.4 years exposure. The camera's radiator consisted of a 0.8 m x 2.2 m curved rectangular plate conformal to the HST's outer surface and covering 60° in azimuthal extent. The 4.06 mm-thick Al 6061-T6 substrate was painted with a 4-6 mil (102-152 μm)-thick layer of Zinc Ortho-Titanate YB-71 white thermal paint. The NASA ODPO mounted three expeditions to NASA Goddard Space Flight Center (GSFC) in 2009 to characterize the surface of the WFPC-2's radiator. During these inspections, 677 impact features to a limiting feature size of 300 μm were observed and documented (Opiela, Liou, & Anz-Meador, 2010). After examination of the radiator by other project teams, the radiator was de-mated from the camera assembly and delivered to the ODPO for detailed inspection of MM/OD impact features. This inspection consisted of coring over 400 of the largest features and analyzing them for impactor residues using SEM-EDX and other techniques. Cores and typical analysis products are illustrated in Figure 3-19.

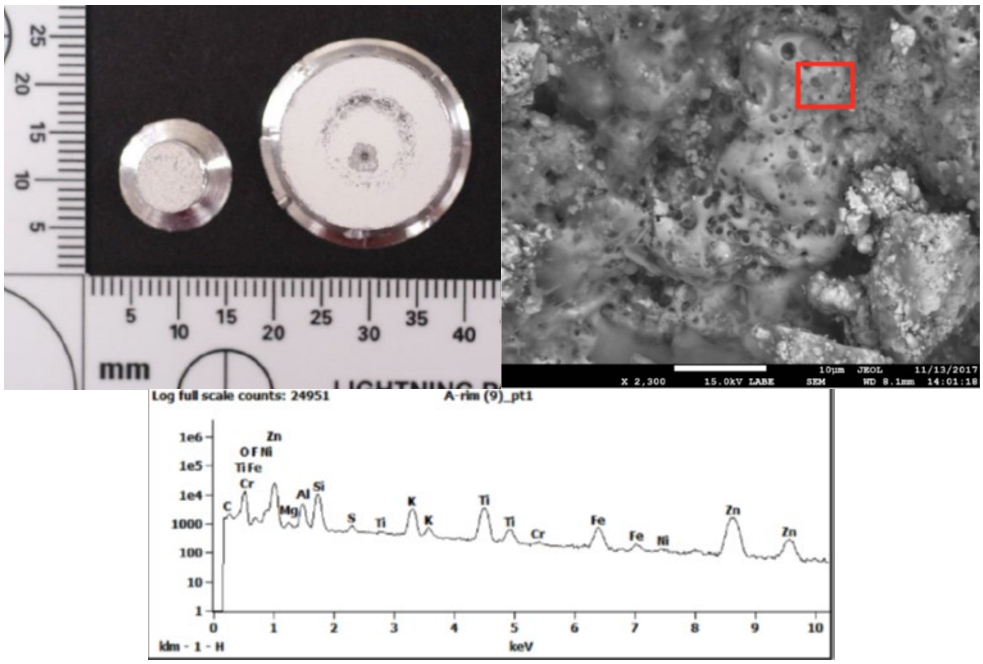

Figure 3-19. (upper left) small and large cores extracted by special machining from the HST WFPC-2 radiator assembly, (upper right) SEM imagery of impact melt inside an impact feature, the red box indicating a region of interest characterized using EDX, (bottom) SEM-EDX energy spectrum of the elemental constituents discerned with the region of interest.

The NASA ODPO and HVIT conducted multiple WSTF test campaigns in the FY2010–2012 time frame to characterize the response of painted surfaces (primary goal), thermal taped surfaces, and MLI (secondary goals) to HVI. These were necessitated by the lack of suitable damage equations for coated surfaces. Figure 3-20 illustrates an impact on a prepared impact coupon (test article).

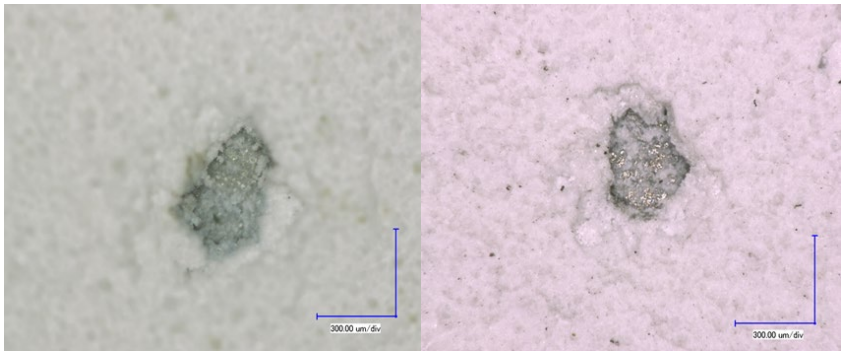

Figure 3-20. An impact feature observed on the WFPC-2 radiator (left) and on an impact coupon (right). In the latter case, the projectile was a 100 µm Al 2017-T4 sphere impacting the coupon at 5.32 km/s at an angle of 45°.

The NASA HVIT developed five interpretive damage equations for painted Al surfaces: these related impact parameters to crater depth, crater average and maximum diameters, and paint spallation zone average and maximum diameters. The “crater depth” equation was adopted for interpretation based on a better fit with respect to WSTF testing. The crater depth P [mm] as a function of projectile diameter d_p [mm] is defined as:

$$P = 0.238 \cdot d_p^{1.316} \cdot \rho^{1.111} \cdot v^{0.429} \cdot (cos\,\theta)^{0.751} \qquad 3.4\text{-}2$$

where all other variables are defined in Section 2.2.2.

The NASA ODPO commissioned a new study of crater residues for the largest WFPC-2 impact feature cores beginning in FY17 to facilitate ORDEM 3.1 validation. The cores were initially reexamined using typical SEM-EDX techniques. However, a new technique was developed over the course of this work, specifically to address difficulties in EDX sampling the small melt volumes present in the craters. This technique consists of potting the core in an epoxy resin; cutting the core and polishing the newly-exposed surface of the core, including a seam along the impact feature's long axis; and applying SEM-EDX and X-ray elemental mapping to the smooth surface. Figure 3-21 illustrates the new technique applied to a large WFPC-2 crater.

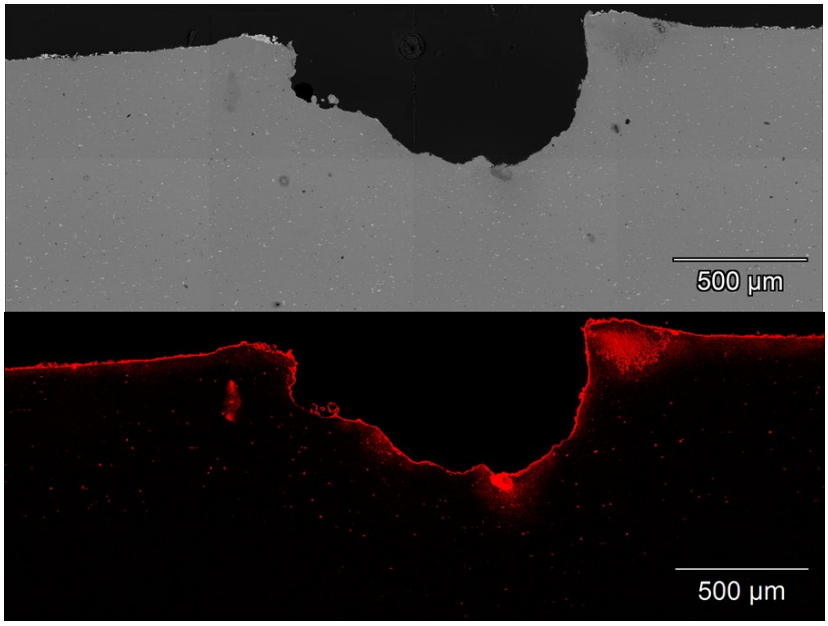

Figure 3-21. An SEM image of the lateral surface of the cut core (top) and an X-ray map of Potassium (as found in the YB-71 paint's binder) (bottom). This is core sample A, N1_21_16 or "Big 10" in the survey nomenclature of the 2009 inspection conducted at NASA GSFC, or JSC core number 471.

Damage equation density is determined by this new technique. In the case of the feature illustrated in Figure 3-21, the impactor is classified as likely stainless steel, an HD category impactor. Therefore, a mass density of 7.9 g/cm^3 was used when interpreting this feature. Relative velocity and impact angle factors were assessed in a probabilistic method using detailed HST pointing histories provided to the ODPO by the HST Program Office to generate estimates of the mean impactor diameter and attendant uncertainties, similar to the approach used for the STS impact data (Section 2.4.2).

The newly-developed analysis techniques described above are on-going as of this report's writing. Eleven large cores have been analyzed and attribution made to source (MM or OD) and likely impactor elements, compounds, or alloys through 23 May 2019. To that date, all impactors have been assessed as OD. Of these, four fall into the MD category with the remainder falling into the HD category.

The core sample ensemble facilitating ORDEM 3.1 validation is illustrated in Figure 3-22. The HVIT crater depth damage equation was used to interpret size, using either the MD or HD standard densities; in this

figure, size estimates are based upon the naïve assumption of a 10 km/s relative velocity and a 45° impact angle. Actual validation (Figure 3-23) uses a probabilistic sampling in relative velocity and impact angle based on sampling a detailed HST pointing history. Uncertainties (+/- one σ) are standard Poisson sampling uncertainties.

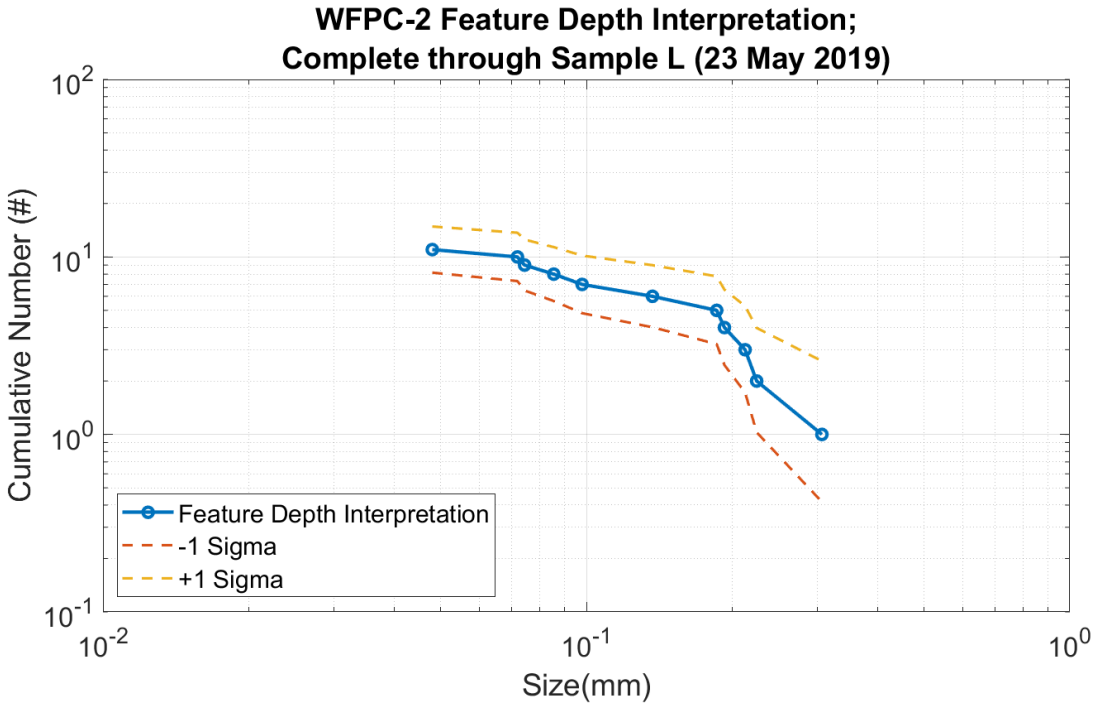

Figure 3-22. Cumulative distribution of WFPC-2 large impact features, using the crater depth damage equation, for 11 craters identified as OD or likely OD projectiles.

Conversion of the cumulative number distribution to the corresponding flux was predicated upon the radiator's area of 1.54 m^2 and exposure time of approximately 15.447 years. In addition, a scaling factor was applied to scale the total area appropriately based on the fraction of WFPC-2 sample craters whose analysis for MM/OD assessment is complete versus the census of craters to a limiting crater depth. The census is assumed complete with 122 features to a limiting crater depth of 200 μm. Two craters assessed as OD impactors featured anomalously small depths and were discarded so that, for a sample size of 11 (with 2 discarded), the scaling factor to extend the sample to the census was 122/9 or 13.56. This scaling factor reduces the applicable area to use for converting from surface area to cross-sectional area flux. It is incorporated into the fluxes shown in Figure 3-23 and will be updated regularly as additional WFPC-2 sample craters are assessed as having been caused by OD MD/HD projectiles.

3.3.2 Cumulative Flux vs Size

Figure 3-23 illustrates the agreement between a total MMOD environment model, under the necessary assumptions required, and data as described in Sections 3.3.1.1 and 3.3.1.2. The total MMOD environment is defined here as ORDEM 3.1 plus the meteoroid flux from the NASA Meteoroid Engineering Model Release 2.0 (MEM R2) (Moorhead, Koehler, & Cooke, 2015). Note that while the exposure time for the HST Bay 5 MLI and WFPC-2 radiator surfaces is different (19.1 years compared to 15.447 years, respectively), the resulting ORDEM fluxes considering those different exposure times is not significantly different; thus, for clarity, single curves are shown for ORDEM 3.0 and ORDEM 3.1 average fluxes covering the 19.1 years exposure time for the HST Bay 5 MLI. Two sets of Bay 5 MLI results are shown, corresponding to an assumption of all MD (2.8 g/cm^3) or all HD (7.9 g/cm^3) projectiles.

Comparison between the data and the model predictions is considered excellent for both the HST MLI penetrating flux and WFPC-2 cratering flux estimates. Horizontal and vertical uncertainties on the HST data points were calculated in a similar manner as for the STS data points (see Section 2.4.2).

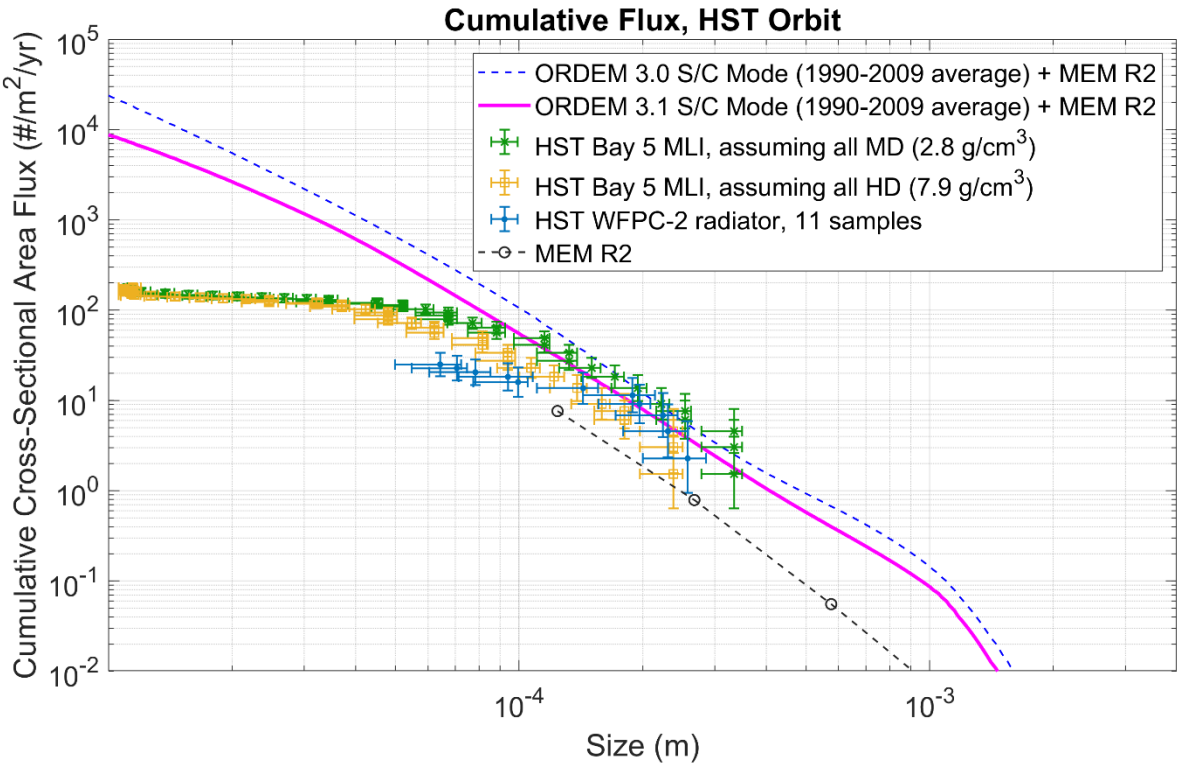

Figure 3-23. Comparison of the cumulative cross-sectional area flux vs size between ORDEM 3.0, ORDEM 3.1, and impact data from the HST Bay 5 MLI and WFPC-2 radiator. The ORDEM curves include the meteoroid flux estimates from the MEM R2 model. Two sets of MLI data points are shown, assuming all points as either MD or HD. The MEM R2 model results are also shown for reference.

3.4 OPTICAL-BASED POPULATIONS

3.4.1 Optical Measurements in GEO

MODEST data from the 2013–2014 observation period was used to validate the ORDEM 3.1 GEO population. The probability of detection for this MODEST dataset is shown in Figure 3-24 as a “tie-dye” pattern in the Cartesian coordinates of (INC·cos(RAAN), INC·sin(RAAN)). Darker red colors (> 0.8 on color scale) indicate a high probability of detection, given the observing geometry during the applicable period, and darker blue colors (< 0.4 on color scale) indicate low probabilities of detection. In this figure, the color scale is capped at 1.0, so any probabilities greater than 1.0 are reset to 1.0.

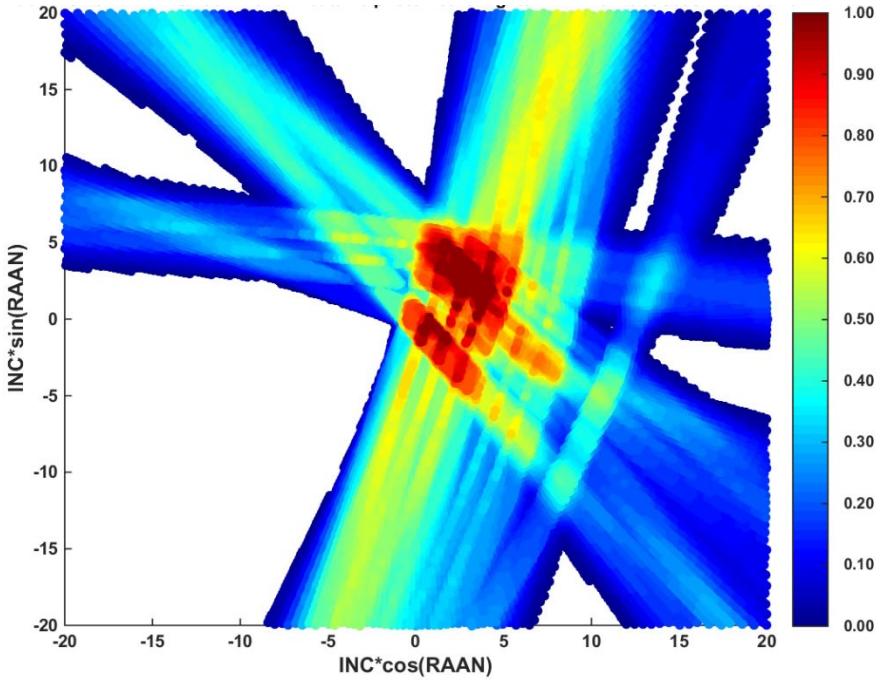

Figure 3-24. Probability of detection, in (INC· cos(RAAN), INC · sin(RAAN)) Cartesian space, for the 2013–2014 MODEST observation period.

After 2009, the end of the MODEST observation period used for building the ORDEM 3.1 GEO populations, a new camera was installed on MODEST that increased the field of view (FOV) from 1.3 by 1.3 degrees to 1.6 by 1.6 degrees. The effect of this increase in FOV is that more detections are possible for a given observing geometry in the 2013–2014 dataset as compared to the previous datasets. This does not necessarily increase the sensitivity of the telescope to be able to detect objects with a larger numerical magnitude (smaller size). Like the 2004–2006 and 2007–2009 datasets, the 2013–2014 dataset is considered complete down to approximately 30 cm in size (approximately 17th magnitude).

Similar to the ORDEM 3.1 development process, MODEST targets in the 2013–2014 dataset were propagated forward or backward in time to a common epoch at the midpoint of the observation period: 0 hr UT on 1 January 2014. UCTs were identified and filtered by size (30 cm – 1 m, approximately 14.1–17.1 magnitude) and using the debris ring filter applied for the ORDEM 3.1 population development (discussed in Section 3.3.3 of the ORDEM 3.1 Process Document). The debris ring filter is based on the angle between a target's specific angular momentum vector and a unit vector perpendicular to the stable Laplace plane inclined at 7.2° (Rosengren, Scheeres, & McMahon, 2014). Subsequent references to UCTs herein refer to UCTs filtered in this manner.

3.4.2 GEO Population Validation

For validation of the ORDEM 3.1 GEO population, comparisons between ORDEM 3.1 and the MODEST 2013–2014 UCTs and CT debris were made in clock angle distribution and cumulative size distribution.

3.4.2.1 Clock Angle Distribution

Comparisons in clock angle were performed between ORDEM 3.1 and the MODEST 2013–2014 dataset to ensure the model was accurately representing the orbital evolution of the GEO debris population built from the 2004–2009 composite MODEST dataset. Uncontrolled objects in GEO exhibit a natural precession in inclination-right ascension space due to effects from the Earth's oblateness and the gravity

of the Sun and the Moon. This natural precession traces out a loop in the Cartesian coordinates of (INC · cos(RAAN), INC · sin(RAAN)), which represents the projection of the orbit's angular momentum vector on the equatorial plane. Objects found to reside on or near this idealized loop represent GEO or near-GEO objects at various stages in their orbital evolution. Controlled (station-kept), intact objects will tend to clump near (0°,0°) in these coordinates, while derelict intact satellites and debris will tend to spread out in this ring in a clockwise fashion. The clock angle of an object is defined to represent this motion around the ring. The clock angle origin is defined by a vector originating at (7.2°,0°) and pointing in the (0°,0°) direction, and the angle increases in a clockwise direction, as shown in Figure 3-25. This clock angle is analogous to the "age" of orbits as they evolve away from 0° inclination, where most intact GEO satellites originate, under luni-solar perturbations. Fragments from older breakups, such as the Titan 3C Transtage (International Designator 1968-081E, SSN #3432) fragmentation event, are located closer to 270° clock angle and spread out across a larger range of clock angles.

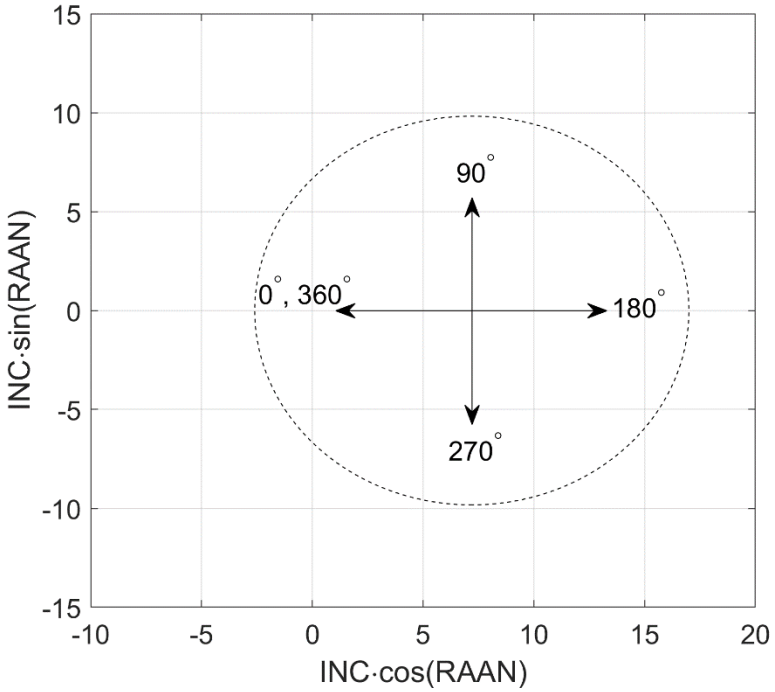

Figure 3-25: Clock angle as defined in (INC · cos(RAAN), INC · sin(RAAN)) Cartesian space, representing the direction of natural motion of uncontrolled GEO objects.

Initial comparisons of the ORDEM 3.1 GEO populations with MODEST 2013–2014 data showed more objects in the MODEST dataset in the clock angle ranges of 0–60° and 240–300°, as seen in Figure 3-26. This discrepancy suggests additional breakups occurred after 2009 (the end of the MODEST dataset used for ORDEM 3.1 development), and before 2013 (the beginning of the dataset used for ORDEM 3.1 validation). It is not surprising that unidentified breakups would have occurred during this time period. Due to difficulties of observing small debris in GEO, fragmentation events are sometimes identified years after the event actually took place. For example, prior to the 2004 MODEST observations, only four GEO breakups had been confirmed by the Combined Space Operations Center (CSpOC). Two of those breakups were made known to the ODPO only recently, more than 30 years after the breakups actually occurred, and only in terms of day of event, without any information as to state vector or ephemerides at the time of breakup. Thus, it is plausible that unidentified breakups occurred during the time between the MODEST datasets.

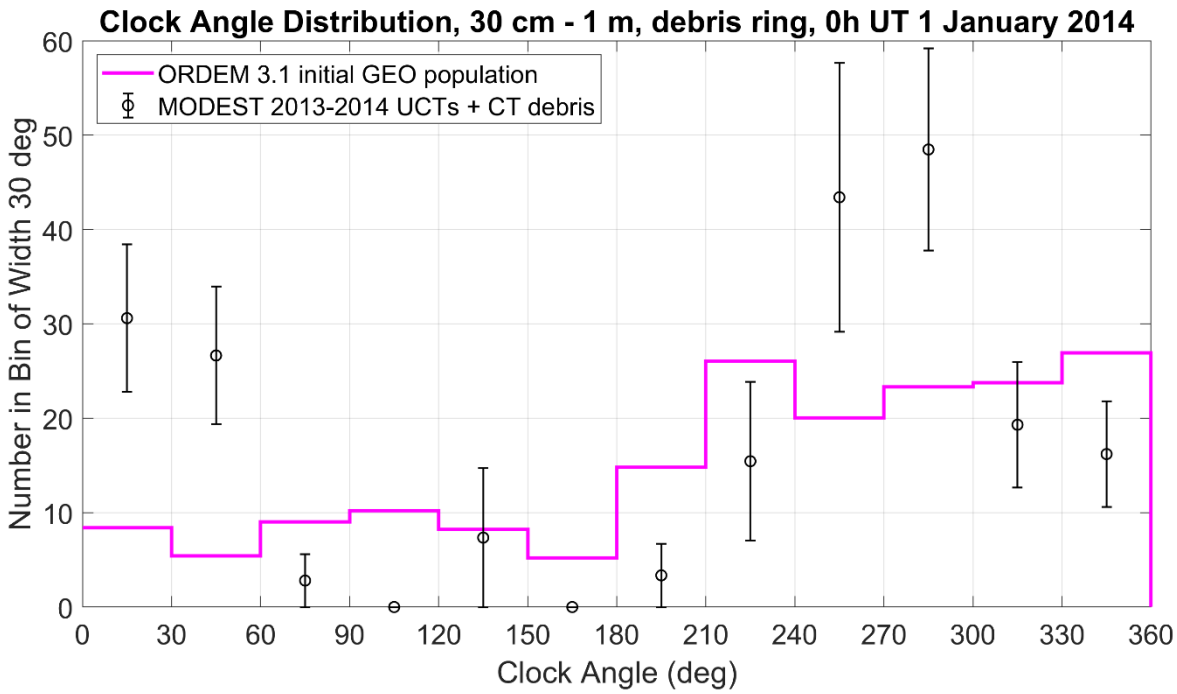

Figure 3-26: Comparison of the clock angle distribution between the initial ORDEM 3.1 GEO population and the MODEST 2013–2014 dataset.

To resolve the discrepancy between the GEO population modeled based on the 2004–2009 composite MODEST data and the later MODEST dataset, simulated breakups were added to the model populations. One breakup was added at the beginning of 2010 (0 hr UT on 1 January 2010) to address the discrepancy in the clock angle range 0–60°. The simulated parent object was assumed to have a mass of approximately 1900 kg, and the NASA Standard Satellite Breakup Model was used to model the breakup fragments. Through trial and error, a best match to the MODEST data was found by modeling the breakup with INC = 0°, RAAN = 0°, and mean longitude = 270°.

Another additional breakup was investigated to resolve the discrepancy between the model and the data in the 240–300° clock angle range. However, after an initial parametric investigation, a suitable breakup candidate time and orbit was not readily evident. While this is an area of ongoing investigation, for the purposes of ORDEM 3.1, fragments were added directly to the initial GEO population in this clock angle range in order to better match the data. Approximately 50 extra fragments were added to the ORDEM populations at the beginning of 2014 using the orbital element distributions from the 2013–2014 dataset. Orbits were assigned to the extra fragments based on the objects in the MODEST 2013–2014 dataset with clock angle between 240° and 300°, similar to the method used for assigning non-circular orbital elements to UCTs and objects with size less than 30 cm for building the ORDEM 3.1 GEO population (as discussed in Section 3.3.4 of the ORDEM 3.1 Process Document). Objects were drawn from the cumulative distribution in weight of the MODEST UCTs and CT debris, and the orbit, size, and weight of the selected object was assigned to the extra fragment. Thus, orbits and sizes of targets with higher weights were more likely to be assigned to the extra fragments.

Figure 3-27 shows the final ORDEM 3.1 GEO population, after the addition of fragments from these two simulated breakups, as compared to the MODEST 2013–2014 UCTs and CT debris. The model is clearly improved by the addition of the simulated breakups and is generally within the one σ-confidence intervals of the MODEST data. Overall, the comparison is considered a good match.

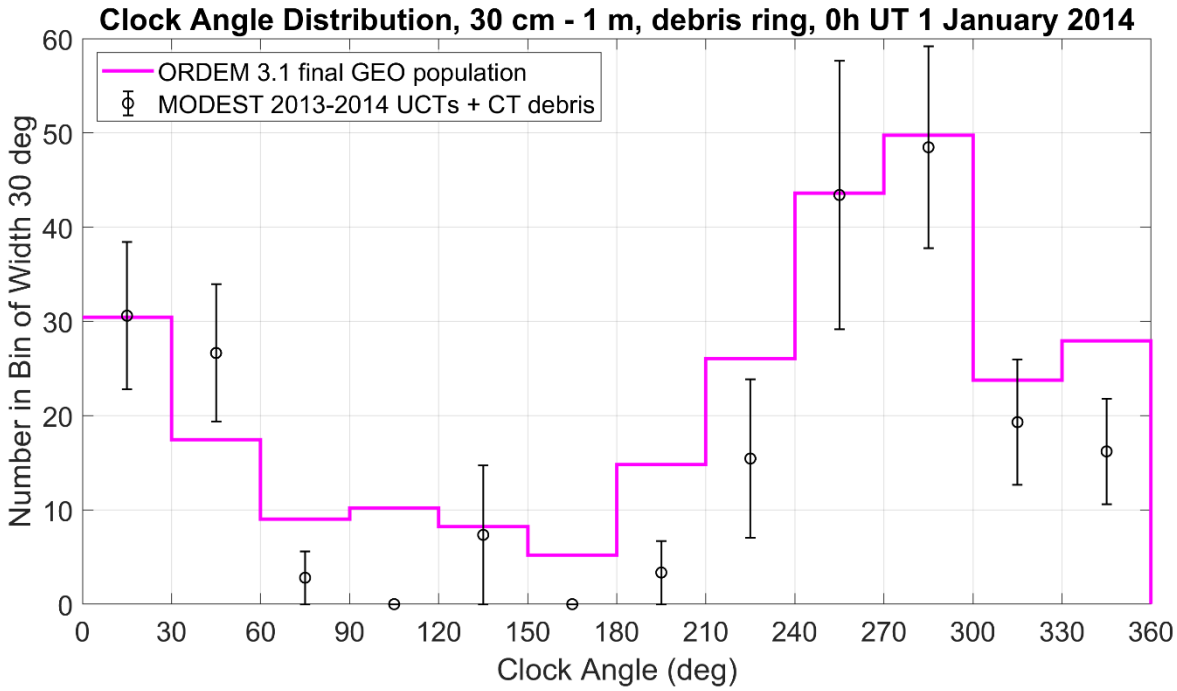

Figure 3-27: Comparison of the clock angle distribution between the final ORDEM 3.1 GEO population, including the addition of two simulated breakups, and the MODEST 2013–2014 dataset.

3.4.2.2 Cumulative Number vs Size

An additional validation comparison of the ORDEM 3.1 GEO population to the MODEST data was made using the cumulative size distribution of objects from 10 cm to 1 m. The discrepancy between the initial ORDEM 3.1 GEO population and the MODEST 2013–2014 dataset is also evident in Figure 3-28 ("ORDEM 3.1 initial GEO population" curve), where the model begins to diverge from the data below approximately 50 cm. With the addition of the two simulated breakups, the modeled cumulative size distribution is in very good agreement with the MODEST 2013–2014 dataset, as seen from the "ORDEM 3.1 final GEO population" curve in Figure 3-28.

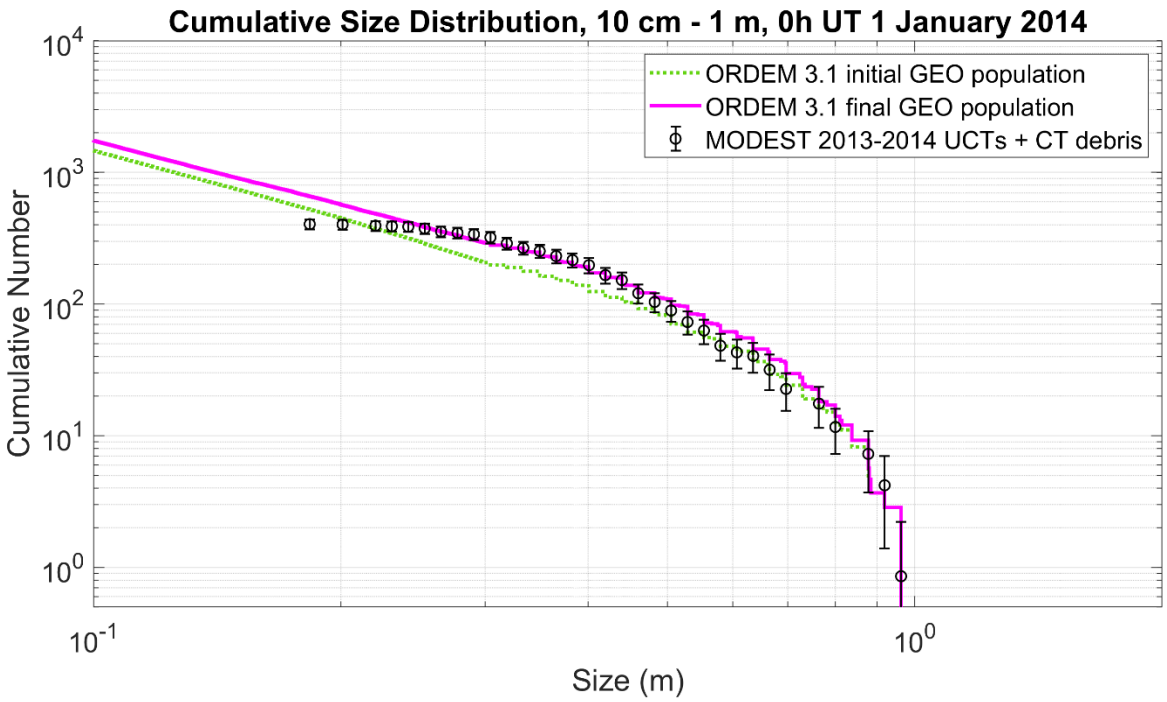

Figure 3-28: Comparison of the cumulative size distribution between the ORDEM 3.1 initial and final GEO populations and the MODEST 2013–2014 UCTs and CT debris.

3.4.3 Bootstrap Analysis for Optical Data

Because the GEO data is obtained by summing over detections with different weights, the analysis of the statistics is more complex than that for the radar-based populations. The simplest way to compare optical data to predictions is to use a bootstrap analysis. The measured value for a particular subset of detections (*e.g.*, within a particular clock angle bin, as considered here) is a sum over the weighted values of N detections within that subset

$$measured = \sum_{j=1}^{N} w_j \qquad 3.4\text{-}1$$

The Bootstrap method seeks to estimate the uncertainty in this measured value by resampling the weighted values, with replacement. Each resampling will give a new bootstrap estimate of the measured value, and the distribution of these measured values an estimate of the distribution of possible actual values. We can then compare the distribution to the ORDEM predicted value to estimate the likelihood that the data came from the predicted value.

Standard bootstrap techniques use resample sizes that are the same as the original size, *i.e.*, N. However, debris detections are a Poisson process where the number of samples can vary when resampling.

A way to think about this is not to envision N objects detected, but a very large number of measurements M in small divisions of time ($M >> N$), where the vast majority of the measurement times have zero detections. If we resample from this set of M time segments M times in a standard bootstrap scheme with replacement, then the probability of resampling any given time segment an integer number of times k is given by a binomial probability:

$$P_B = \frac{M!}{(M-k)!\,k!}\left(\frac{1}{M}\right)^k\left(1-\frac{1}{M}\right)^{M-k}. \quad 3.4\text{-}2$$

Taking the limit of this equation as $M \to \infty$ gives

$$P_B = \frac{1}{e\;k!} = \frac{e^{-1}(1)^k}{k!}. \quad 3.4\text{-}3$$

So the probability of getting k resamples of any time bin (for our purposes, a bin with a detection in it) is simply the Poisson probability for getting k samples with an expectation value of 1. So, rather than dividing up the data into M time segments, resampling, and summing (where most values are zero), we can simply resample each of the N data values k_{BS} times using a Poisson sampler and expectation value 1. The resampled integer values would have the breakdown shown in Table 3-2.

Table 3-2: Probability of being resampled, P_{BS}, for each sampled integer value k_{BS}.

Sampled Integer Value k_{BS}	**Probability of being Sampled P_{BS}**
0	36.8%
1	36.8%
2	18.4%
3	6.1%
4	1.5%

After each resampling, the $measured_{BS}$ value is recomputed as

$$measured_{BS} = \sum_{j=1}^{N} k_{BSj} w_j \quad 3.4\text{-}4$$

where N is still the number of detections.

The easiest way to compare to the ORDEM predicted value is to count what fraction of the $measured_{BS}$ values are less than the predicted value. This gives a one-sided p-value, p_1. A two-sided p-value p_2 can also be computed from the one-sided p-value p_1 by

$$p_2 = 2\,Min[p_1, 1-p_1] \quad 3.4\text{-}5$$

A high value for p_2 indicates a very close fit between data and prediction.

Using the GEO data in Figure 3-27 gives the values for p_1 and p_2 shown in Table 3-3. Note that for two of the bins, there were insufficient data to come up with an empirical value. This is due to the incomplete coverage of the MODEST validation data set for these clock angles. As there were no weightings to use for the bootstrap method, these two cases were ignored for the analysis.

Table 3-3: Bootstrap values for p_1 and p_2 from the distribution in clock angle for the final ORDEM 3.1 GEO population, including the addition of two simulated breakups, and the MODEST 2013–2014 dataset.

"Clock Angle" Bin	ORDEM Prediction	Measured Value	Bootstrap p_1	Bootstrap p_2
0°–30°	30.42	30.61	0.511	0.978
30°–60°	17.44	26.65	0.096	0.192
60°–90°	9.01	2.80	0.981	0.038
90°–120°	10.21	-	-	-
120°–150°	8.22	7.35	0.736	0.528
150°–180°	5.20	-	-	-
180°–210°	14.80	3.36	0.996	0.008
210°–240°	26.05	15.45	0.888	0.224
240°–270°	43.60	43.41	0.531	0.938
270°–300°	49.76	48.48	0.562	0.876
300°–330°	23.76	19.31	0.758	0.484
330°–360°	27.93	16.21	0.973	0.054

In the frequentist interpretation, a model with "good" coverage should have a p-value of 0.1 or lower about 10% of the time, a value of 0.2 or lower 20% of the time, *etc.* The p-values should be uniformly distributed under the null hypothesis. In order to measure the distribution in p-values, Kuiper's test was conducted on each p-value distribution, to see if it follows such an ideal distribution. A high Kuiper statistic is indicative of a high probability that the sampled data (in this case, the p-values) came from the theoretical distribution (in this case, a uniform distribution) (Matney, 2008). For p_1, the p-value for Kuiper's test is 0.258, indicating the distribution is within the 90% confidence limits. Similarly, for p_2, the p-value for Kuiper's test is 0.150. This also is within the 90% confidence limit.

4 SUMMARY AND CONCLUSIONS

The V&V process used to assess the ORDEM 3.1 model has been described using the most recent data sources available to the ODPO from HUSIR, Goldstone, STS, HST, and MODEST. During the build process, data sources were used to scale the model such that it matched – to the extent possible – the data in the orbital regimes and orbital debris sizes where such comparisons could be made. As detailed in Section 2, good agreement between the population build sources and model was obtained. Testing of the applicability of the model to data collections from the same sensor in later years or independent measurement sources was conducted for validation purposes in Section 3, and these were shown to provide good agreement with the model as well – exhibiting a better match than ORDEM 3.0 to this recent data.

5 REFERENCES

Abercromby,K.J., Seitzer, P.,*et al*., *Michigan Orbital DEbris Survey Telescope Observations of the Geosynchronous Orbital Debris Environment, Observing Years: 2004 – 2006*, NASA/TP-2010-216129, August 2010.

Abercromby, K.J., Seitzer, P.,*et al*., *Michigan Orbital DEbris Survey Telescope Observations of the Geosynchronous Orbital Debris Environment, Observing Years: 2007 – 2009*, NASA/TP-2011-217350, September 2011.

Barker, E.S., J. L. Africano, *et al.*, "Analysis of Working Assumptions in the Determination of Populations and Size Distributions of Orbital Debris from Optical Measurements," *Proceedings of the 2004 AMOS Technical Conference*, Wailea, Maui, HI, pp. 225-235, 2004.

Barton, D. K., *et al.*, *Final Report of the Haystack Orbital Debris Data Review Panel,* NASA/JSC Technical Memorandum 4809, Houston, TX, February 1998.

Bohannon, G., Caampued, T., and Young, N,. *First Order RCS Statistics of Hypervelocity Impact Fragments.* XonTech Report 940128-BE-2305, April, 1994.

Hyde, J., Christiansen, E., and Lear, D., "Shuttle MMOD Impact Database," Procedia Engineering, 103, pp. 246 – 253, 2015.

Dalquist, C. and Bohannon, G., *Physical Descriptions of Debris Objects Used in Static RCS Measurements*. XonTech Report 910555-1978, August 1991.

Everett, R., Caampued, T., and Chu, J., *Summary of Data Processing of September 1990 SPC Debris Data*. XonTech Report 910147-1937, March 1991.

Everett, R., Dalquist, C., and Caampued, T,. *Summary of Processing of January 1991 SPC Debris Data*. XonTech Report 9100393-1965, July 1991.

J.M. Hilbe, Modeling Count Data, Cambridge University Press, New York, Chapters 5 and 8, 2014.

Hill, N., "Measurement Techniques for Hypervelocity Impact Test Fragments," 59th International Astronautical Congress, September-October 2008, Glasgow, Scotland.

Johnson, N.L., Kemp, A.W., Kotz, S., Univariate Discrete Distributions, 3rd Edition, Wiley, New Jersey, pp. 165 – 197, 2005.

Manis, A, *et. al*., *ORDEM 3.1 Model Process*, NASA TP-TBD, 2022.

Matney, M.J., "Statistical Issues for Uncontrolled Reentry Hazards," 3rd IAASS Conference, Rome, Italy, 2008.

Moorhead, A.V, Koehler, H.M., and Cooke, W.J., NASA Meteoroid Engineering Model Release 2.0, NASA/TM-2015-218214, October 2015.

Mulrooney, M., Matney, M., and Barker, E., "A New Bond Albedo for Performing Orbital Debris Brightness to Size Transformations," IAC-08.A6.2.7, 2008.

National Aeronautics and Space Administration, "What is the A-Train?" http://www.atrain.nasa.gov/ Accessed February 13, 2022.

Opiela, J.N., Liou, J.-C., and Anz-Meador, P.D., **"**Data Collected During the Post-Flight Survey of Micrometeoroid and Orbital Debris Impact Features on the Hubble Wide Field Planetary Camera 2," IAC-10.A6.1.10, 2010.

Rosengren, A.J., Scheeres, D.J., and McMahon, J.W., "The classical Laplace plane as a stable disposal orbit for geostationary satellites," Adv. Space Res., 53, pp. 1219-1228, 2014.

Steele, M.J., *et. al.*, *Standard for Models and Simulations*, NASA-STD-7009A, December 2016.

Stokely, C.L., Benbrook, J.R., Horstman, M., "On the Determination of Poisson Statistics for Haystack Radar Observations of Orbital Debris," Proceedings of the 58th International Astronautical Congress, pp. 1743 – 1750, 2007.

Vavrin, A., Manis, A., *et al.*, NASA Orbital Debris Engineering Model ORDEM 3.1 –Software User Guide, NASA/TP-2019-220448, NASA Johnson Space Center, Houston, TX, USA, December 2019.

Xu, Y.-l and C.L. Stokely., "A Statistical Size Estimation Model for Haystack and HAX Radar Detections," 56th International Astronautical Congress, Fukuoka, Japan, 2005.

A ORDEM 3.1 SUPPORT SOFTWARE AND DATABASES

This section describes the support software used in the development of the ORDEM 3.1 software release. They may all be considered as legacy products in that they have been developed and tested over decades. The first three – LEGEND, the space traffic database, and solar flux activity tables – are in-house ODPO products that are vetted through the ODPO Configuration Control Board (CCB) process. The last two, Piecewise Cubic Hermite Interpolant Package (PCHIP) and TeeChart charting library, developed by the registered company Steema Software SL in Barcelona, are off-the-shelf government and commercial products, respectively.

A.1 LEGEND

The LEGEND three-dimensional, long-term environment model was used during the development of ORDEM 3.1 to provide baseline orbital debris populations for sizes of 1 mm and larger. To simulate future traffic in LEGEND, future populations were added via an 8-year launch cycle, as commonly adopted by the international debris modeling community. These future populations (*i.e.*, rocket bodies, spacecraft, operational debris) were based on LEGEND model runs using nominal assumptions for breakup rates, launch rates, and solar activity. A 90% compliance rate of post mission disposal (*i.e.*, "25-year rule") was assumed. After an 8-year operational lifetime for spacecraft, the orbit was lowered such that the object would reenter the atmosphere within 25 years. The LEGEND model was used in a Monte Carlo manner, and the mean and variance of the number of objects over 100 Monte Carlo runs was used for building the ORDEM 3.1 populations and uncertainties for years 2016 through 2050. LEGEND (and LEGEND variant) software were subject to continuing, informal V&V efforts during their development, including the extensive use of legacy software. The V&V of LEGEND is beyond the scope of this document.

A.2 SPACE TRAFFIC DATABASE

The space traffic database consist of historical yearly space launch traffic, maneuvers conducted in space (*e.g.*, re-orbit or deorbit maneuvers), and fragmentation events (collisions and explosions) that are stored in the ODPO-controlled Launches, Intacts, Maneuvers, Breakup Objects (LIMBO) web application. Space traffic data is exported as text files and used by LEGEND as historical inputs, and the previous eight years of launches were repeated in a serial fashion to serve as a basis for future space traffic. For the non-GEO populations, the years 1957–2014 were used as the historical inputs, and the launch traffic cycle of 2007–2014 was repeated every 8 years. For the GEO populations, the historical period covered 1957–2015, and the years 2008–2015 were repeated. The difference in the years covered by the non-GEO and GEO regions is due to a revision in the time period of radar data to be used for building the ORDEM 3.1 populations, which occurred after the non-GEO LEGEND runs through 2014 were completed. Orbital and physical data are regularly reviewed and corrected, augmented, and/or updated as necessary. The files are reviewed on a yearly basis during the construction of the latest year's input data.

A.3 SOLAR FLUX ACTIVITY

The solar flux activity model is an ODPO software tool that generates solar cycle projections for the solar flux component (*i.e.*, 10.7 cm radio wavelength) that affects atmospheric density calculations. Solar activity, as expressed by the Extreme Ultraviolet analogue of the 10.7 cm radio flux, is an important LEGEND input file. The radio flux governs the exospheric temperature and hence the atmospheric density as a function of altitude. Atmospheric drag is a function of atmospheric density. Therefore, the rate at which LEO debris is removed from orbit by atmospheric drag depends upon historical (1957–2015) and modeled (2016–2050) solar activity. Both historical and projected data sets are provided by the National Atmospheric and Oceanic Administration (NOAA), and long-term projections are made based on curve fits to the historical measurements. The April 2016 solar flux activity table was used for ORDEM 3.1, which contains measurement data up to that time and predicted future flux values out to 2050. A formal V&V of the projected solar activity is beyond the scope of this document.

A.4 PCHIP

The PCHIP computer software suite was used to provide interpolation of fluxes while enforcing the cumulative (or monotone) nature of ORDEM 3.1 distributions, (*e.g.*, flux as a function of projectile size). The subroutines pchim, pchfe, pchst, chfev, and xermsg constitute the suite. PCHIP is a Department of Energy (DOE)-developed suite licensed for distribution with ORDEM 3.1 by the DOE Office of Scientific and Technical Information's Energy Science and Technology Software Center. It is a government off-the-shelf (GOTS) product and was not included in the ORDEM 3.1 V&V effort.

A.5 TEECHART

TeeChart.NET is a standard graphical software product licensed from Steema Software (www.steema.com) for distribution with ORDEM 3.1. It is a commercial off-the-shelf (COTS) product and was not included in the ORDEM 3.1 V&V effort.

B ALTITUDE BAND COMPARISONS OF ORDEM 3.1 AND RADAR DATA

This Appendix includes additional cumulative surface area flux versus SEM size comparisons, not covered in Section 3, between ORDEM 3.0, 3.1, and radar data sets from HUSIR 2016–2017 and Goldstone 2016. Each plot represents a comparison on an altitude limited basis and is included for completeness of the comparison between ORDEM 3.1 and the radar datasets used for validation purposes. Goldstone data appears for altitudes above 650 km, which are altitudes where the flux measured by Goldstone has sufficient counts for the limited number of hours obtained from Goldstone to provide meaningful comparisons. Uncertainties plotted for the measured radar data in all plots are the one σ confidence intervals described in Section 2.2.4.

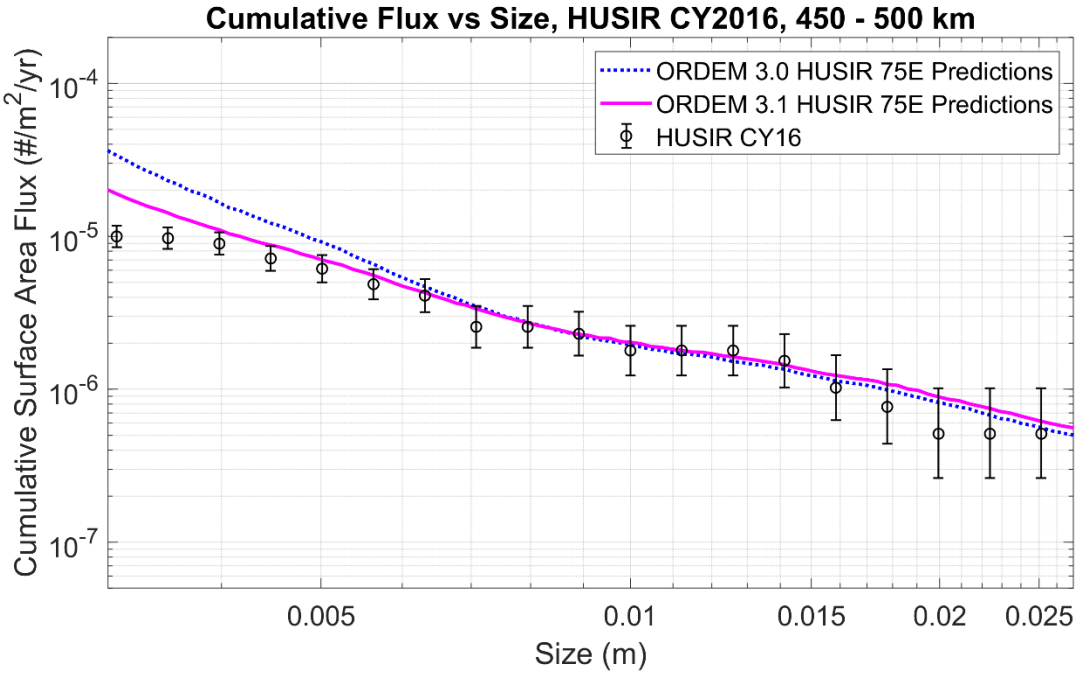

Figure B-1. Comparison of the surface area flux vs SEM size between ORDEM 3.0, ORDEM 3.1, and measurements from HUSIR 75E in 2016. The altitude is restricted to 450–500 km.

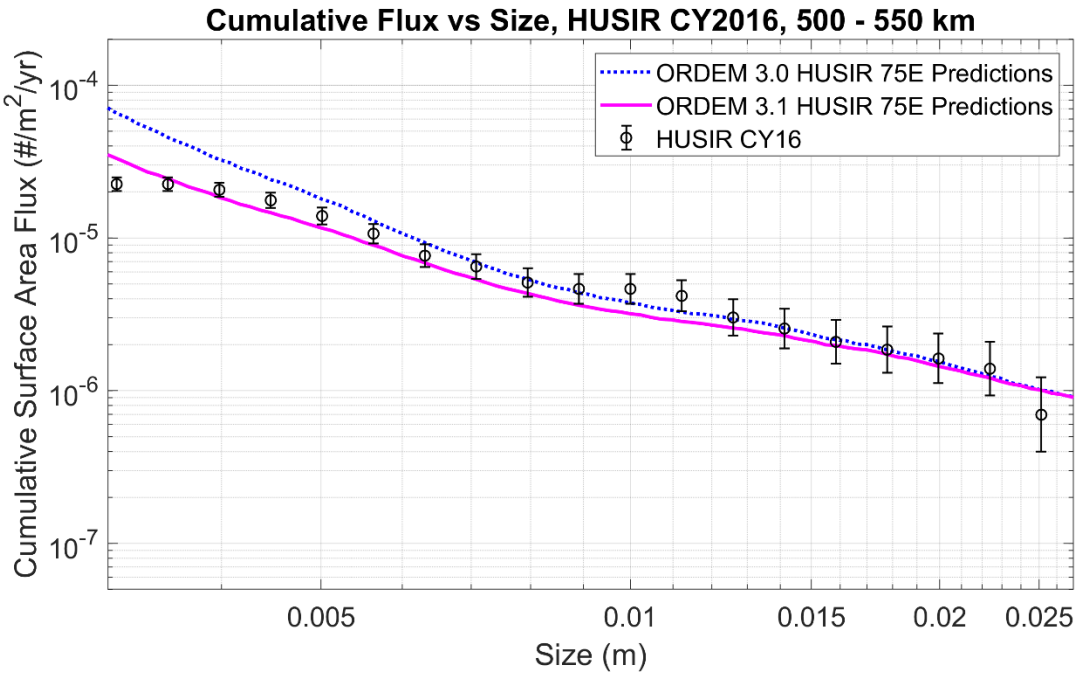

Figure B-2. Comparison of the surface area flux vs SEM size between ORDEM 3.0, ORDEM 3.1, and measurements from HUSIR 75E in 2016. The altitude is restricted to 500–550 km.

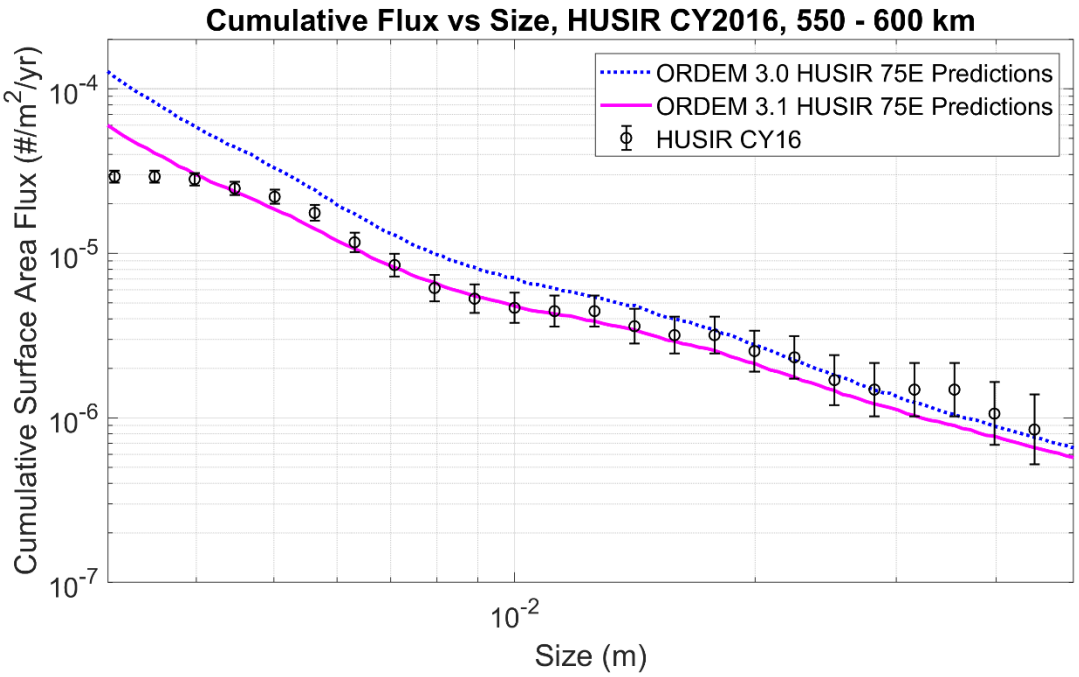

Figure B-3.Comparison of the surface area flux vs SEM size between ORDEM 3.0, ORDEM 3.1, and measurements from HUSIR 75E in 2016. The altitude is restricted to 550–600 km.

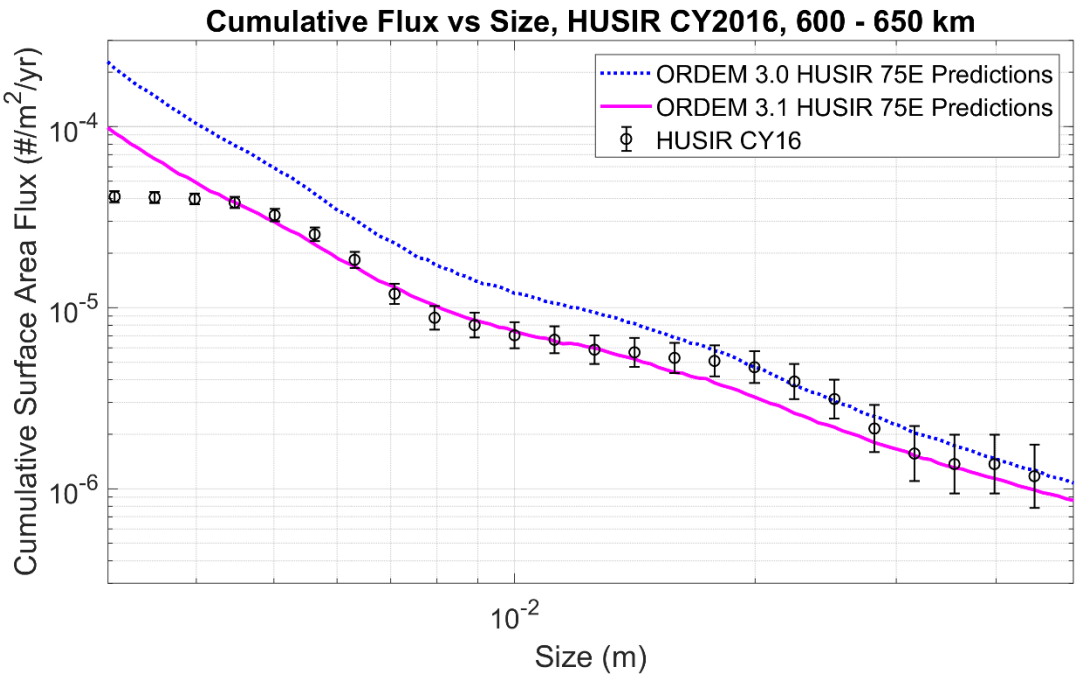

Figure B-4. Comparison of the surface area flux vs SEM size between ORDEM 3.0, ORDEM 3.1, and measurements from HUSIR 75E in 2016. The altitude is restricted to 600–650 km.

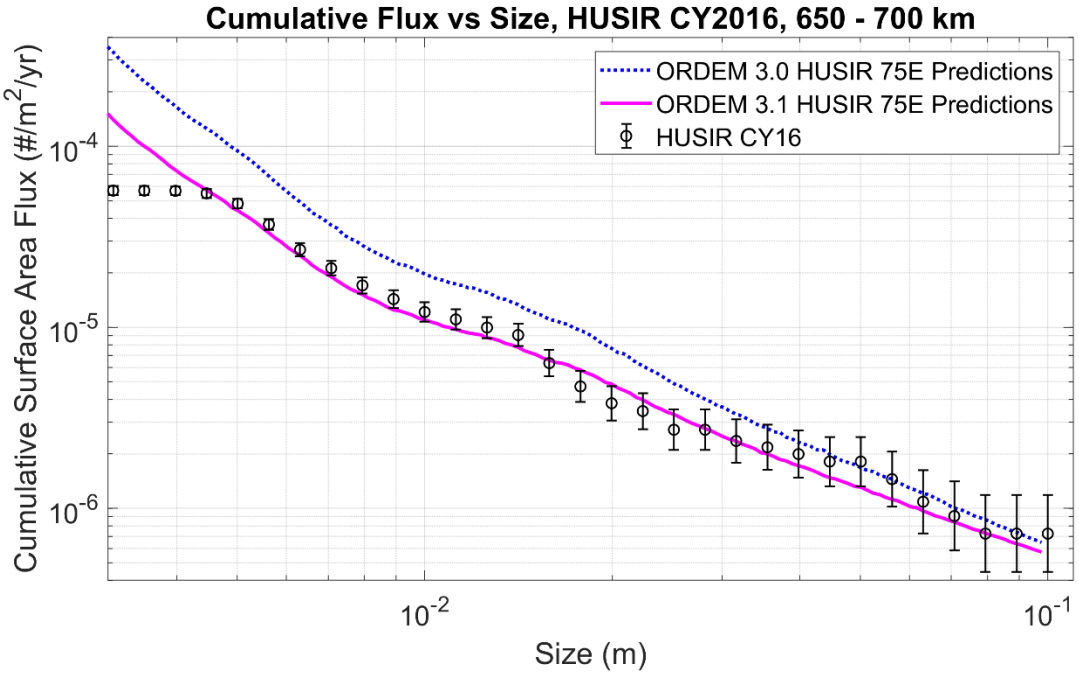

Figure B-5. Comparison of the surface area flux vs SEM size between ORDEM 3.0, ORDEM 3.1, and measurements from HUSIR 75E in 2016. The altitude is restricted to 650–700 km.

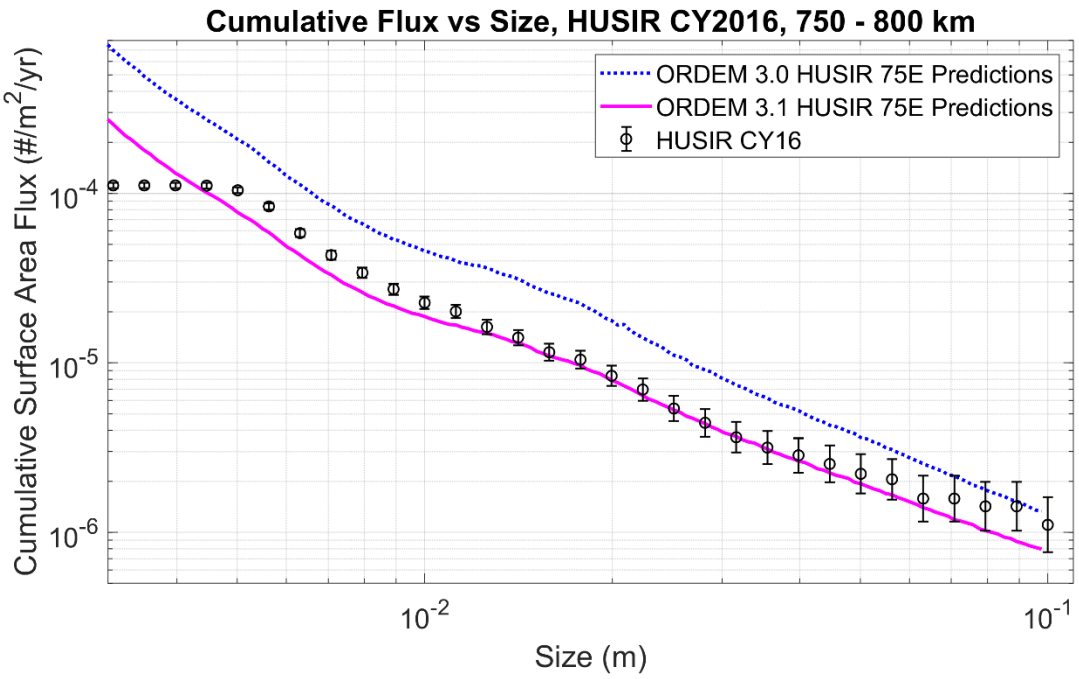

Figure B-6. Comparison of the surface area flux vs SEM size between ORDEM 3.0, ORDEM 3.1, and measurements from HUSIR 75E in 2016. The altitude is restricted to 750–800 km.

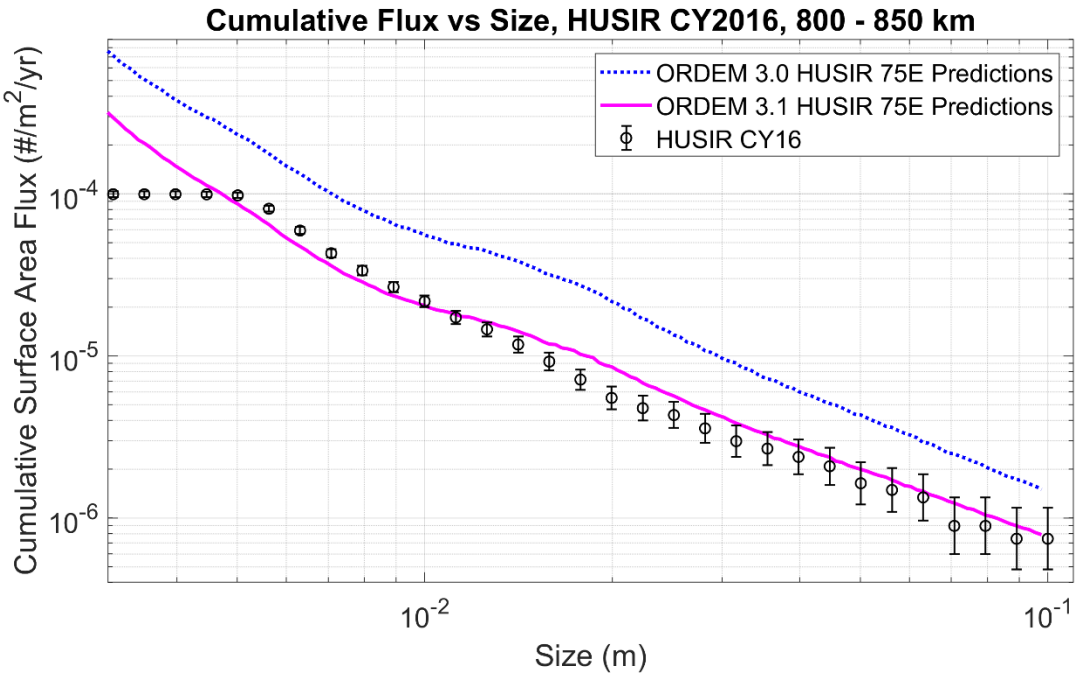

Figure B-7. Comparison of the surface area flux vs SEM size between ORDEM 3.0, ORDEM 3.1, and measurements from HUSIR 75E in 2016. The altitude is restricted to 800–850 km.

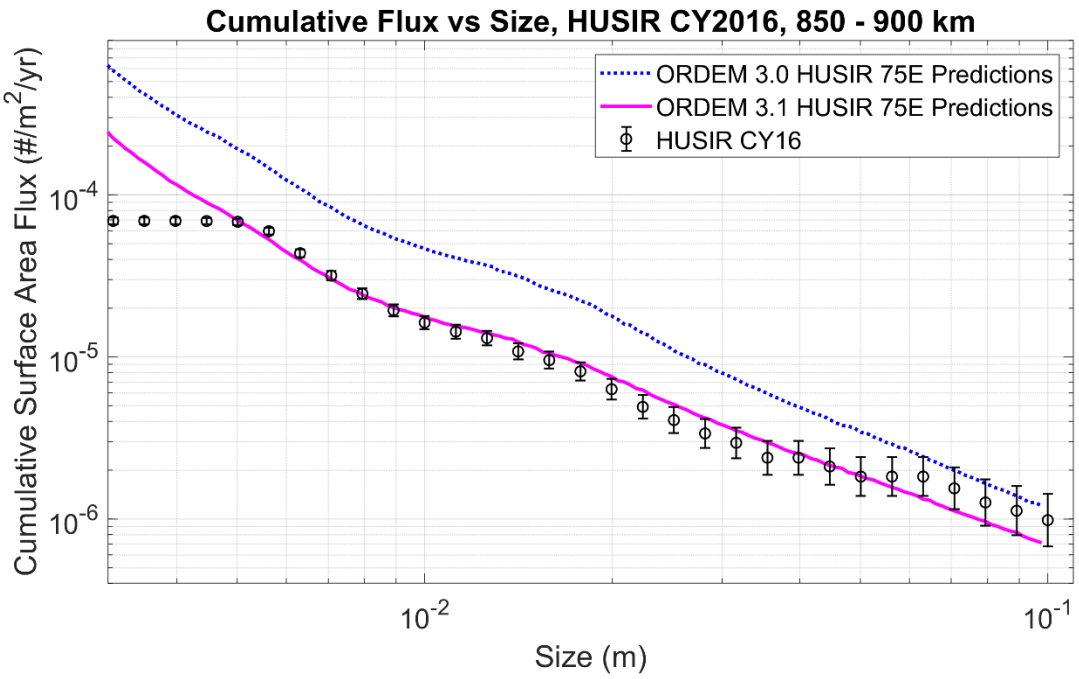

Figure B-8. Comparison of the surface area flux vs SEM size between ORDEM 3.0, ORDEM 3.1, and measurements from HUSIR 75E in 2016. The altitude is restricted to 850–900 km.

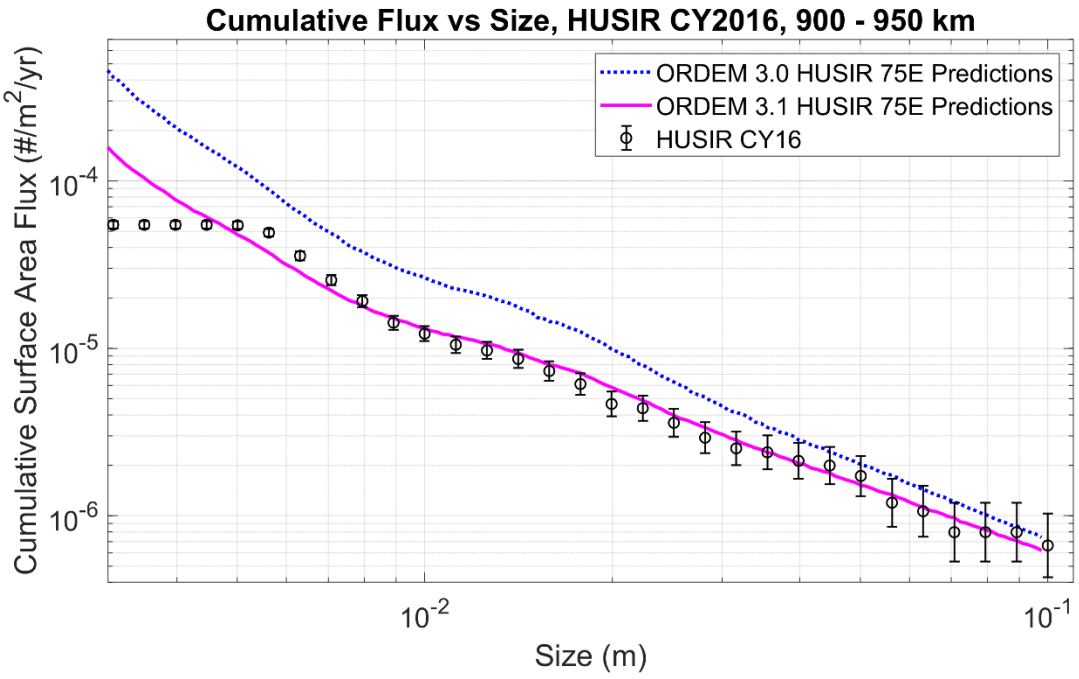

Figure B-9. Comparison of the surface area flux vs SEM size between ORDEM 3.0, ORDEM 3.1, and measurements from HUSIR 75E in 2016. The altitude is restricted to 900–950 km.

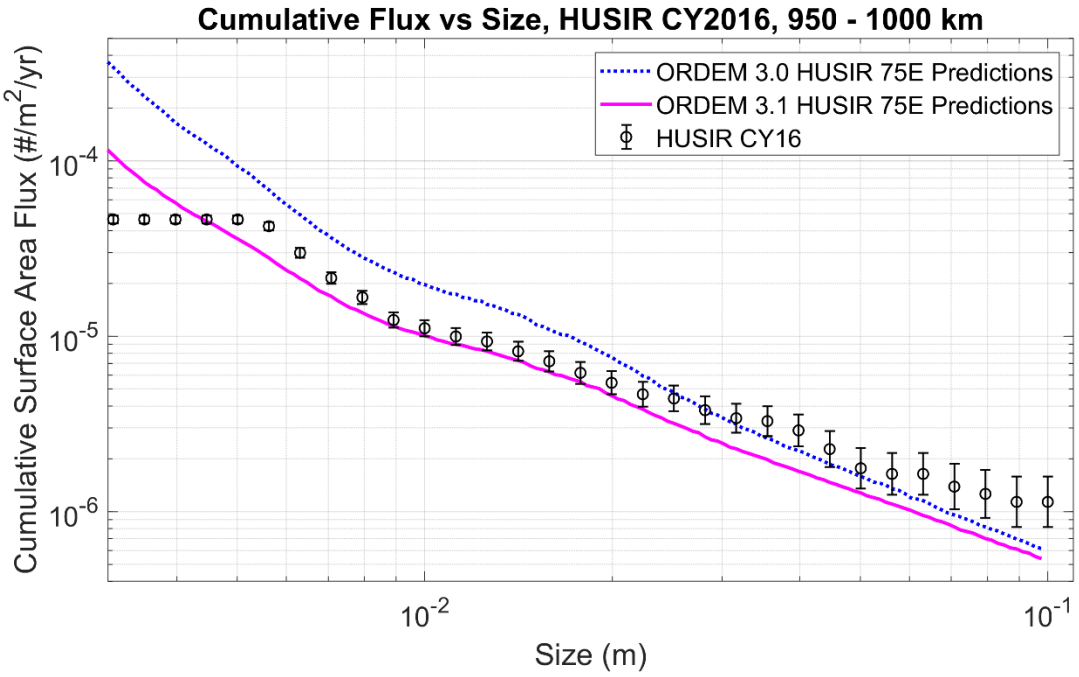

Figure B-10. Comparison of the surface area flux vs SEM size between ORDEM 3.0, ORDEM 3.1, and measurements from HUSIR 75E in 2016. The altitude is restricted to 950–1000 km.

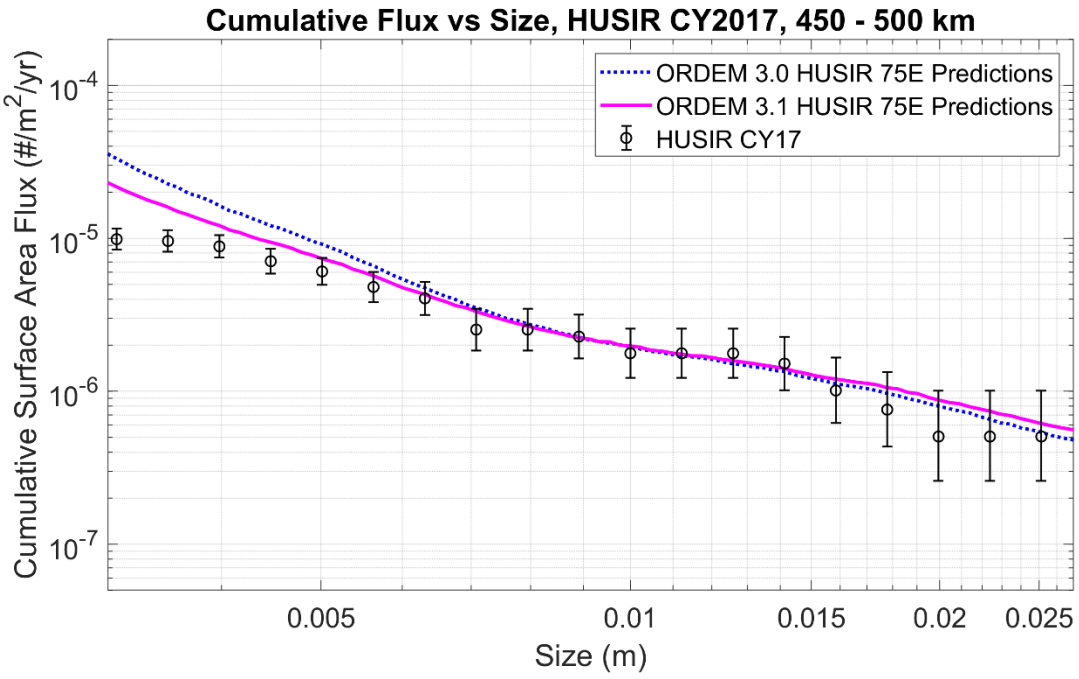

Figure B-11. Comparison of the surface area flux vs SEM size between ORDEM 3.0, ORDEM 3.1, and measurements from HUSIR 75E in 2017. The altitude is restricted to 450–500 km.

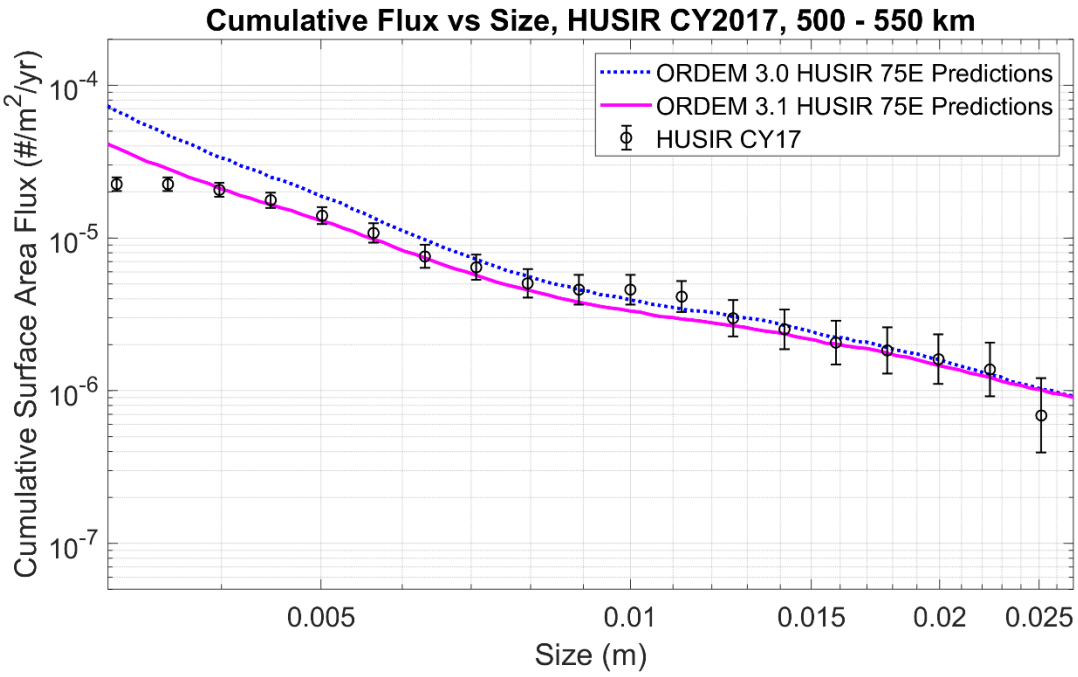

Figure B-12. Comparison of the surface area flux vs SEM size between ORDEM 3.0, ORDEM 3.1, and measurements from HUSIR 75E in 2017. The altitude is restricted to 500–550 km.

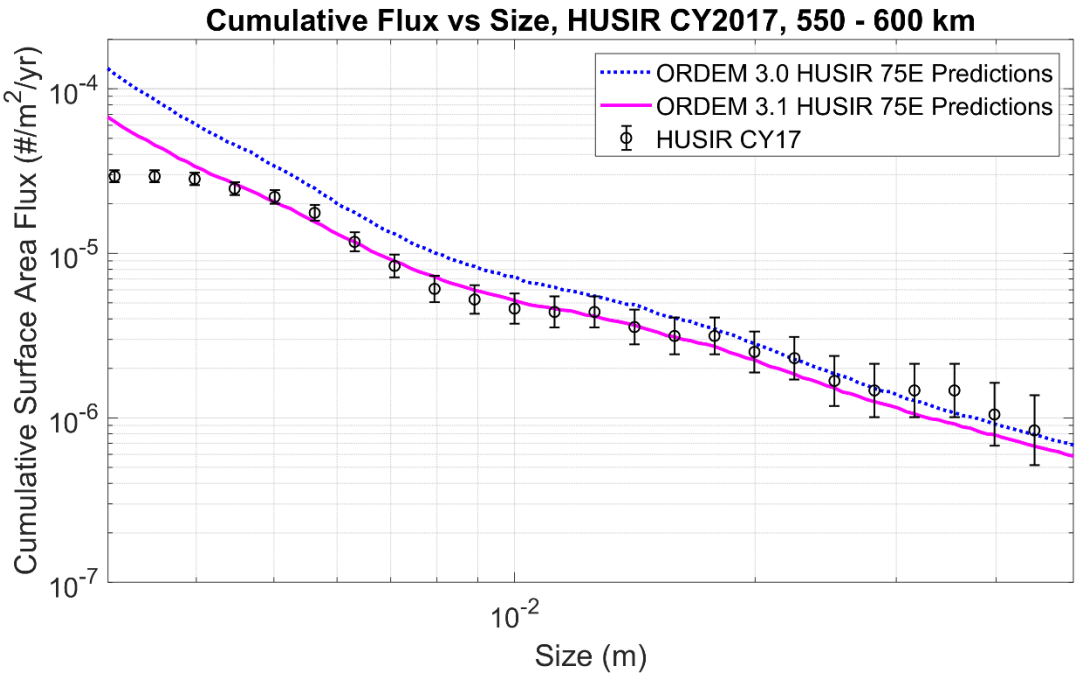

Figure B-13. Comparison of the surface area flux vs SEM size between ORDEM 3.0, ORDEM 3.1, and measurements from HUSIR 75E in 2017. The altitude is restricted to 550–600 km.

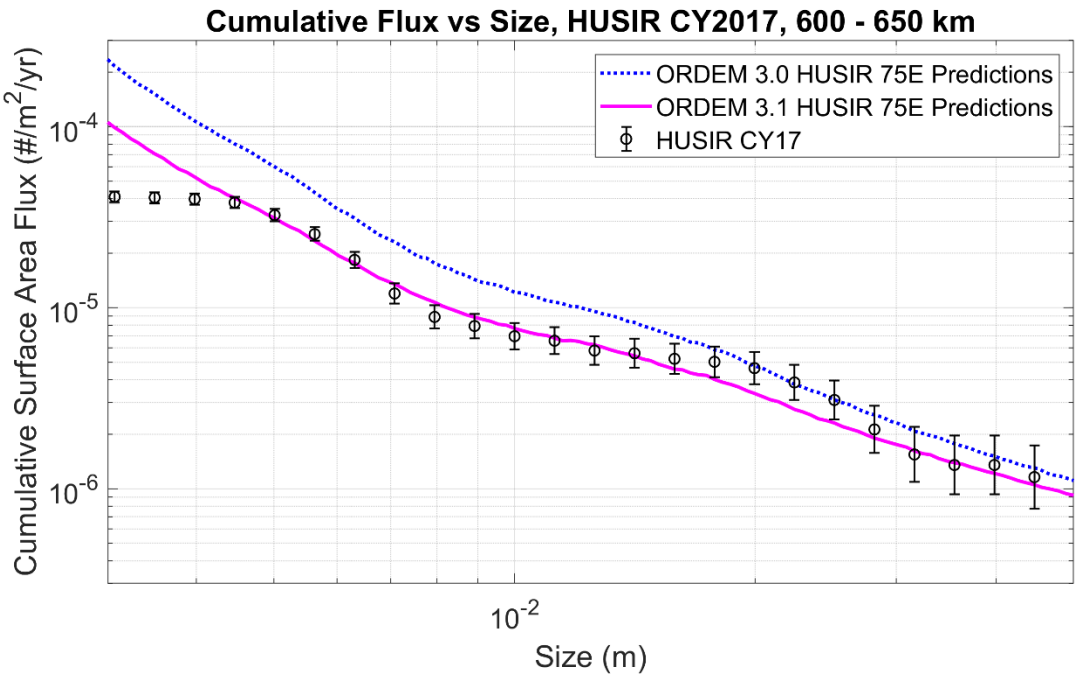

Figure B-14. Comparison of the surface area flux vs SEM size between ORDEM 3.0, ORDEM 3.1, and measurements from HUSIR 75E in 2017. The altitude is restricted to 600–650 km.

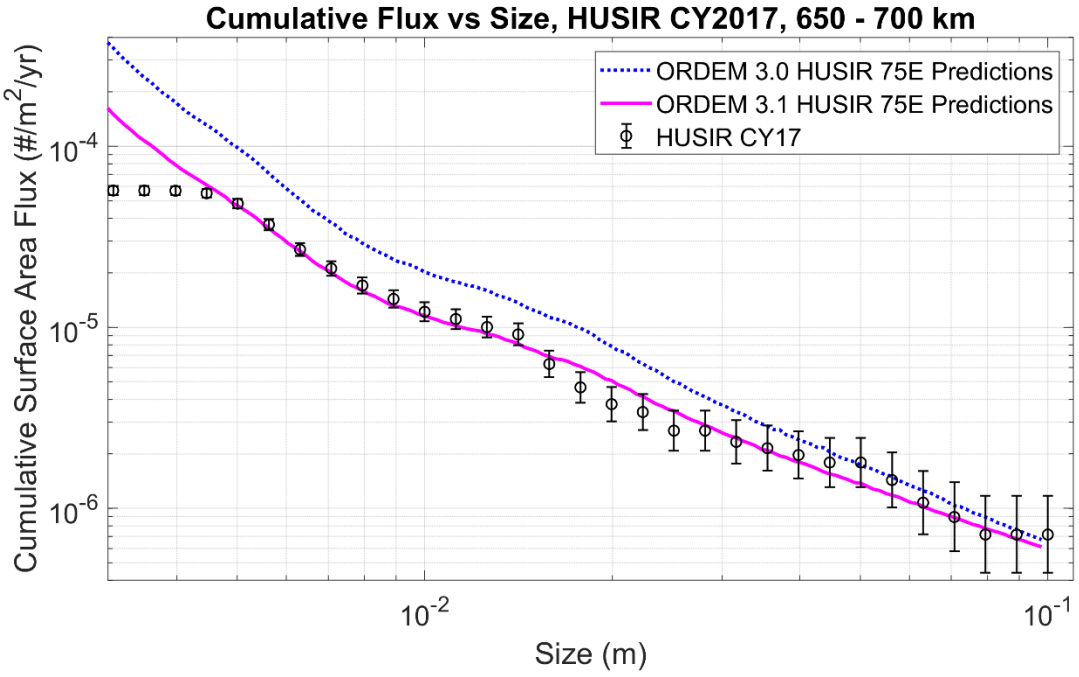

Figure B-15. Comparison of the surface area flux vs SEM size between ORDEM 3.0, ORDEM 3.1, and measurements from HUSIR 75E in 2017. The altitude is restricted to 650–700 km.

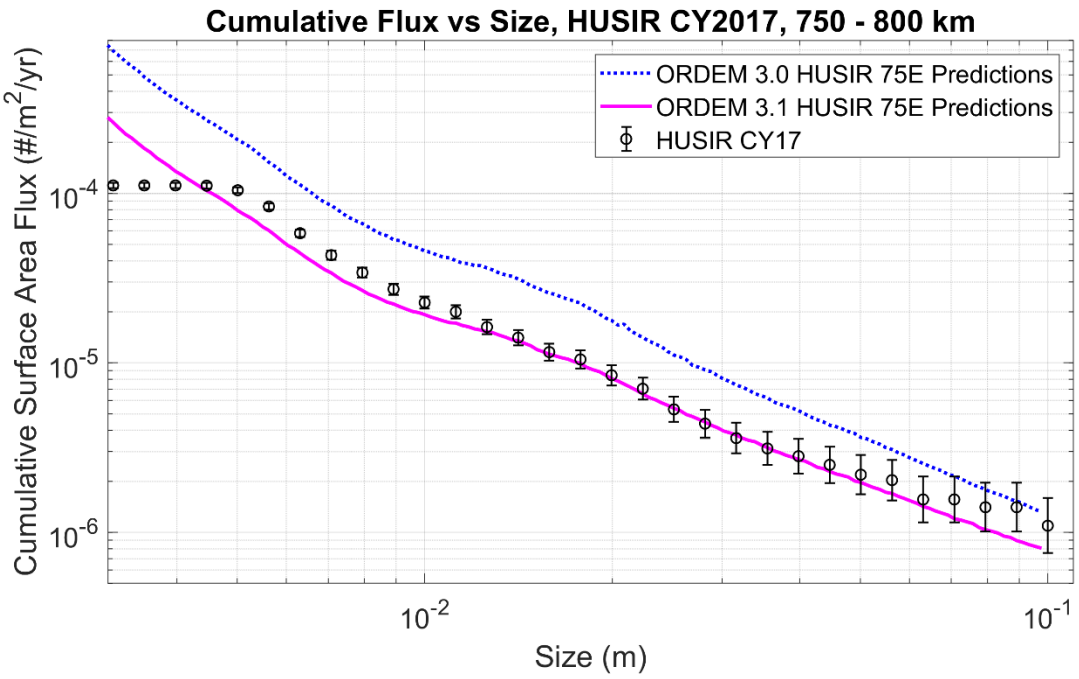

Figure B-16. Comparison of the surface area flux vs SEM size between ORDEM 3.0, ORDEM 3.1, and measurements from HUSIR 75E in 2017. The altitude is restricted to 750–800 km.

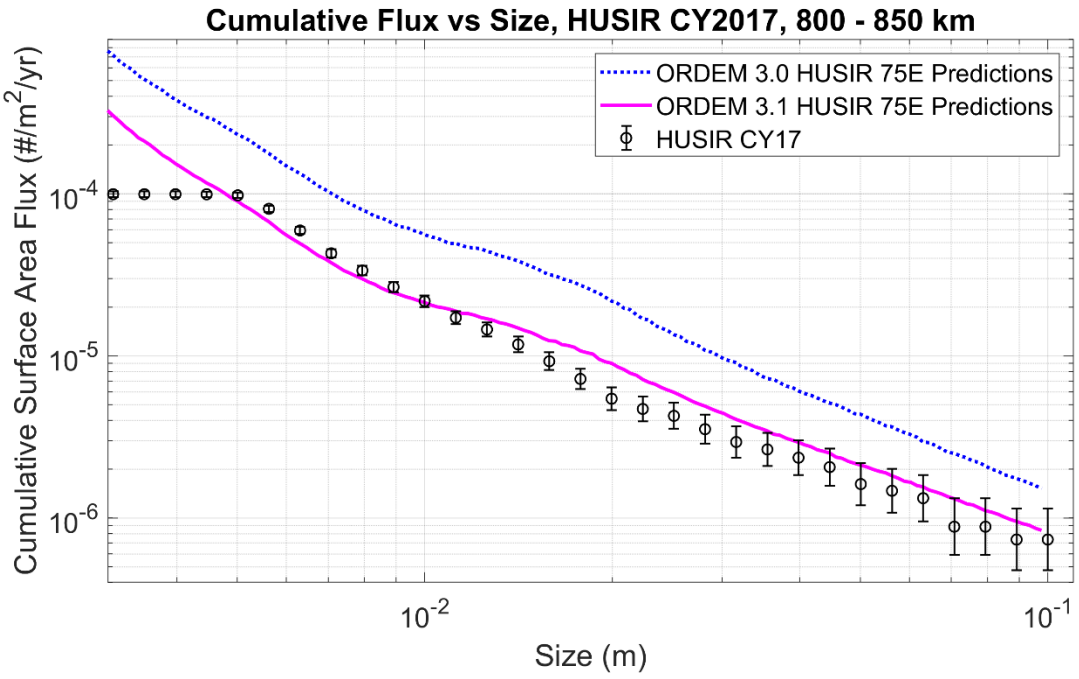

Figure B-17. Comparison of the surface area flux vs SEM size between ORDEM 3.0, ORDEM 3.1, and measurements from HUSIR 75E in 2017. The altitude is restricted to 800–850 km.

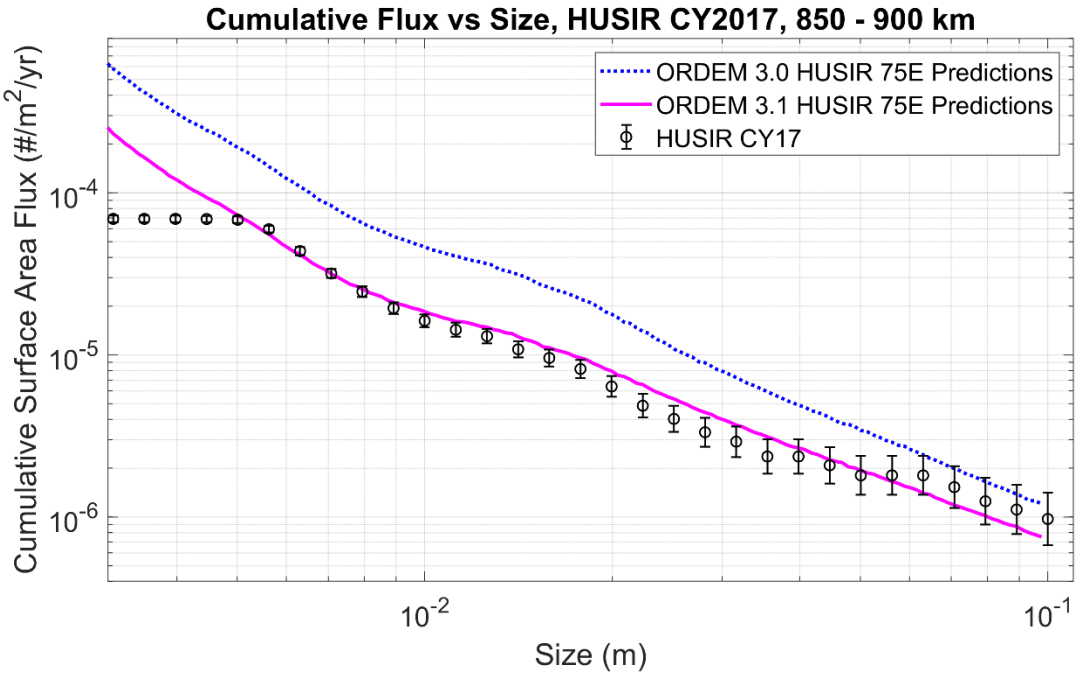

Figure B-18. Comparison of the surface area flux vs SEM size between ORDEM 3.0, ORDEM 3.1, and measurements from HUSIR 75E in 2017. The altitude is restricted to 850–900 km.

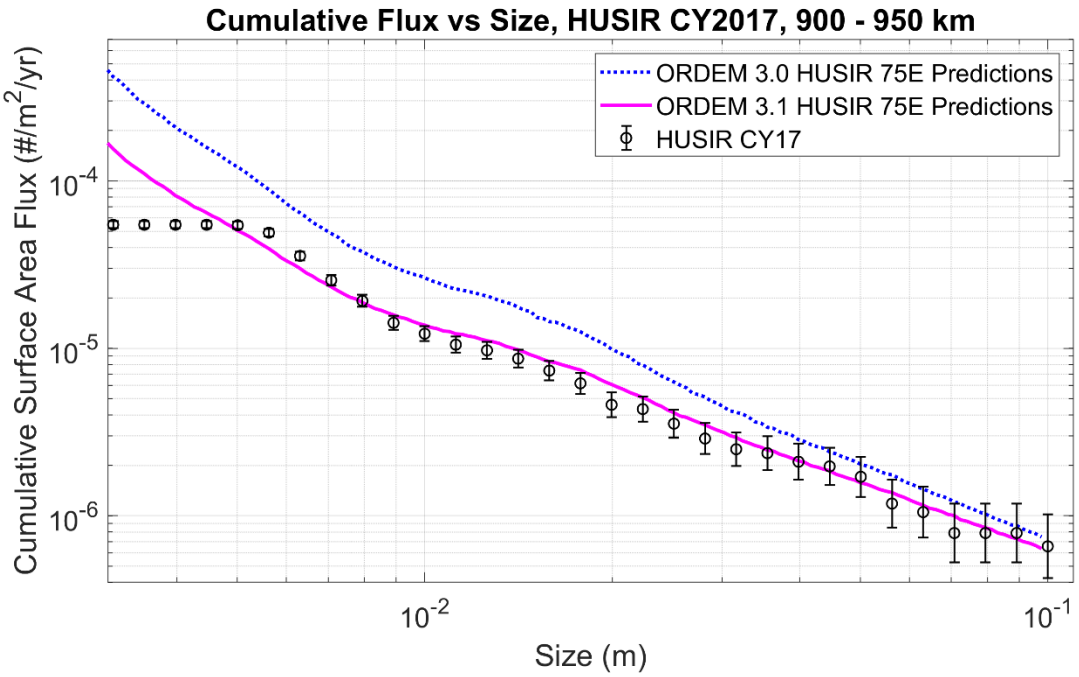

Figure B-19. Comparison of the surface area flux vs SEM size between ORDEM 3.0, ORDEM 3.1, and measurements from HUSIR 75E in 2017. The altitude is restricted to 900–950 km.

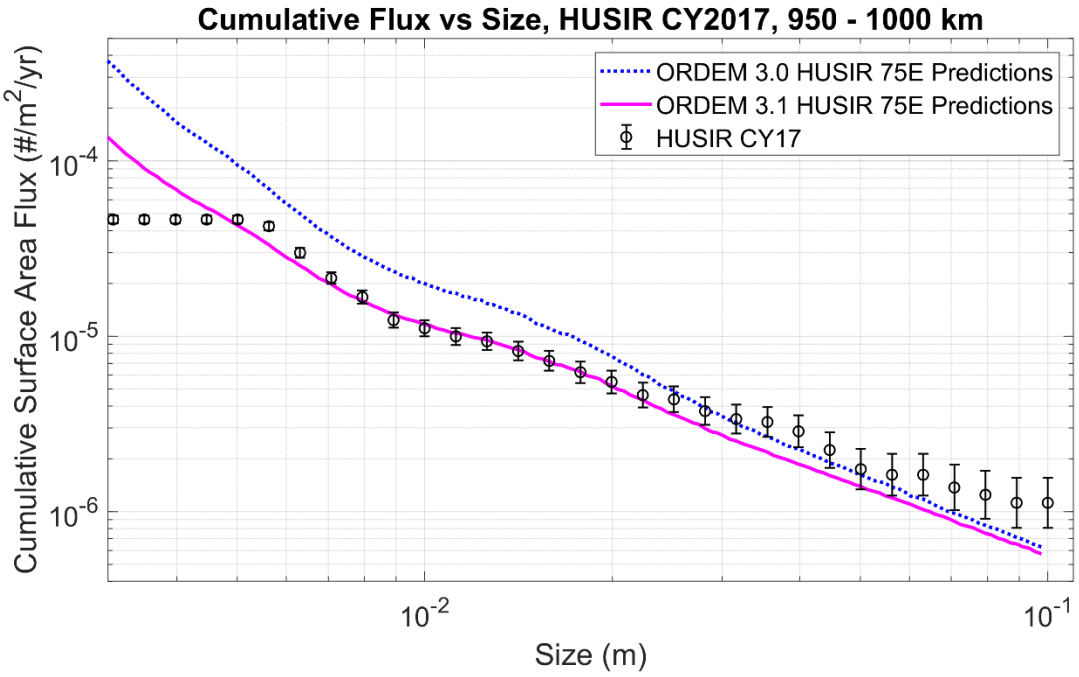

Figure B-20. Comparison of the surface area flux vs SEM size between ORDEM 3.0, ORDEM 3.1, and measurements from HUSIR 75E in 2017. The altitude is restricted to 950–1000 km.

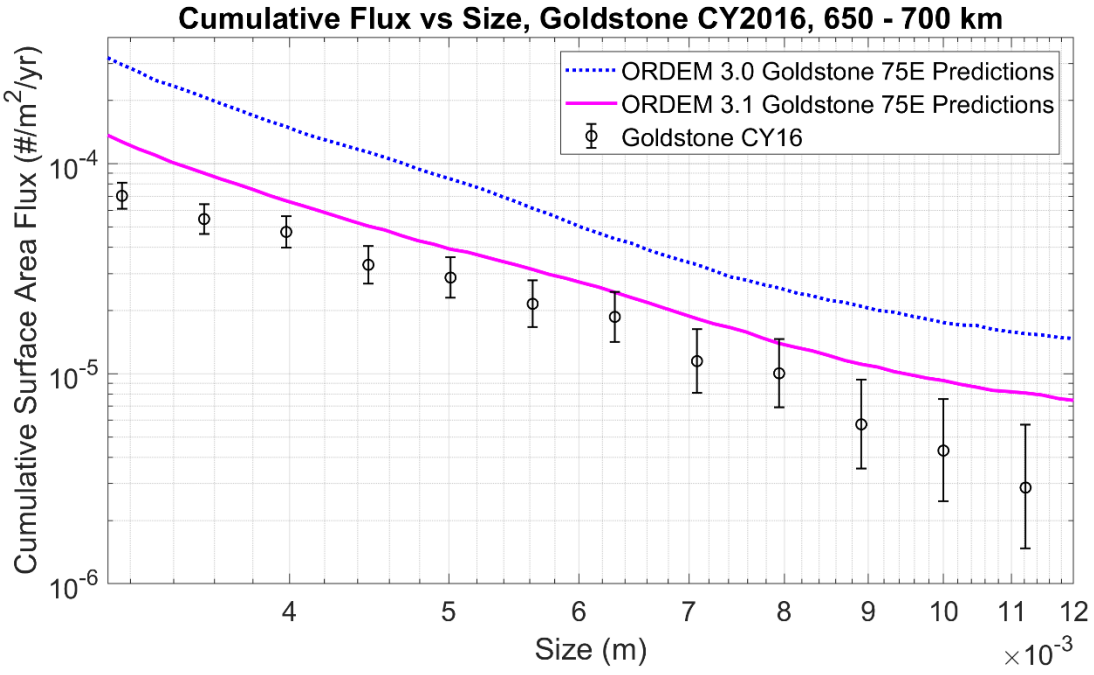

Figure B-21. Comparison of the surface area flux vs SEM size between ORDEM 3.0, ORDEM 3.1, and measurements from Goldstone 75E in 2016. The altitude is restricted to 650–700 km.

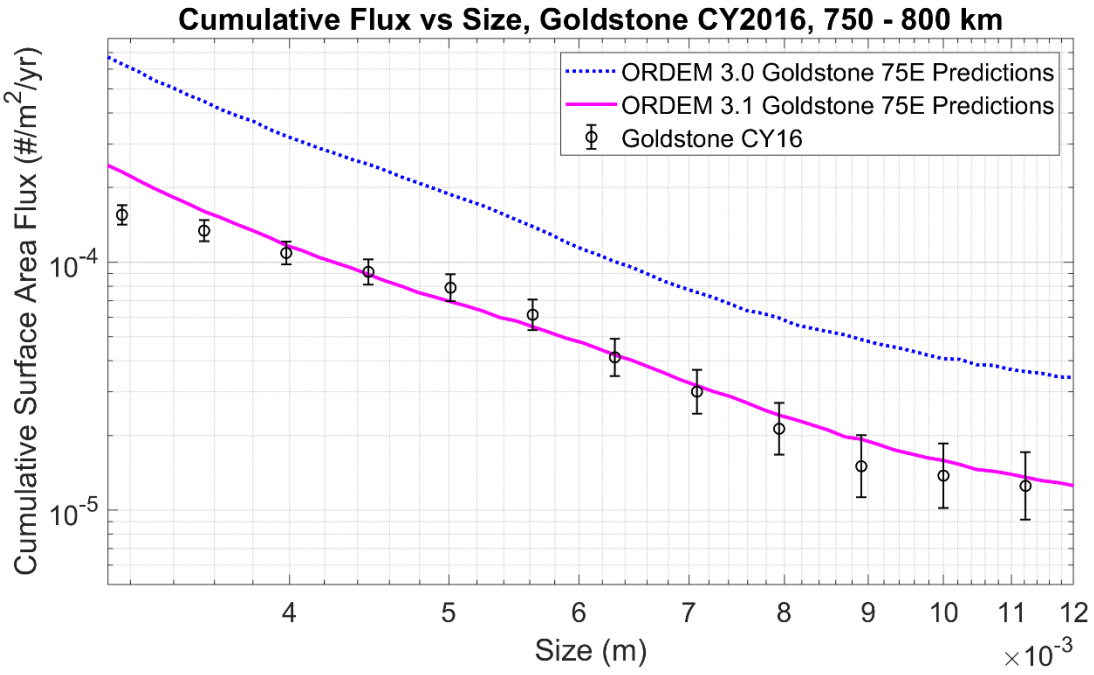

Figure B-22. Comparison of the surface area flux vs SEM size between ORDEM 3.0, ORDEM 3.1, and measurements from Goldstone 75E in 2016. The altitude is restricted to 750–800 km.

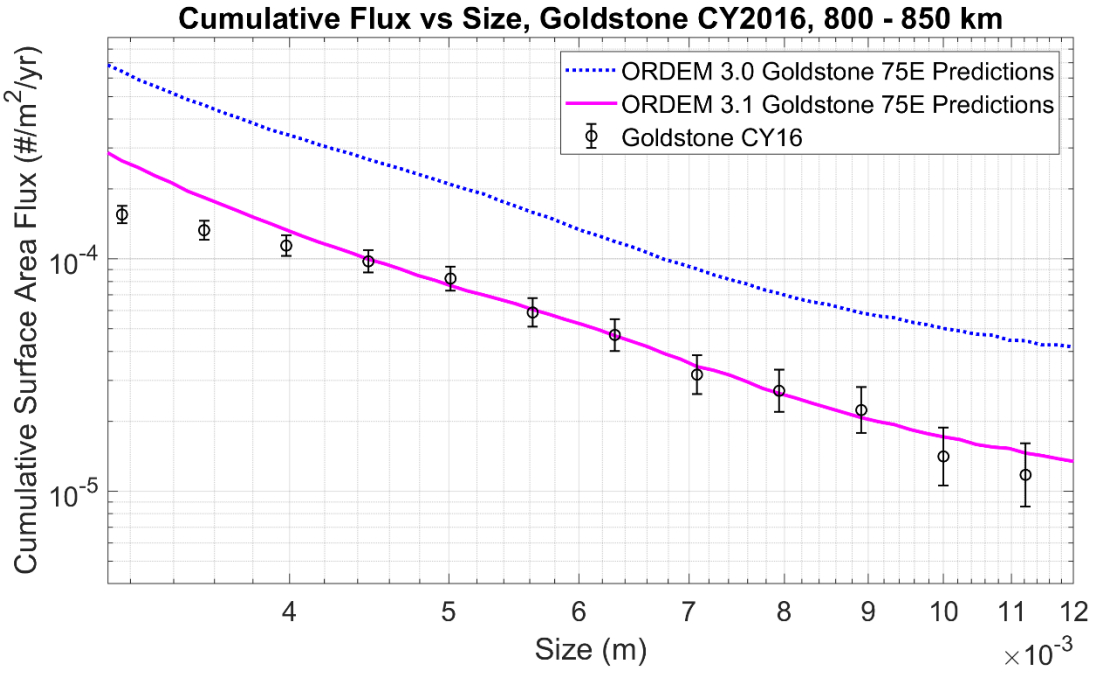

Figure B-23. Comparison of the surface area flux vs SEM size between ORDEM 3.0, ORDEM 3.1, and measurements from Goldstone 75E in 2016. The altitude is restricted to 800–850 km.

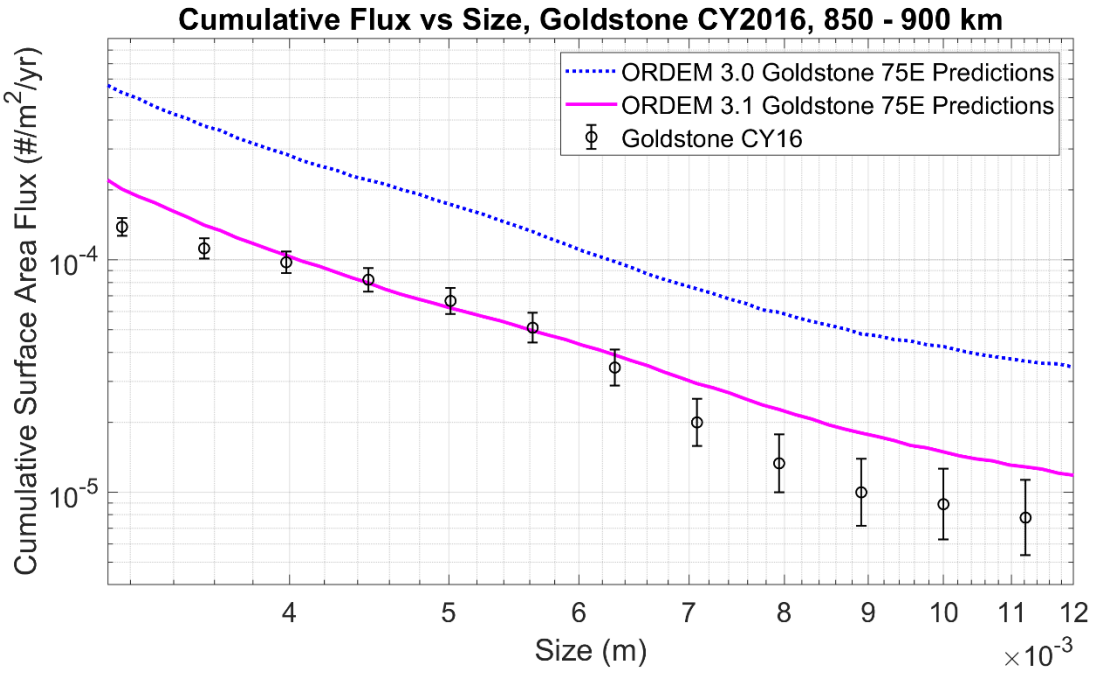

Figure B-24. Comparison of the surface area flux vs SEM size between ORDEM 3.0, ORDEM 3.1, and measurements from Goldstone 75E in 2016. The altitude is restricted to 850–900 km.

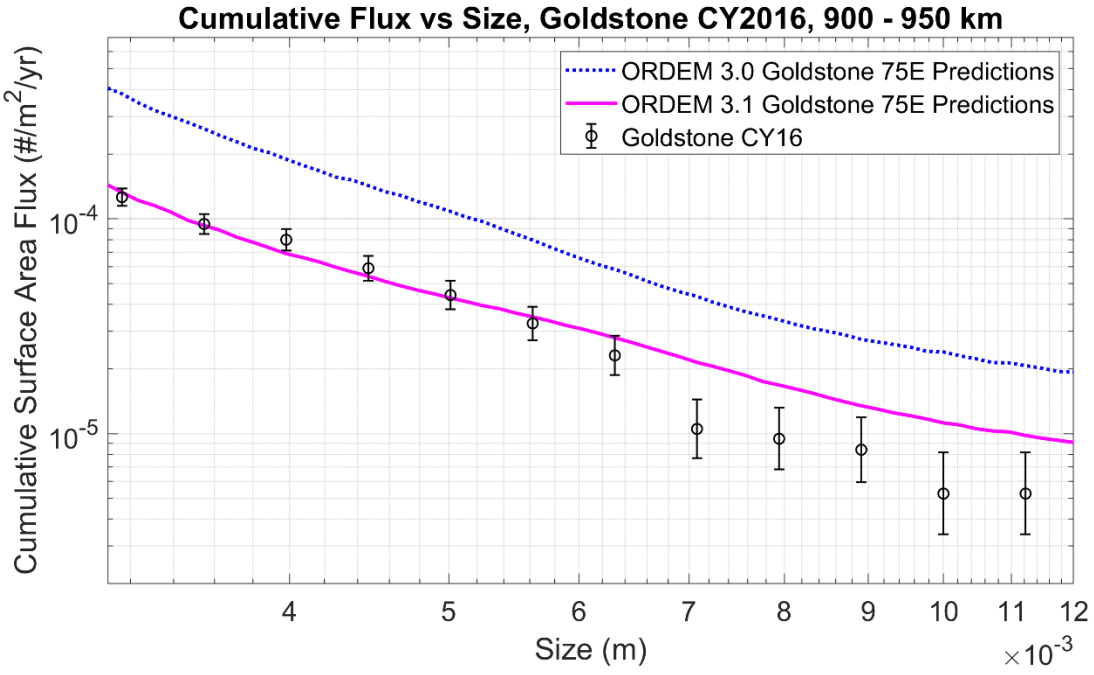

Figure B-25. Comparison of the surface area flux vs SEM size between ORDEM 3.0, ORDEM 3.1, and measurements from Goldstone 75E in 2016. The altitude is restricted to 900–950 km.

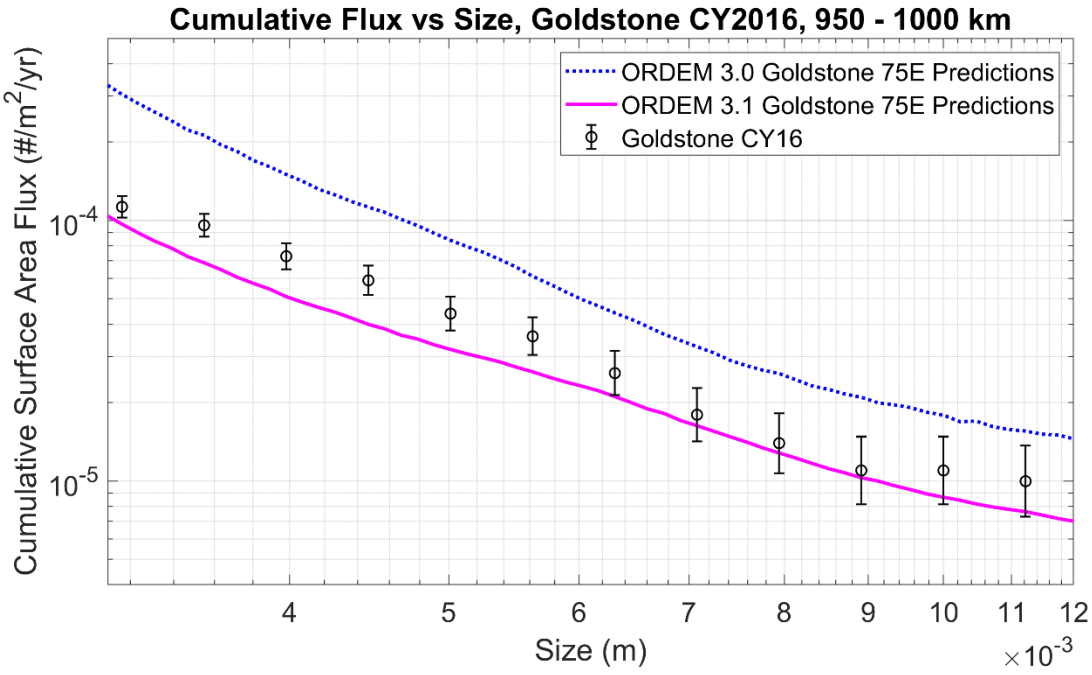

Figure B-26. Comparison of the surface area flux vs SEM size between ORDEM 3.0, ORDEM 3.1, and measurements from Goldstone 75E in 2016. The altitude is restricted to 950–1000 km.

C SOFTWARE VERIFICATION

C.1 DEFINITION

Verification is the demonstration of consistency, completeness, and correctness of the software products at each stage and between each stage of the development life cycle. The purpose of verification activities is to identify defects as early as possible and to ensure the correct translation of requirements to design to code. Performing verification activities throughout the lifecycle lead up to the successful validation of the final software products.

The commercially available issue tracking web application Jira™, developed by Atlassian, was used to store any software bugs, issues, and/or anomalies found during software verification by the ODPO testing group. Additionally, Jira also captures any new or modified requirements that surface during the entire project lifecycle.
Four different methods are used for verification: inspection, analysis, demonstration, and test, or a combination of these. The assigned method may prove invalid as the design matures. In this case, the requirement will be reevaluated to determine the appropriate verification method. The verification method will be documented by the tester on each test procedure.

- Analysis (A) is a verification method utilizing existing data such as prior test data, vendor test results, data bus traffic logs, *etc.*, to reach a conclusion concerning the functionality and/or performance of the software. The existing data is “analyzed” to confirm that requirements are met. Comparisons and calculations may be necessary to reach the conclusion. Obviously, the existing data must contain enough pertinent data to conclude that requirements are satisfied. An example of analysis would be to review a data bus traffic log from a previous test and use data from the log in calculations to determine timing performance of certain messages.
- Inspection (I) is a verification method which involves physical examination of the software under test to reach a conclusion regarding requirements satisfaction. As opposed to verification by analysis, verification by inspection will not require any extra calculations. The conclusion should be obvious and immediately visible. An example of an inspection would be a review of source code to ensure that coding standards are being followed.
- Demonstration (D) is a verification method which involves “executing” the software to “demonstrate” that it functions/performs per requirements. As opposed to verification by inspection, verification by demonstration requires that the software is operating. The conclusion can be made visually during the execution without any further analysis. One example of verification by demonstration is a functional test to show that a user interface display meets format requirements.
- Test (T) is a verification method, which involves measurement/analysis of responses after the controlled application of stimuli. This activity may involve special equipment to create the stimuli and record/measure/analyze the responses. An example of a test would be an end-to-end checkout of the effect of issuing a command to the software.

C.2 ORDEM PROCESSOR

This section outlines the results of verifying compliance of the ORDEM 3.1 software requirements and coding standards related to the low-level processor source code. Software improvements related to the publicly released ORDEM 3.0 software are also listed here.

Table C-1 shows the test details that include the description, the verification method, the expected outcome, and result (*i.e.*, pass or fail). The development team considers these results acceptable and thus verified.

Table C-1 Software Verification Results from the ORDEM Processor

Description	Method	Expected Outcome	Result
Correct flux calculation for highly elliptical, high inclination, orbits	I,D	Increased number of Monte Carlo integration calls for highly inclined orbits	Pass
Allocate and deallocate large arrays to avoid memory leaks	I,D	Proper allocation and deallocation of arrays	Pass
Include correction of sigma values for GEO in spacecraft mode	I,D	Standard deviation calculated correctly	Pass
Update fit method at each fiducial point	I,D	Follows the same interpolation technique as HVIT, BUMPER	Pass
Correct units in IGLOO S/C output file	I,D	Flux units are no./m^2/yr	Pass
Correct m^2 as units in DIRFLUX S/C output file	I,D	Flux units are no./m^2/yr/kps	Pass
The ORDEM 3.1 igloo output files shall adhere to a strict format, where the igloo data starts on the same row, regardless of warning messages	I,D	All *.out files contain the header; data starts on correct row	Pass
ORDEM 3.1 shall include the version number on first line of all *.out files	I,D	All *.out file start with “ORDEM 3.1”	Pass

C.3 ORDEM GUI

This section outlines the results of verifying compliance of the ORDEM 3.1 software requirements and coding standards related to the ORDEM graphical user interface. Software improvements related to the publicly released ORDEM 3.0 software are also listed here.

Table C-2 shows the test details that include the description, the verification method, the expected outcome, and result (*i.e.*, pass or fail). The development team considers these results acceptable and thus verified.

Table C-2 Software Verification Results from ORDEM GUI

Description	Method	Expected Outcome	Result
Remove “export to PDF” function in Teechart dialog	D	Export to PDF option does NOT appear	Pass
Allow eccentricity of zero in GUI	D	‘0.0’ appears in the eccentricity textbox with no errors	Pass
Allow zero-degree inclination	D	‘0.0’ appears in the inclination textbox with no errors	Pass
Exclude “Native” and “Theme” tab from the export editor found on the top menu bar of the graph window	D	The “Native” and “Theme” tabs do NOT appear	Pass
Display error message when object is not in LEO or GEO	D	Error message displays as expected	Pass
Prompt user for confirmation to overwrite output files from a previous run in the project directory	D	Confirmation dialog window displays as expected	Pass

Description	Method	Expected Outcome	Result
Range of acceptable S/C inclinations	D	Inclination values fall within allowed range	Pass
ORDEM 3.1 shall output progress status during ORDEM run	I,D	Progress bar is displayed next to the percent complete	Pass
ORDEM 3.1 GUI shall allow backwards compatibility with ORDEM 3.0 projects	D	User-specified plots are generated as expected	Pass
Flux calculator dialog displays NaN	D	Values of flux remain within expected parameters	Pass
“Select project folder” dialog	I,D	Updated dialog window	Pass
Update the GUI icons	I,D	Higher quality images visible	Pass

C.4 REFERENCE SUBPOPULATIONS

This section outlines the results of verifying compliance of the ORDEM 3.1 software requirements and coding standards related to the ORDEM reference subpopulations (*i.e.*, SNAPSHOT, Transit, NaK, Fengyun-1C antisatellite [ASAT] test, Iridium 33/Cosmos 2251 accidental collision, degradation, > 1mm background). Additionally, since the > 1 mm background subpopulation consists of objects generated from LEGEND Monte Carlo runs, all LEGEND-related issues are addressed here as well.

Table C-3 shows the test details that include the description, the verification method, the expected outcome, and result (*i.e.*, pass or fail). The development team considers these results acceptable and thus verified.

Table C-3 Software Verification Results related to ORDEM Reference Subpopulations

Description	Method	Expected Outcome	Result
LEGEND simulation runs shall include a post mission disposal rate of 90% for spacecraft and rocket bodies	I,D	Correct PMD value used	Pass
LEGEND simulation runs shall use the three-density source code version	I,D	Proper LEGEND source code used	Pass
LEGEND simulation runs shall include intact and fragmentation objects with sizes greater than 1 mm	I,D	Correct size used	Pass
LEGEND simulation runs shall use the April 2016 solar flux file	I,D	solarflux_table.dat file contains 2016/04/18	Pass
LEGEND simulation runs shall use the custom scale factors for historical fragmentation events	I,D	set to true	Pass
LEGEND simulation runs shall use the 2015 DBS delivery of space traffic files, where historical data is defined as 1957 through 2015 traffic	I,D	Start/stop years fall within expected range	Pass
The Fengyun-1C (FY-1C, ASAT) special population shall be recertified for ORDEM 3.1 software, for sizes > 1 mm	T	Population resides in expected zones	Pass
The SNAPSHOT special population shall be recertified for ORDEM 3.1 software, for sizes 1 mm to 10 cm	T	Population resides in expected zones	Pass

Description	Method	Expected Outcome	Result
The Transit special population shall be recertified for ORDEM 3.1 software, for sizes 1 mm to 10 cm	T	Population resides in expected zones	Pass
The Iridium 33 special population shall be recertified for ORDEM 3.1 software, for sizes > 1 mm	T	Population resides in expected zones	Pass
The Cosmos 2251 special population shall be recertified for ORDEM 3.1 software, for sizes > 1 mm	T	Population resides in expected zones	Pass
ORDEM 3.1 population files shall include a degradation/ejecta sub-population for the size range 10 μm to 3.16 mm	T	Population resides in expected zones	Pass
The NaK population shall be recertified for ORDEM 3.1 software, for sizes 1 mm to 10 cm	T	Population resides in expected zones	Pass

C.5 ORDEM ASSESSMENT MODE

The ORDEM 3.1 processor was put through a series of specific regression test cases to verify that changes made to the processor code during ORDEM 3.1 development (*e.g.,* for improved computational efficiency) did not affect the rest of the software functionality that did not undergo any changes. To accomplish this regression testing, the test group used a variant ORDEM 3.1 processor software that reads in ORDEM 3.0 yearly population files. Each test case was run through the publicly released ORDEM 3.0 software and the variant ORDEM 3.1 software, and the output flux values (stored in *.OUT files for a given ORDEM run) were compared. The test objectives checklist is shown in Table C-4.

Table C-4: Test objectives for spacecraft and telescope modes

Objective	Passed
Use test satellites/observation modes, each with various years	✓
Compare MD60 flux values	✓
Compute statistics (*i.e.,* correlation coefficient, sample covariance, standard error of the estimate.)	✓
Generate figures for comparison	✓

For N samples, the sample covariance, S_{xy}, between ORDEM 3.0 x samples and ORDEM 3.1 variant y samples is:

$$S_{xy} = \frac{\sum_{i=1}^{N}(x_i - \bar{x})(y_i - \bar{y})}{n-1}.$$

The correlation coefficient, ρ_{xy}, is between x and y:

$$\rho_{xy} = \frac{S_{xy}}{\sigma_x \sigma_y}.$$

Finally, the standard error of the estimate, s_{est}, is computed as follows:

$$s_{est} = \sqrt{\frac{\sum_{i=1}^{N}(y_i - y_{est})^2}{n-2}}.$$

Table C-5 describes the spacecraft used for the spacecraft mode tests, including the orbit type, Apogee height (km), Perigee height (km), inclination (degrees), and right ascension of the ascending node (degrees). These satellites are spread out through three different regions – Molniya (highly eccentric, high inclination), GTO, and GEO.

Table C-5: Spacecraft Used for ORDEM Spacecraft Mode Verification

Int. Designator	SSN #	Name	Orbit type	TLE epoch	Apogee (km)	Perigee (km)	Inc (°)	RAAN (°)
1986-003C	16483	SATCOM K1 R/B	GTO	10001.41392	33774.28	353.01	27.23	38.56
2004-005A	28163	MOLNIYA 1-93	Molniya	11001.15607	38591.13	1764.28	64.83	221.66
2009-075A	36131	DIRECTV 12	GEO	14001.42237	35786.89	35785.77	0.031	216.32

Table C-6 shows the spacecraft mode test details for each spacecraft/orbit type including ORDEM population year, and argument of perigee (degrees). Since both ORDEM 3.0 and the variant ORDEM 3.1 software use the same yearly population files as inputs, the results should be the same for both runs. Therefore, the criteria for a successful test is more strict. A test is marked as “Passed” if the correlation coefficient is greater than or equal to 0.99999 and the standard error of the estimate is less than 1e-3. All test cases considered here passed using these criteria. Figure C-1 through Figure C-6 pair the flux distribution between ORDEM 3.0 and ORDEM 3.1 variant runs, showing agreement between the results in all cases.

Table C-6: Software Verification Results (Medium Density, 1 m) from ORDEM Spacecraft Mode

Satellite Name	Orbit Type	Year	Argument of Perigee (°)	Correlation Coefficient	Sample Covariance	Standard Error of the Estimate	Passed
SATCOM K1 R/B	GTO	2016	100.22	0.99999	14.46374	7.51332e-05	✓
SATCOM K1 R/B	GTO	2023	100.22	0.99999	15.64581	7.41210e-05	✓
MOLNIYA 1-93	Molniya	2022	267.11	0.99999	11.69976	7.68334e-05	✓
MOLNIYA 1-93	Molniya	2029	267.11	0.99999	14.51694	8.50329e-05	✓
DIRECTV 12	GEO	2020	85.44	0.99999	8.94537	1.98478e-04	✓
DIRECTV 12	GEO	2027	85.44	0.99999	18.18778	2.11117e-04	✓

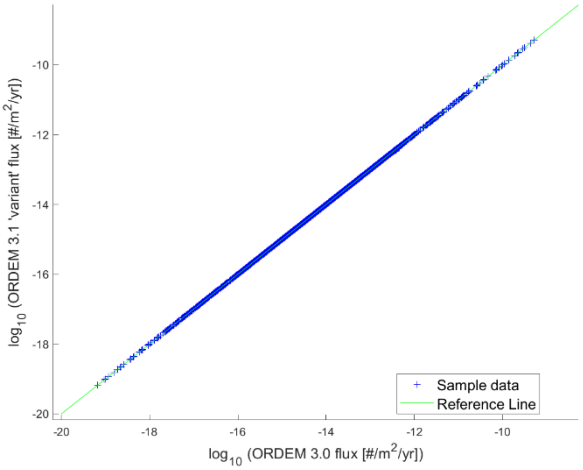

Figure C-1. SATCOM (GTO), flux, 2016, Fixed AP.

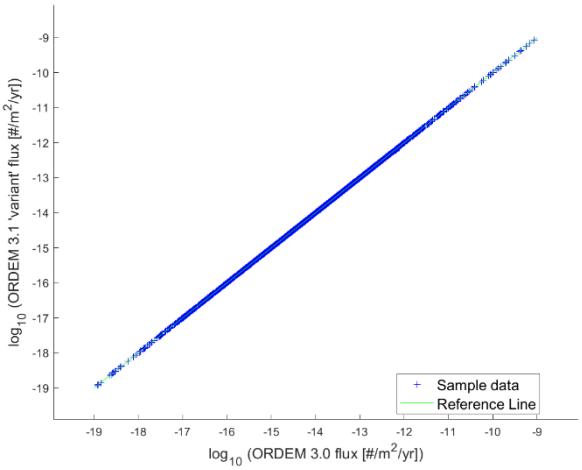

Figure C-2. SATCOM (GTO), flux, 2023, Fixed AP.

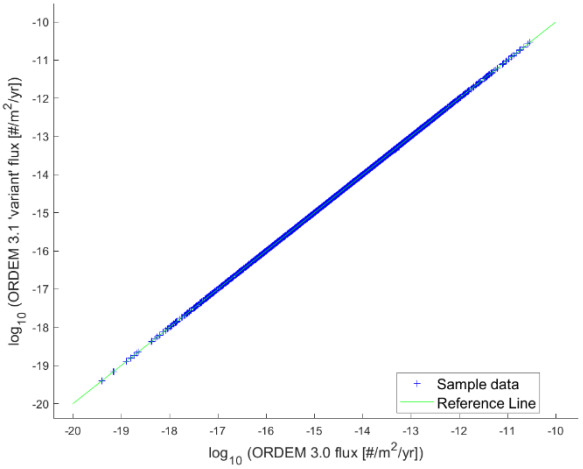

Figure C-3. Molniya, flux, 2022, Fixed AP.

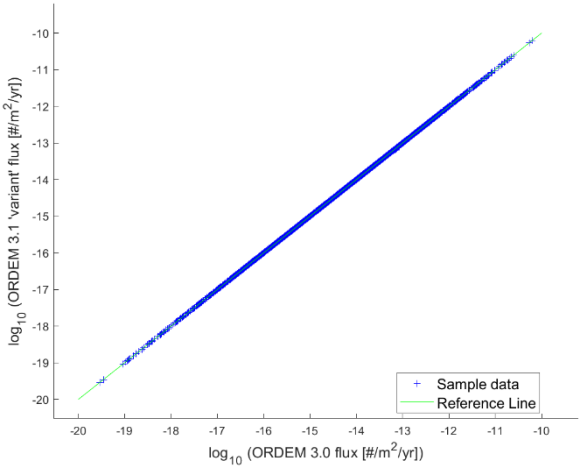

Figure C-4. Molniya, flux, 2029, Fixed AP.

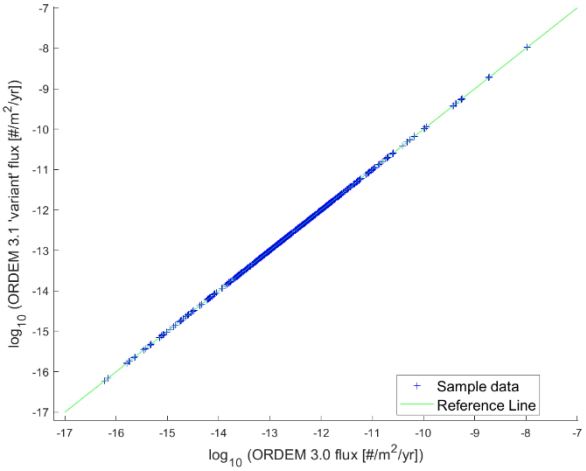

Figure C-5. DIRECTV (GEO), flux, 2020, Fixed AP.

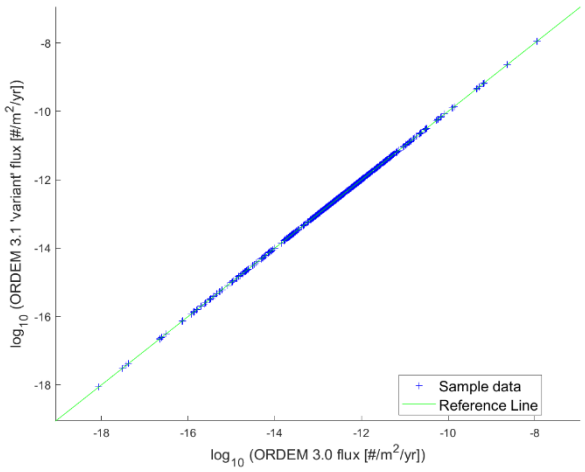

Figure C-6. DIRECTV (GEO), flux, 2027, Fixed AP.

Table C-7 describes the observation sites used for the telescope/radar mode tests, including the sensor name, ORDEM population year, latitude (degrees), azimuth (degrees), and elevation (degrees).

Table C-7: Observation sites used in ORDEM Telescope Mode

Sensor Name	Year	Latitude (°)	Azimuth (°)	Elevation (°)
Haystack (75E)	2018	42.6	90	75
Haystack (75E)	2022	42.6	90	75
Haystack (20S)	2018	42.6	180	20
Ascension	2020	-7	0	80

Table C-8 shows the telescope/radar mode test details for each observation type in a given year. Since both ORDEM 3.0 and the ORDEM 3.1 variant software use the same yearly population files as inputs, the results should be the same for both runs. Therefore, the criteria for a successful test is more strict. A test is marked as “Passed” if the correlation coefficient is greater than or equal to 0.99999 and the standard error of the estimate is less than 1e-3. All test cases considered here passed using these criteria. Figure C-7 through Figure C-10 pair the flux distribution between ORDEM 3.0 and variant ORDEM 3.1 runs, showing agreement between the results in all cases.

Table C-8: Software Verification Results from ORDEM Telescope Mode

Sensor Name	Year	Correlation Coefficient	Sample Covariance	Standard Error of the Estimate	Passed
Haystack (75E)	2018	1.00000	5.40202	2.65673e-09	✓
Haystack (75E)	2022	1.00000	5.47732	2.70654e-09	✓
Haystack (20S)	2018	0.99999	4.41546	1.14676e-08	✓
Ascension	2020	0.99999	1.64315	2.96805e-08	✓

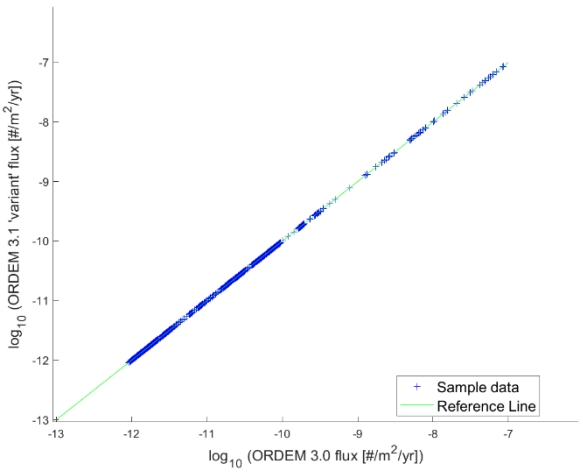

Figure C-7 Haystack (75E), flux, 2018.

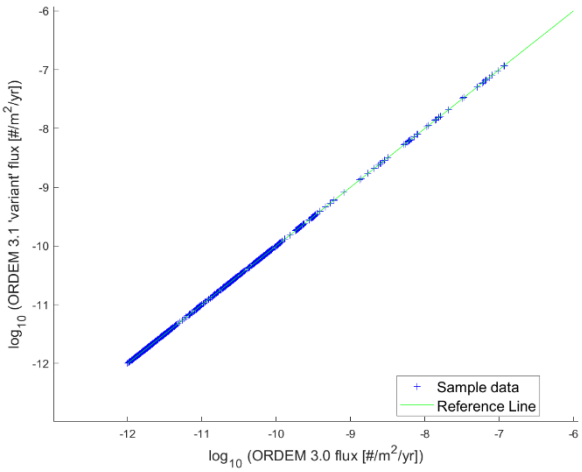

Figure C-8. Haystack (75E), flux, 2022.

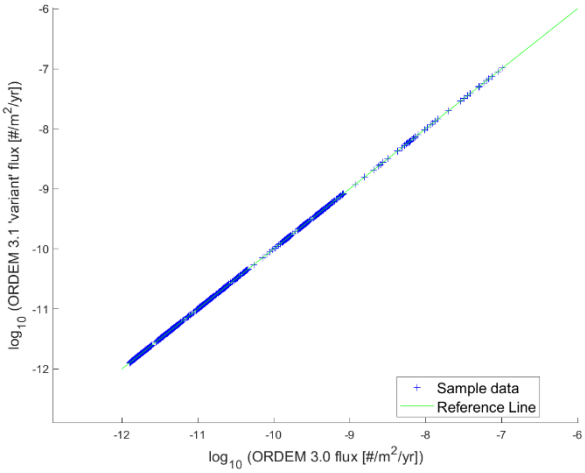

Figure C-9. Haystack (20S), flux, 2018.

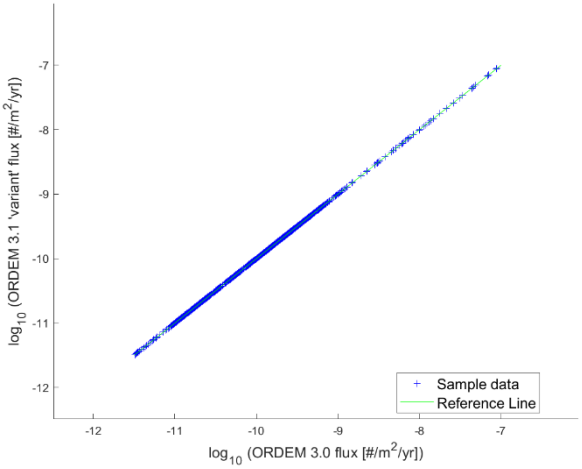

Figure C-10. Ascension, flux, 2020.

The development team considers these results acceptable and thus verified. Output files for spacecraft and/or telescope/radar mode test cases are available upon request.